

**Universidade do Minho**  
Escola de Ciências

Jorge Miguel Fernandes da Cunha

**Computational Development of New  
Biocatalyst for Plastic Degradation through  
QM/MM Methods**

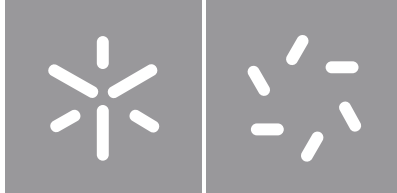
**Computational Development of New  
Biocatalyst for Plastic Degradation  
through QM/MM methods**

Jorge Cunha

UMinho | 2021

December 2021





**Universidade do Minho**

Escola de Ciências

Jorge Miguel Fernandes da Cunha

**Computational Development of New  
Biocatalyst for Plastic Degradation through  
QM/MM Methods**

Master Thesis

Master in Biophysics and Bionanosystems

Work developed under the supervision of

**Dr. Sérgio Filipe Maia de Sousa**

**Prof. Dr. Elisabete Maria dos Santos Castanheira  
Coutinho**

## DIREITOS DE AUTOR E CONDIÇÕES DE UTILIZAÇÃO DO TRABALHO POR TERCEIROS

Este é um trabalho académico que pode ser utilizado por terceiros desde que respeitadas as regras e boas práticas internacionalmente aceites, no que concerne aos direitos de autor e direitos conexos.

Assim, o presente trabalho pode ser utilizado nos termos previstos na licença abaixo indicada.

Caso o utilizador necessite de permissão para poder fazer um uso do trabalho em condições não previstas no licenciamento indicado, deverá contactar o autor, através do RepositóriUM da Universidade do Minho.



Atribuição-NãoComercial-SemDerivações

CC BY-NC-ND

<https://creativecommons.org/licenses/by-nc-nd/4.0/>

# Agradecimentos

Esta tese representa uma importante etapa da minha vida, a nível pessoal e profissional. A todos os que contribuíram para a realização deste trabalho deixo aqui o meu agradecimento.

Ao meu orientador Doutor Sérgio F. Sousa, agradeço pela oportunidade de ingressar no seu grupo de pesquisa e pela oportunidade de trabalhar consigo. Foi um ano de muita aprendizagem, numa área que pouco conhecia, mas com o seu empenho, dedicação e ensinamento acabei por desenvolver bastante o gosto pela biocomputação.

À Professora Doutora Elisabete Coutinho, agradeço a sua disponibilidade e ensinamentos manifestados ao longo da dissertação.

A todos os membros do grupo de pesquisa BioSIM, em especial ao Henrique S. Fernandes e à Rita P. Magalhães, agradeço pelos ensinamentos e pela motivação demonstrada ao longo do ano.

Aos amigos de longa data, André Verdelho, Daniel Oliveira, Joana Costa, Daniel Pereira, Diogo Silva e Fátima Peixoto agradeço pelos momentos de descontração e pela motivação. Às três últimas pessoas mencionadas, desejo-vos votos de sucesso nos vossos projetos de tese.

Aos amigos de licenciatura, Edgar Moita, Patrícia Rodrigues, Rita Oliveira, Leandro Soares, Fábio Pombo e Fábio Lopes, o meu sincero agradecimento pela amizade mantida pelos anos e pelos momentos de descontração.

Aos amigos de mestrado, Ana Martins, Diana Sousa e Fábio Lopes, agradeço a vossa companhia nesta desafiante etapa e pelos momentos de apoio e descontração. Haveremos todos de cantar Harry Styles novamente, como mestres.

Por fim, à minha família pelo apoio incansável e por acreditarem sempre em mim. Aos meus irmãos e ao meu país, agradeço o sacrifício feito, sem vocês não conseguiria realizar este trabalho. Às minhas “estrelas”: avó Luísa, tia Estefânia e avô “Martelo”, dedico-vos esta tese, obrigado.

## STATEMENT OF INTEGRITY

I hereby declare having conducted this academic work with integrity. I confirm that I have not used plagiarism or any form of undue use of information or falsification of results along the process leading to its elaboration.

I further declare that I have fully acknowledged the Code of Ethical Conduct of the University of Minho.

## Computational Development of New Biocatalyst for Plastic Degradation through QM/MM Methods

### Resumo

Os polímeros sintéticos têm sido produzidos de forma excessiva nestes últimos anos chegando a atingir cerca de 350 milhões de toneladas por ano. A demanda destes plásticos deve-se às suas propriedades, tais como, não degradabilidade, baixo custo, alta resistência, habilidade de serem moldados a pressões e temperaturas altas, entre outros. Contudo, este excesso leva à sua deposição em aterros, que posteriormente são depositados em ambientes aquáticos e terrestres, causando dessa forma consequências adversas para os biosistemas.

O método industrial para a degradação de plástico requer pressões e temperaturas altas, e normalmente a adição de solventes orgânicos que levam à formação de poluentes ambientais adicionais. Dessa forma, é necessário uma solução mais viável.

A biodegradação de plástico por enzimas biocatalisadoras tem sido estudada e desenvolvida nos últimos anos, sendo a biodegradação de plástico polietileno tereftalato (PET) o mais recorrente. A degradação deste plástico, normalmente resulta nos produtos intermédios tereftalato de bis(2-hidroxietileno) (BHET) e ácido tereftálico mono-(2-hidroxietil) (MHET) e nos produtos finais ácido tereftálico (TPA) e etileno glicol (EG).

Neste projeto, foi estudado o mecanismo catalítico da enzima *h*SMHETase contra o substrato MHET, através de métodos computacionais, nomeadamente, métodos híbridos de mecânica quântica/mecânica molecular (QM/MM) usando um esquema subtrativo (ONIOM). A parte QM é composta pelos resíduos de aminoácidos essenciais na reação e foi calculada usando a teoria do funcional de densidade, onde o funcional utilizado foi o B3LYP e a base de funções 6-31G(d,p). Entretanto, a parte MM que envolve o resto do sistema foi calculada através de mecânica molecular, nomeadamente por campos de força ff14SB e GAFF.

Os resultados revelaram um mecanismo catalítico de cinco passos, que são divididos em acilação e desacilação. Durante o processo de acilação, Ser225 é desprotonada pela His528 e torna-se um nucleófilo que ataca o grupo carbonilo do substrato MHET, originando o intermediário ácil-enzima e libertando o produto EG. Durante a desacilação, uma molécula de água é desprotonada pela His528 que ataca o intermediário, libertando o segundo produto TPA.

### Palavras-Chave

Biocatalisadores, degradação de plástico, *h*SMHETase, mecanismo catalítico, métodos QM/MM

## Computational Development of New Biocatalyst for Plastic Degradation through QM/MM Methods

### Abstract

Synthetic polymers are being produced in an excessive way, reaching about 350 million tons yearly. The demand of these plastics is due to their properties, such as non-degradability, low cost, high resistance, ability to be moulded at high pressures and temperatures, many others. However, the excess leads to its deposition in landfills that end up deposited in aquatic and terrestrial environments, causing several hazard consequences to the biosystems.

Industrial strategy for plastic degradation requires high pressure and temperature, and often organic solvents, causing additional environmental pollutants. Therefore, it is necessary a more environmentally friendly strategy.

Plastic biodegradation by biocatalyst enzymes have been studied and developed in recent years, being the polyethylene terephthalate (PET) the most studied plastic. The degradation of this plastic normally results in bis(2-hydroxyethyl)terephthalic acid (BHET) and mono-(2-hydroxyethyl)terephthalic acid (MHET) intermediates and terephthalic acid (TPA) and ethylene glycol (EG) building blocks.

In this project, the catalytic mechanism of *h*SMHETase enzyme against MHET substrate was studied, using computational means, namely hybrid quantum mechanical/molecular mechanical (QM/MM) methodology with subtractive scheme (ONIOM). The QM part is composed of key amino acid residues involved in the reaction and was calculated using density functional theory with the functional B3LYP and the basis set 6-31G(d,p). Meanwhile, the MM part encompasses the remaining of the system and was calculated using molecular mechanics, namely ff14SB and GAFF force fields.

The results showed a five-step catalytic mechanism that are divided in acylation and deacylation. In acylation, Ser225 is deprotonated by His528, becoming a nucleophile and attacks the carbonyl group of MHET substrate, resulting in the formation of the acyl-intermediate enzyme and the release of EG. In deacylation, a water molecular is deprotonated by His528 and attacks the intermediate, resulting in the second product TPA.

### Keywords

Biocatalysts, catalytic mechanism, plastic degradation, *h*SMHETase, QM/MM methodology



# Table of Content

Agradecimientos .....	iiv
Resumo .....	vi
Abstract .....	vii
Table of Content .....	viii
Index of Figures .....	xiv
Index of Equations .....	xvi
Index of Tables.....	xvii
List of Abbreviations .....	xviii
A. Introduction .....	1
1. Plastic .....	2
1.1. Types of plastic .....	3
1.1.1. Polyethylene Terephthalate (PET) .....	3
1.1.2. Polyurethane (PUR) .....	4
1.1.3. Polyethylene (PE).....	4
1.1.4. Polypropylene (PP) .....	5
1.1.5. Polyamide (PA) .....	5
1.1.6. Polystyrene (PS) .....	6
1.1.7. Polyvinyl Chloride (PVC).....	6
1.2. Classification of plastic .....	6
1.3. Additives .....	7
1.4. Negative impacts .....	7
1.4.1. Human health .....	8
1.4.2. Ecosystems .....	10

1.4.3. Atmosphere.....	11
2. Biodegradation solution.....	11
2.1. <i>Ideonella sakaiensis</i> PETase ( <i>Is</i> PETase).....	12
2.1.1. Discovery.....	12
2.1.2. Structure.....	12
2.1.3. Activity.....	14
2.1.4. Proposed mechanism.....	16
2.2. <i>Ideonella sakaiensis</i> ( <i>Is</i> MHETase).....	17
2.2.1. Discovery.....	17
2.2.2. Structure.....	17
2.2.3. Activity.....	18
2.2.4. Proposed Mechanism.....	19
2.3. <i>Pseudomonas aestusnigri</i> PETase ( <i>Pa</i> PETase).....	20
2.3.1. Discovery.....	20
2.3.2. Structure.....	20
2.3.3. Activity.....	21
2.3.4. Proposed Mechanism.....	22
2.4. LC-Cutinase (LCC).....	22
2.4.1. Discovery.....	22
2.4.2. Structure.....	22
2.4.3. Activity.....	23
2.5. <i>Thermomonospora fusca</i> Hydrolase ( <i>TH</i> Cut) and <i>Thermomonospora fusca</i> BTA Hydrolase 2 (BTA-2).....	25
2.5.1. Discovery.....	25
2.5.2. Structure.....	25
2.5.3. Activity.....	26
2.5.4. Proposed mechanism.....	27
2.6. <i>Saccharomonospora viridis</i> AHK190 Cutinase ( <i>Si</i> Cut190).....	27
2.6.1. Discovery.....	27
2.6.2. Structure.....	27
2.6.3. Activity.....	28
2.6.4. Proposed Mechanism.....	29
2.7. <i>Thermobifida</i> Genus Cutinase 1 and Cutinase 2 (Cut1 and Cut2).....	30

2.7.1. Discovery.....	30
2.7.2. Structure .....	30
2.7.3. Activity.....	31
2.8. <i>Fusarium oxysporum</i> Cutinase 5 ( <i>FoCut5a</i> ) .....	32
2.8.1 Discovery.....	32
2.8.2. Structure .....	33
2.8.3. Activity.....	34
2.9. <i>Humicola insolens</i> Cutinase ( <i>HCut</i> ).....	34
2.9.1. Discovery.....	34
2.9.2. Structure .....	34
2.9.3. Activity.....	35
2.10. <i>Fusarium solani</i> Cutinase ( <i>FsCut</i> ) .....	35
2.10.1. Discovery .....	35
2.10.2. Structure .....	35
2.10.3. Activity .....	36
2.11. <i>Candida antarctica</i> Lipase B ( <i>CaLipB</i> ).....	36
2.11.1. Discovery .....	36
2.11.2. Structure .....	37
2.11.3. Activity .....	38
2.12. <i>Thermomyces lanuginosus</i> Lipase ( <i>TLip</i> ).....	38
2.12.1. Discovery .....	38
2.12.2. Structure .....	38
2.12.3. Activity .....	39
2.13. <i>Thermobifida fusca</i> Carboxylesterase ( <i>TCa</i> ).....	39
2.13.1. Discovery .....	39
2.13.2. Structure .....	40
2.13.3. Activity .....	40
2.14. <i>Thermobifida alba</i> Esterase 1 ( <i>TaEst1</i> ).....	40
2.15. Lesser-known Enzymes .....	41
2.15.1. <i>Enterobacter</i> sp. HYI Esterase B ( <i>EsEstB</i> ).....	41
2.15.2. HR29 Hydrolase ( <i>BhrPETase</i> ) .....	41
2.15.3. <i>Bacillus subtilis</i> Lipase ( <i>BsEstB</i> ).....	42
2.15.4. <i>Streptomyces scabies</i> Sub1 ( <i>ScSub1</i> ) .....	42

2.15.5. <i>Pseudomonas mendocina</i> Cutinase ( <i>PmCut</i> ).....	42
2.15.6. PET1–PET13.....	42
2.15.7. <i>Thermomonospora curvata</i> Cutinases 0390 and 1278 ( <i>TcCut0390</i> and <i>TcCut1278</i> ).....	43
2.15.8. <i>Thermobifida halotolerans</i> Esterase ( <i>ThEst</i> ).....	43
3. Microorganisms with PET Degradation Activity.....	43
4. Potential PET hydrolases with activity to be confirmed .....	44
<b>B. Theoretical Background .....</b>	<b>45</b>
1. Molecular Mechanics .....	47
1.1. Force Fields .....	47
1.1.1. Bonded interaction .....	48
1.1.2. Non-bonded interactions .....	49
1.2. Molecular Dynamics (MD).....	50
1.2.1. Integration step .....	51
1.2.2. Non-bonded interactions cut-off.....	51
1.2.3. Periodic boundary conditions .....	51
1.2.4 SHAKE algorithm.....	52
2. Quantum Mechanics.....	52
2.1. Density Function Theory (DFT).....	52
2.1.1. Kohn-Sham Self-Consistent Field (SCF) .....	53
2.1.2. Exchange-correlation functionals .....	53
2.1.3. Basis Sets .....	54
2.1.4. Thermal corrections.....	55
3. QM/MM hybrid method .....	55
3.1. ONIOM.....	56
4. Gaussian software .....	57
5. ORCA .....	57
<b>C. RESULTS .....</b>	<b>59</b>

1. Plastic Biodegradation Enzyme Database .....	60
1.1. Scope .....	60
1.2. Methodology.....	60
1.2.1. Polymer.....	60
1.2.2. Enzyme .....	60
1.2.3. Organism .....	60
1.2.4. PDB code .....	61
1.2.5. Resolution (Å) .....	61
1.2.6. Year of Deposition.....	61
1.2.7. Methods .....	61
1.2.8. State .....	61
1.2.9. Substrate / Ligand.....	61
1.2.10. Mutations .....	61
1.2.11. DOI Publication.....	61
1.2.12. Chain .....	62
1.2.13. EC number and Gene name.....	62
1.2.14. Metal Ions .....	62
1.2.15. Metacyc .....	62
1.2.16. Enzymatic Activity .....	62
1.2.17. Kinetic Parameters .....	62
1.2.18. Thermostability.....	62
1.2.19. Disulfide Bond .....	63
1.2.20. Catalytic Triad .....	63
1.2.21. Oxyanion Hole .....	63
1.2.22. Uniprot.....	63
1.2.23. FASTA sequence.....	63
1.3. Results and Discussion.....	64
1.4. Conclusion and Future Works .....	67
2. <i>α</i> SMHETase Catalytic Mechanism .....	69
2.1. Scope .....	69
2.2. Methodology.....	69
2.2.1. Structure preparation.....	69

2.2.1.1. PDB analyses.....	69
2.2.1.2. Protonation states .....	70
2.2.1.3. LEaP.....	70
2.2.1.4. Molecular Dynamics Simulation.....	71
2.2.1.5. QM/MM model .....	71
2.2.1.6. Thermal corrections .....	72
2.2.1.7. Single-point calculations.....	72
2.3. Results.....	73
2.3.1. Acylation .....	73
2.3.1.1. Step 1 .....	73
2.3.1.2. Step 2 .....	75
2.3.1.3. Step 3 .....	77
2.3.2. Deacylation.....	79
2.3.2.1. Step 4 .....	79
2.3.2.2. Step 5 .....	79
2.4. Comparison with other catalytic mechanism .....	81
D. Conclusion and Future Works .....	83
E. References .....	86
F. Appendices.....	103

# Index of Figures

<b>Figure 1.</b> Synthetic polymers as stratigraphic indicators. Adapted from: The Plastocene - Plastic in the sedimentary record.....	2
<b>Figure 2.</b> Scheme of the PET polymer reaction.....	3
<b>Figure 3.</b> Scheme of the PUR polymer reaction. ....	4
<b>Figure 4.</b> Scheme of the PE polymer reaction.....	4
<b>Figure 5.</b> Scheme of PP polymer reaction. ....	5
<b>Figure 6.</b> Scheme of PA polymer reaction. ....	5
<b>Figure 7.</b> Scheme of PS polymer reaction. ....	6
<b>Figure 8.</b> Scheme of PVC polymer reaction. ....	6
<b>Figure 9.</b> Male endocrine system. In the female system is the addition of the ovaries and removal of testes. ....	8
<b>Figure 10.</b> Several conformations of residue Trp185. The catalytic triad is represented in orange and the PET substrate in red. Conformation A (PDB: 5XG0), Conformation B (PDB: 5XFY), and Conformation C (PDB: 5XJH) are represented in green, yellow, and blue, respectively. ....	13
<b>Figure 11.</b> Conformational changes of Phe415 and Gl410 upon binding to benzoic acid (BA). The apo-form structure is represented in orange (PDB: 6QZ4) while the complexed form is represented in blue (PDB: 6QZ3). ....	18
<b>Figure 12.</b> Schematic representation of <i>Pa</i> PETase secondary structure motifs represented in New Cartoon. ....	20
<b>Figure 13.</b> Fundamental <i>Pa</i> PETase amino acid residues, including the catalytic triad (in orange) the oxyanion hole (in blue) and the disulfide bonds (in yellow) represented in Licorice. The loop (in dark blue) is represented in New Cartoon. ....	21
<b>Figure 14.</b> Representation of important amino acid residues of LCC: catalytic triad (in orange) the oxyanion hole (in blue) and the disulfide bonds (in yellow) represented in Licorice. ....	23
<b>Figure 15.</b> Comparison between two different regions in <i>Tc</i> Cut1 (PDB: 5LUI), in green, and <i>Tc</i> Cut2 (PDB: 5LUJ), in blue. Region 1 and region 2 are represented in orange and grey, respectively. Amino acid residues are identified by their three-letter code. ....	32
<b>Figure 16.</b> Schematic representation of main structural aspects of <i>Fc</i> Cut5a. (A) Detailed view of the catalytic triad and oxyanion hole residues. (B) Schematic representation of the hydrogen bond	

between residues Lys63 and Asp209 (C) View of the two repulsing amino acid residues Glu165 and Asp166. ....	33
<b>Figure 17.</b> Dual-system action of <i>H</i> Cut and <i>Ca</i> LipB to fully degrade PET to TPA and EG. ....	38
<b>Figure 18.</b> Number of polymer entries. ....	66
<b>Figure 19.</b> Number of organism entries. ....	67
<b>Figure 20.</b> Number of enzymatic entries. ....	69
<b>Figure 21.</b> Representation of MHETA and MHET substrates. ....	70
<b>Figure 22.</b> Fourth minimization model with critical distances represented.....	71
<b>Figure 23.</b> Reactant (R), transition state (TS) and Product (P) structures with distances of the atoms involved in the step 1 displayed. ....	73
<b>Figure 24.</b> Energy profile of $\Delta E$ (6.90 and -0.75 kcal/mol, for activation and reaction, respectively) $\Delta G$ (4.25 and -0.59 kcal/mol) and $\Delta G + SP$ (6.44 and -1.74 kcal/mol) of step 1. ....	74
<b>Figure 25.</b> Activation and reaction energies and the contribution of HL and LL layers in step 1. ....	74
<b>Figure 26.</b> Reactant (R), transition state (TS) and Product (P) structures with distances of the atoms involved in the step 2 displayed. ....	75
<b>Figure 27.</b> Energy profile of $\Delta E$ (3.90 and 3.79 kcal/mol, for activation and reaction, respectively) $\Delta G$ (3.97 and 2.85 kcal/mol) and $\Delta G + SP$ (8.84 and 7.73 kcal/mol) of step 2. ....	76
<b>Figure 28.</b> Activation and reaction energies and the contribution of HL and LL layers in step 2. ....	76
<b>Figure 29.</b> Reactant (R), transition state (TS) and Product (P) structures with distances of the atoms involved in the step 3 displayed, confirming the proton transference.....	79
<b>Figure 30.</b> Energy profile of $\Delta E$ (0.53 and -4.38 kcal/mol, for activation and reaction, respectively) $\Delta G$ (-1.16 and -3.26 kcal/mol) and $\Delta G + SP$ (-1.12 and -6.80 kcal/mol) of step 3.....	80
<b>Figure 31.</b> Activation and reaction energies and the contribution of HL and LL layers in step 3. ....	80
<b>Figure 32.</b> Reactant (R), transition state (TS) and Product (P) structures with distances of the atoms involved in the step 5 displayed, confirming the regeneration of Ser225. ....	82
<b>Figure 33.</b> Energy profile of $\Delta E$ (8.59 and 1.57 kcal/mol, for activation and reaction, respectively) $\Delta G$ (4.13 and -0.34 kcal/mol) and $\Delta G + SP$ (8.74 and 1.95 kcal/mol) of step 5. ....	82
<b>Figure 34.</b> Activation and reaction energies and the contribution of HL and LL layers in step 5. ....	81



# Index of Equations

Equation 1. Potential energy function (Class I).....	48
Equation 2. Bonded interactions energy function.....	48
Equation 3. Potential energy function of bond stretching.....	48
Equation 4. Potential energy function of angle-bending.....	48
Equation 5. Potential energy function of dihedral angle.....	49
Equation 6. Non-bonded energy function.....	49
Equation 7. Potential energy function of electrostatic between two atoms (i and j).....	49
Equation 8. Potential energy function of van der Waals interactions between two atoms (i and j).....	49
Equation 9. Final potential energy function of the system.....	49
Equation 10. Differential equation derivative.....	50
Equation 11. Atomic position calculation using the finite integration step $\Delta t$ .....	50
Equation 12. Atomic velocity calculation using the finite integration step $\Delta t$ .....	50
Equation 13. Total number of electrons calculated by the integral of electron density $\rho(r)$ .....	52
Equation 14. Electron density calculation.....	53
Equation 15. SCF theory energy calculation according to Kohn-Sham.....	53
Equation 16. Energy calculation considering orbitals.....	53
Equation 17. B3LYP exchange-correlation energy calculation.....	54
Equation 18. GTO function in atom-centered Cartesian coordinates.....	54
Equation 19. Internal energy calculation considering a certain temperature.....	55
Equation 20. Subtractive type of hybrid method energy calculation.....	56
Equation 21. Energy calculation using the two-layered ONIOM method.....	56
Equation 22. Convergence energy calculation to CBS.....	58
Equation 23. Correlation energy calculation.....	58

# Index of Tables

<b>Table 1.</b> List of database entry examples in Plastic Biodegradation Enzyme Database.....	64
--	----

# List of Abbreviations

2PET	PET Dimer
3PET	Bis(benzoyloxyethyl) Terephthalate
ABS	Acrylonitrile Butadiene Styrene
ADHD	Attention-deficit/hyperactivity Disorder
AEI	Acyl-enzyme Intermediate
AMBER	Assisted Model Building with Energy Refinement
B3	Becke 3 Functional
B3LYP	Becke 3 and Lee, Yang and Parr Functional
BA	Benzoic Acid
BHET	Bis(2-hydroxyethyl)terephthalic Acid
CBS	Basis Set Limit
cc	Couple Cluster
CCSD(T)	Coupled Cluster Singles Doubles Perturbative Triples
CHARMM	Chemistry at Harvard Macromolecular Mechanics
CO	Carbon Monoxide
CO <sub>2</sub>	Carbon Dioxide
DEHP	Di-2-ethylhexyl Phthalate
DFT	Density-Functional Theory
DLPNO	Domain Based Local Pair Natural Orbital
DNA	Deoxyribonucleic Acid
DPB	Di-n-butyl Phthalate
EDC	Endocrine Disruptor Compound
EDTA	Ethylenediaminetetraacetic Acid
EG	Ethylene glycol
EMT	1,2-ethylene-mono-terephthalate-mono(2-hydroxyethyl) Terephthalate
EP	Epoxide
EPS	Expanded Polystyrene
fT	Free Testosterone

GAFF	General AMBER Force Field
GRAPE	Greedy Accumulated Strategy for Protein Engineering
GROMOS	Groningen Molecular Simulation package
GTO	Gaussian-type orbitals
HEB	2-hydroxyethyl Benzoate
HF	Hartree-Fock
HL	High-level
IR	Infrared
$K_{cat}$	Catalytic Constant
$K_M$	Michaelis Constant
LL	Lower-level
LYP	Lee, Yang, and Parr Functional
MC	Monte Carlo
MD	Molecular Dynamics
MFEP	Minimum Free-energy
MHEP	Mono-ethylhexyl-phthalate
MHET	Mono-(2-hydroxyethyl)terephthalic Acid
MHETA	Mono-(2-hydroxyethyl) Terephthalamide
MM	Molecular Mechanics
MP	Microplastic
NMR	Nuclear Magnetic Resonance
NP	Nanoparticle
ONIOM	Our own N-layered Integrated Molecular Orbital and Molecular Mechanics
OPLS	Optimized Potentials for Liquid Simulations
PA	Polyamide
PAA	Polyacrylic Acid
PBAT	Polybutylene Adipate Terephthalate
PBSA	Poly(butylene succinate-co-butylene adipate)
PBT	Polybutylene Terephthalate
PBT	Polybutylene Terephthalate

PC	Polycarbonate
PCL	Poly( $\epsilon$ -caprolactone)
PDB	Protein Data Bank
PE	Polyethylene
PE-HD	High Density Polyethylene
PE-LD	Low Density Polyethylene
PE-LLD	Linear Low Density Polyethylene
PE-MD	Medium Density Polyethylene
PEN	Polyethylene 2,6-naphthalenedicarboxylate
PET	Polyethylene Terephthalate
PF	Phenol-formaldehyde
PHB	Polyhydroxybutyrate
PMMA	Poly(methyl methacrylate)
PMSF	Phenylmethylsulfonyl Fluoride
PNO	Pair Natural Orbital
<i>p</i> NPB	<i>p</i> -nitrophenyl Butyrate
Pos-HF	Post-Hartree-Fock
PP	Polypropylene
PPAR	Peroxisome Proliferator Activated Receptors
PS	Polystyrene
PUR	Polyurethane
PVA	Polyvinyl Alcohol
PVC	Polyvinyl Chloride
QM	Quantum Mechanical
SCF	Self-consistent Field
$T_g$	Glass Temperature
TI	Tetrahedral Intermediate
$T_m$	Melting temperature
TPA	Terephthalic Acid
TS	Transition State

UP	Unsaturated Polyester Resin
UV	Ultraviolet
VMD	Visual Molecular Dynamics
WT	Wild Type
WTP	Water Treatment Plants

# A. Introduction

## 1. Plastic

Synthetic polymers materials are typically derived from fossil-fuel by-products (1) and composed by an enormous variety of organic polymers, such as Polyethylene (PE), Polypropylene (PP), Polyvinyl chloride (PVC), Polyethylene Terephthalate (PET), Polyurethane (PUR), Polyamide (PA) and Polystyrene (PS). Plastic was firstly produced by Leo Baekeland, which patent was granted in 1909. Since that, the production has increased drastically, reaching recently roughly 350 million tons annually (2). It is expected to reach a total of 34 billion tons by 2050 (3), of which 12 billion, are expected to be deposited in landfills or to contaminate the natural environment. This massively increase of production is due to their many advantages including its use in plastic packaging, to protect the food from getting wasted and/or contaminated; replacement of ceramics in cars and aircrafts, saving fuel and decreasing emissions; medical application (e.g., prosthesis and blood pouches); light weight, and many others. The high resistance and durability, low-cost, non-degradability and capability of being moulded when pressure and heat are applied also contributes for the high demand of plastic. Recently, these synthetic polymers are being used as stratigraphic indicators, for the Anthropocene epoch (1950 – present day) (Fig. 1) (4).

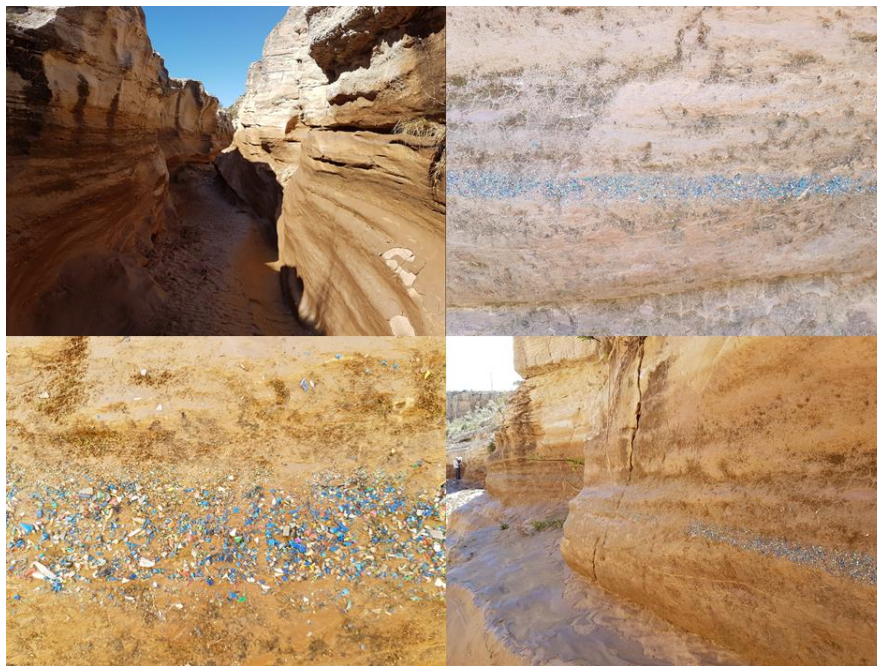


**Figure 1.** Synthetic polymers as stratigraphic indicators. Adapted from: The Plastocene - Plastic in the sedimentary record.

Although, the production of plastic has increased from 2018 to 2019 worldwide (359 vs 368 million tons), in Europe a decline of 4 million tons was observed (61.8 vs 57.9 million tons). The European demand of plastic polymers in 2020, was of 19.7% PP, 17.4% PE-LD / PE-LLD (Low Density Polyethylene



/ Liner Low Density Polyethylene), 12.9% PE-HD / PE-MD (High Density Polyethylene / Medium Density Polyethylene), 9.6% PVC, 7.8% PUR, 8.4 % PET, 6.1% PS and EPS (Expanded Polystyrene), 7.4% other plastics, such as phenolic resins, epoxide resins, urea resins, etc. Thermoplastics such as hub caps (ABS), optical fibres (PBT), touch screens (PMMA) and many others constitute 10.7% of annual production (5).

The process to produce synthetic polymers starts with the extraction of raw materials, such as oil and natural gas and their refinement into ethane and propane, using energy and water. In a process called “cracking” the ethane and propane are treated with high temperature, being converted into monomers such as ethylene and propylene. These monomers are combined with a catalyst and polymers are created. The polymers are then melted with an extruder and form a long tube as it cools down. The tube is then cut into small pellets, which are finally moulded into the final shape.

## 1.1. Types of plastic

Nowadays, several types of plastics are being produced. While some biodegradable plastics have been developed, in this section we will only be focusing on the top tier nonbiodegradable plastics.

### 1.1.1. Polyethylene Terephthalate (PET)

PET is a linear, polar, flexible polymer with variable crystallinity (amorphous to semi-crystalline) derived from crude-oil that belongs to the polyester family and is composed of repetitive units of aromatic terephthalic acid (TPA) and ethylene glycol (EG) monomers (Fig. 2). Its production involves the condensation of TPA and EG or the intermediate bis(2-hydroxyethyl) terephthalic acid (BHET) and EG (6). This synthetic polymer is used to produce bottles, cleaning products, fibres in the textile industry, etc. The main components that result from PET degradation are namely the intermediates BHET and mono-(2-hydroxyethyl) terephthalic acid (MHET) and the building blocks TPA and EG. Production of PET bottles was of 485 billion units in 2016 and estimations reveal an increase to 583 billion bottles by 2021 (2,7).

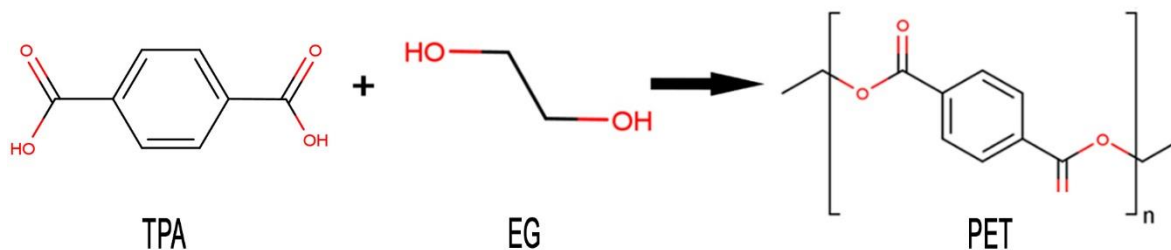


**Figure 2.** Scheme of the PET polymer reaction.

### 1.1.2. Polyurethane (PUR)

PUR is a polymer composed of organic units united by carbamate (urethane) links. They are formed by reacting a polyol with a diisocyanate or a polymeric isocyanate in the presence of suitable catalysts and additives (Fig. 3). PUR is a synthetic polymer widely used for the production of foams, insulation materials, textile coatings, paint to prevent corrosion, shoes, etc. Annually, 27 million tons of this type of polymer are produced.

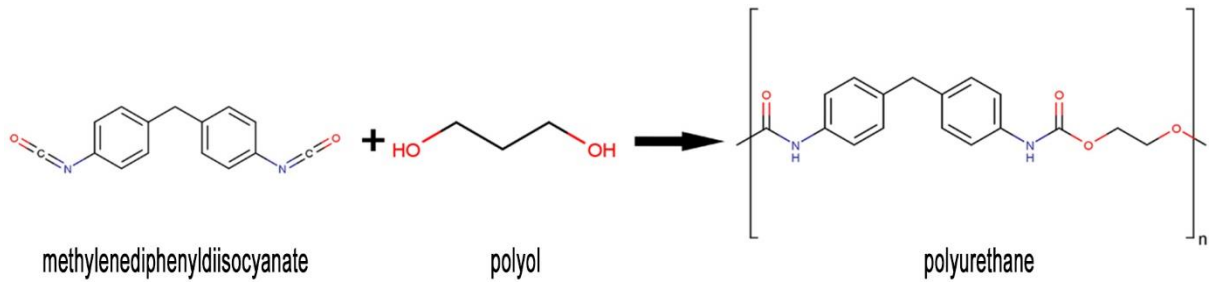


Figure 3. Scheme of the PUR polymer reaction.

### 1.1.3. Polyethylene (PE)

PE is a linear polymer with variable crystalline structure that consists of a long chain of ethylene polymers, being produced from the polymerization of ethylene monomer (Fig. 4). PE can be classified into high-density (PE-HD), medium-density (PE-MD) or low-density polyethylene (PE-LD), where there is a higher crystallinity for high-density (PE-HD) polymers. PE-LD is used to produce reusable bags, trays and containers, agricultural film used in greenhouses, food packaging film, etc. and PE-HD is used to produce toys, milk bottles, shampoo bottles, pipes, houseware, etc. (8). This is the most used polymer, with more than 100 million tons produced annually.

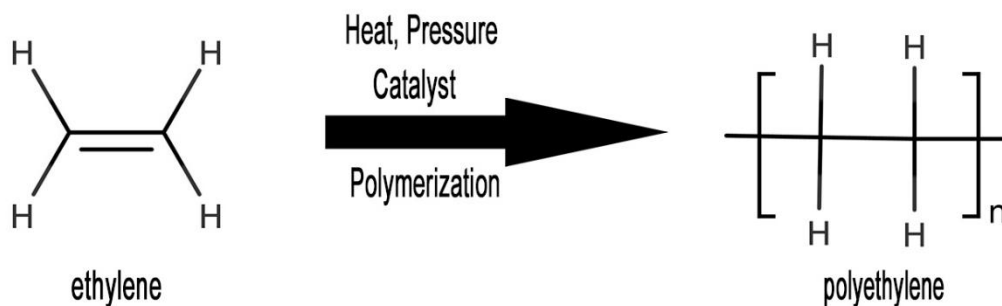


Figure 4. Scheme of the PE polymer reaction.

#### 1.1.4. Polypropylene (PP)

PP is a partially crystalline and non-polar polymer, composed of repeating units of propane-1,2-diyl units (Fig. 5). It is very similar to PE, but it is slightly harder and more heat resistant. PP is used for the production of food packaging, wrappers, hinged caps, microwave containers, pipes, automotive parts, bank notes, etc. It is the second most produced type of plastic with a production of 70 million tons, annually.

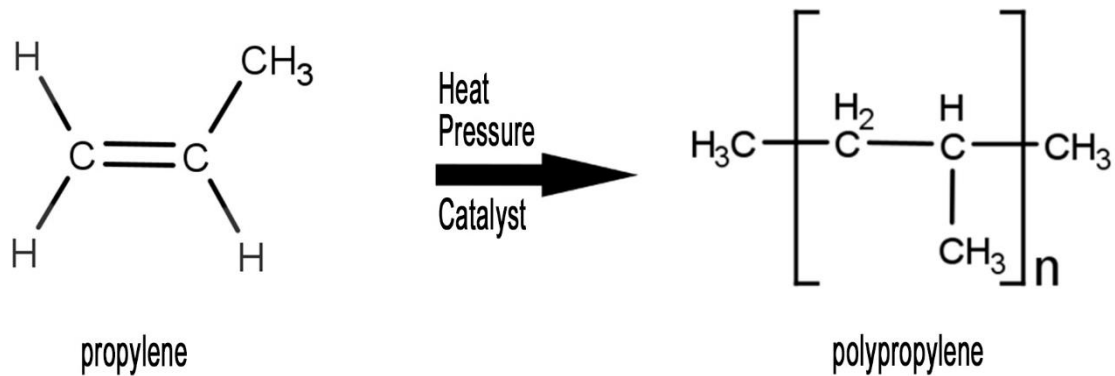


Figure 5. Scheme of PP polymer reaction.

#### 1.1.5. Polyamide (PA)

Polyamide is a polymer with repeating units of aliphatic, semi-aromatic or aromatic molecules linked by amide bonds (Fig. 6). There are many types of synthetic polyamides, the most popular being Nylon and Kevlar. This type of polymer is used in textiles, automotive applications, carpets, and sportswear. Although they are not the most produced types of plastics, compared to other polymers mentioned here, the production of these polymers can reach 10 million tons, annually.

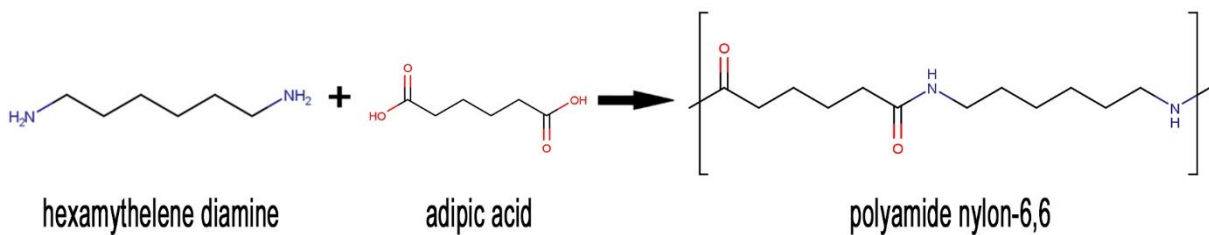


Figure 6. Scheme of PA polymer reaction.

### 1.1.6. Polystyrene (PS)

PS is a synthetic aromatic hydrocarbon polymer consisting of styrene monomers (Fig. 7). It is used for food packaging, building insulation, electrical & electronic equipment, inner liner for fridges, eyeglasses frames, etc, and 14 million tons were produced in 2016.

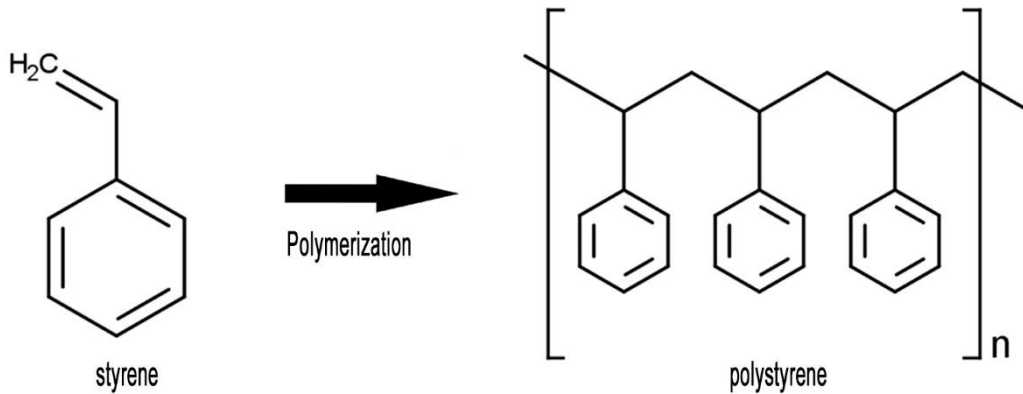


Figure 7. Scheme of PS polymer reaction.

### 1.1.7. Polyvinyl Chloride (PVC)

PVC is a polymer composed of repeating chloroethyl units and it is formed from the polymerization of vinyl chloride (Fig. 8). The polymer can be rigid and flexible, and it is used in window frames, profiles, floor and wall covering, pipes, cable insulation, garden hoses, inflatable pools, etc. It is the third most produced type of plastic with an annual production around 40 million tons.

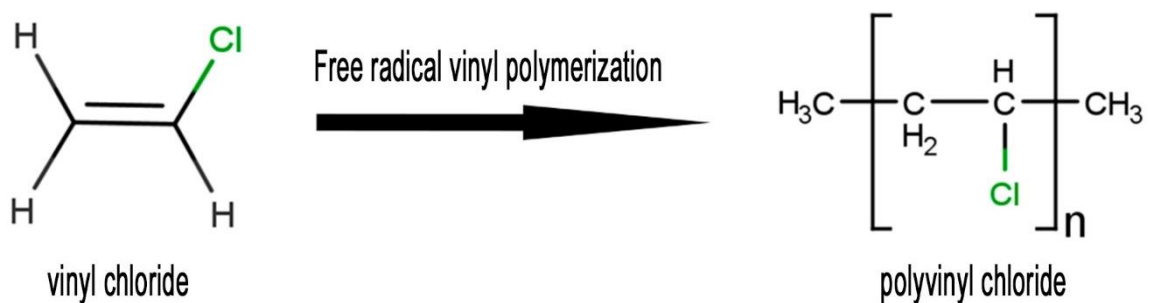


Figure 8. Scheme of PVC polymer reaction.

## 1.2. Classification of plastics

Synthetic polymers can be classified, according to their chemical composition (covalent network structure), engineering behaviour or size.

Thermoplastic polymers are defined as polymers that can be molten at certain temperatures. When heat is applied the polymers melt, and upon cooling they harden. Due to these properties of shaping and hardening, thermoplastics are mechanically recycled. Common thermoplastics are PP, PE, PVC, PS, PET and polycarbonate (PC).

Contrary to thermoplastics, thermosets are polymers that cannot be remoulded when heat is applied. These types of polymers are virtually unrecyclable, except through specialised chemical approaches. Polymers known to be thermosets are namely, PUR, epoxide (EP), phenol-formaldehyde (PF) and unsaturated polyester resin (UP).

Lastly, polymers can be divided according to their particle size. This characterization is divided in three groups namely, macroplastics, microplastics and nanoplastics. All polymers >5 mm are defined as macroplastics, the ones in the range of 100 µm – 5 mm are named microplastics and <100 µm are called nanoplastics. It is of extreme importance to set a range of plastic sizes, because of the different negative impacts that may occur according to each size.

### 1.3. Additives

In addition to the synthetic polymers, additives are used to enhance the polymer's functionality and ageing properties. These additives can be added during the shaping of the polymer, through injection moulding, blow moulding, vacuum moulding, extrusion, etc. The chemical compounds can be divided into 4 categories, and each plays a distinct role in enhancing the product. Functional additives, which are additive or auxiliary substances that are added during the manufacturing process. The most used functional additives are the ones who remove unwanted oxygen, block UV and IR radiation and eliminate or reduce static, such as stabilisers, antistatic agents, flame retardants, plasticizers, lubricants. Fillers can be used to change the properties of the original plastic and save production cost and raw materials. Examples of fillers are talc, kaolin, clay, mica, barium sulphate and calcium carbonates. Reinforcement additives can be used to increase the strength or elasticity of the product and the two most common reinforcements are the glass fibres and carbon fibres. Finally, there is colorants, which are involved in the colouring of the product (e.g., pigments, soluble azocolorants, etc.).

### 1.4. Negative impacts

The high demand and properties of synthetic polymers led to its massive production. Studies have revealed that only 9% of all plastic ever produced have been recycled, 12% incinerated and 79% accumulated in landfills or the natural environment (3). The accumulation of plastic in the landfills leads to major environmental consequences, resulting in the pollution of terrestrial, groundwater and marine

environments. Incineration is also a hazardous strategy that leads to the spreading of volatile and toxic wastes, which are potentially dangerous to the environment and human beings. In fact, in a recent study it was revealed that only in the oceans it was estimated that 4.8 to 12.7 million tons of plastic were accumulated in 2010 (9). Furthermore, 40% of plastic products have a service life lower than 1 month, creating serious environmental and management problems. In this chapter we will discuss the influence of plastic in the human health, marine and freshwater ecosystems, and atmosphere.

#### 1.4.1. Human health

One of the impacts of the excessive plastic production is the intake of hazardous chemicals that can bring many consequences to the human health. Studies have revealed that microplastics are present inside the human body due to its exposure through the nose, mouth, and skin. (10) Many pathways are involved for this to happen, such as ingestion (e.g., contaminated food stock), inhalation (e.g., airborne microplastics), direct contact with plastic materials, etc. One of the main studies on the human health is the yield of endocrine disruptors (EDCs) by plastic waste.

The endocrine system is a network of glands that are responsible for the production and secretion of hormones able to control the emotional state, growth and development, metabolism, organs, and reproduction, directly to the blood stream. The main glands that make up the endocrine system are the: hypothalamus, pituitary gland, pineal gland, thyroid gland, parathyroid, thymus, adrenals, pancreas, ovaries, and testes (Fig. 9).

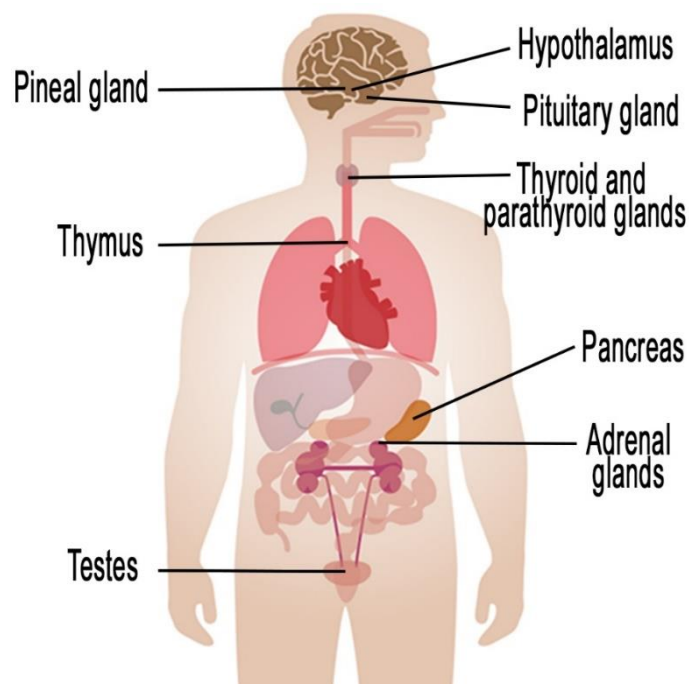


**Figure 9.** Male endocrine system. In the female system is the addition of the ovaries and removal of testes.

Disrupting the system can lead to severe hormonal disabilities. For instance, in male infants the endocrine disruption is associated with decreased anogenital distance indicating under virilization, in male adults a worse metric of fertility (damaged DNA in sperm, decreased semen volume and motility) and increased risk of testicular or prostate cancer (11,12). In females it is believed to be involved with an earlier onset of puberty and increased risks for reproductive and other endocrine related cancers, impaired oocyte competence, ovarian function or menstrual cycling and endometriosis (13–15). Although the effects of early exposures to endocrine disruptor compounds (EDCs) remain unclear, suggestions reveal that foetal or childhood exposure may lead to altered sex differentiation, neurological and reproductive development, and cancer later in life (16–18).

An EDC is any compound or substance that can interfere with hormonal systems. Phthalates, a group of chemicals that are used to make the plastic more durable are classified as endocrine disruptors (19). A study revealed that mineral water has a 12-fold higher concentration of phthalates in PET bottles when compared to samples from glass bottles (20). This means that phthalates are being leached into the mineral water from the PET bottles. The suggested reasons for this leaching are the storage conditions, where higher temperatures provide higher leaching rate, and the ineffectiveness of PET recycling process in removing organic molecules once they have been combined (21).

Urine and blood samples of male workers exposed to high levels of Di-n-butyl Phthalate (DBP) and Di-2-ethylhexyl Phthalate (DEHP) revealed a significantly elevated concentration of DBP and DEHP (644.3 and 565.7  $\mu\text{g/g}$  creatinine, respectively) when compared to the unexposed ones (129.6 and 5.7  $\mu\text{g/g}$  creatinine, respectively) (22). These high concentrations of phthalates affect the production of serum free testosterone (fT). Initially, DEHP also indicated hepatocarcinogenicity and was enlisted as a likely carcinogenic. However, later studies on primates showed that humans are resistant to the effect, withdrawing DEHP as a likely carcinogen (10).

Furthermore, phthalates are classified as metabolic disruptors and a metabolite of DEHP, named Mono-ethylhexyl-phthalate (MHEP) has been determined to interact with all three peroxisome proliferator-activated receptors (PPARs), which belong in the nuclear receptor super family. PPARs are involved in the metabolism of carbohydrate and lipids. It is likely that the exposure of several years to these metabolic disruptors may deregulate complex pathways for metabolism (10).

Airborne microplastics can be easily widespread through the wind and interact with a wide range of organisms. These plastics are mostly fibres from clothes, fragments from abraded plastic sheets and tyres and can be inhaled by humans, ending up transported to the lungs. Lung cancer and

cardiopulmonary diseases are associated with these types of plastics (23). Studies among nylon flock and textile industry workers showed that some personnel had interstitial lung disease with coughing, breathlessness, and wheezing (24). In a specific case, where the ventilation in an air spray unit was inadequate, chronic inhalation of polyacrylate nanoparticles by workers resulted in two deaths by respiratory failure (25).

Other disabilities such as diabetes, breast cancer, immune function, and metabolic disorders may be connected with phthalate exposure (26). Non-conclusive studies also relate these chemicals to adverse child neurodevelopment, including autistic behaviours, lower cognitive and motor development, and attention-deficit/hyperactivity disorder (ADHD) (27,28).

#### 1.4.2. Ecosystems

Most of the contamination by synthetic polymers originates from uncovered landfill sites, untreated sewage, wind-blown debris, and waste disposal including bottles, plastic bags, tyres, and many others (29). Generally, the plastic material starts as a macroplastic that is submitted to slow environmental degradation, releasing smaller particles (microplastics (MP) and nanoparticles (NP)), which widespread more through the ecosystems. Buried plastic in the landfill sites take decades to degrade, posing serious problems for the future.

Roughly 70–80 % of plastic materials that arrive to the oceans are from rivers, which are prevent from manufacturing processes, agriculture and wastewater treatment plants. As for marine environment the contamination source is provided from shipping, oil and gas platforms and fishing (e.g., discarding nets). These plastic leaching to aquatic environments can cause chemical and physical damages to the aquatic species (29).

Macroplastic contamination in the marine environment generally affects large animals such as turtles that can mistake plastic bags for their preferred diet of jellyfish (29). Furthermore, other physical factors such as, asphyxiation or blocking of the digestive tract and entanglement, which leads to impairment of regular activities can be potentially lethal. Much of the microplastic debris in this environment have similar sizes and appearances to microorganisms, such as zooplankton and can be regarded as prey, ending up consumed by predators.

Studies suggest that freshwater fish are more vulnerable to microplastic pollution than seawater fish (30). Furthermore, analysis in the river Thames in London revealed that up to 75% of the bottom feeder European flounder, *Platichthys flesus*, had MPs in the gut, while only 20% of the predator European smelt,



*Osmerus eperlanus*, indicated ingestion of microplastics. This reveals that the bottom feeders ingest more microplastic and as the chain goes up this concentration is lower (31).

Analysis of soft tissues from grown blue mussels and the giant Pacific oyster showed an average of  $36 \pm 7$  and  $47 \pm 16$  particles/100 g wet weight of microplastic levels, respectively. Shellfish are consumed by humans and is estimated that roughly 11,000 microplastic particles/year are ingested from shellfish only (32,33).

An analysis of treated water for consumption showed that the water is still contaminated with plastic ( $338 \pm 76$  to  $628 \pm 28$  particles L<sup>-1</sup>) even after the treatment, meaning that the plastic removal system of Water Treatment Plants (WTP) is insufficient.

### 1.4.3. Atmosphere

The largest scrap of plastic waste still ends up in dumpsites or is openly burned, causing the emission of carbon monoxide (CO) and carbon dioxide (CO<sub>2</sub>), which contribute to global warming. Furthermore, in plastic recycling industry a large share of plastic waste is used for energy recovery. The uncontrolled combustion of the plastic waste, especially halogens such as PVC and additives such as brominated flame retardants can lead to the emission of hazardous substances namely, acid gases and dioxins, which are organic pollutants (34). Chemical degradation methods, such as glycolysis, methanolysis, hydrolysis, aminolysis and ammonolysis, have been developed to remove plastic waste and promote the recycling of plastic-based materials. However, these chemical degradation methods are very expensive, requiring high temperatures (usually 200–425 °C, possibly reaching 1000 °C) (35) and sometimes organic solvents are necessary, which causes additional environmental pollutants. Although some cascading processes involve an innovative use for plastic waste (e.g., asphalt), these are untested and can potentially be associated to unknown pollution (36).

Therefore, it is necessary to develop more environmentally friendly strategies. One solution that has been under development is the use of biocatalysts, such as enzymes.

## 2. Biodegradation solution

Enzymes can potentially catalyze reactions with rates comparable to current methods, but with temperatures that are drastically lower (40–80 °C), and without the need of using organic solvents. With this strategy, the generation of non-environmentally friendly residues is greatly reduced. However, for that to happen, their catalytic efficiency and stability need to be improved, which requires a detailed knowledge on their mechanism of action.

PET exhibits a glass temperature ( $T_g$ ) of 76 °C and to make the polymer more accessible for enzymatic mediated biodegradation, it is key that the enzyme remains stable at temperatures higher than 76 °C. The point when there is an equilibrium between protein folding and unfolding is called melting temperature ( $T_m$ ) and is associated with stability and catalytic ability.

In this section, detailed information on known enzymes with ability to catalyze the PET plastic will be described including features such as enzymatic PET activity, melting temperature, active site amino acid residues, mutagenesis and kinetic parameters.

## 2.1. *Ideonella sakaiensis* PETase (*IsPETase*)

### 2.1.1. Discovery

*IsPETase* was first identified from a novel microbial consortium called *Ideonella sakaiensis* 201-F6 that is formed on PET film by Yoshida et al. (37) in 2016. The enzyme is capable of assimilating PET as a major energy and carbon source and is responsible for degrading PET to MHET as a major product and EG, TPA and BHET as secondary products (37,38). When compared to previously identified enzymes *ThCut*, LCC and *FsCut*, *IsPETase* revealed higher activity against PET film with a 120, 5.5 and 88-fold increase at 60 °C and pH 7, respectively. Moreover, when the organism was confirmed to have the ability to degrade PET films one other enzyme was uncovered to be involved - *IsMHETase*. The fact that *IsPETase* showed low activity against aliphatic esters when compared to the previously mentioned enzymes, indicates the preference for PET.

### 2.1.2. Structure

*IsPETase* is a functional monomer (39) that has a molecular mass of 30.1 kDa and is composed of 290 amino acid residues. Its three-dimensional structure has been explored by several experimental, computational and structural studies (38–40). The enzyme adopts a canonical  $\alpha/\beta$ -hydrolase fold with nine mixed  $\beta$ -strands that compose a central  $\beta$ -sheet, surrounded by seven  $\alpha$  helices (39). At the active site, the catalytic triad is composed of Ser160, His237 and Asp206 residues that are found in a broad active site cleft (38).

Two disulfide bonds are present in the enzyme Cys203–Cys239 and Cys273–Cys289 (39). The second disulfide is located near the C-terminal (distant from the active site) and is conserved amongst all known PET hydrolyzing enzymes. Even though the bond is distant from the catalytic center, disulfide bonds have crucial roles in the structural integrity of the enzyme and is associated with high enzymatic stability. The first disulfide is located near the active center, which connects  $\beta$ -strand 7 to a loop connecting  $\beta$ -strand

8 and helix  $\alpha$ 5. Because of its specificity and location, the disulfide bond is believed to be one of the motifs responsible for the increased activity of *Is*PETase when compared to other PET degrading enzymes (40,41).

Trp185 is a conserved residue that assumes several conformations (Fig. 10). These different conformations only appear in *Is*PETase (38,40). Induced fit Docking and molecular dynamics further confirms the flexibility of Trp185. In *Is*PETase the surrounding amino acid residue is a serine (Ser214) while in homologous enzymes is a histidine. This serine allows the Trp185 conformations to be accommodated in the catalytic site (40).

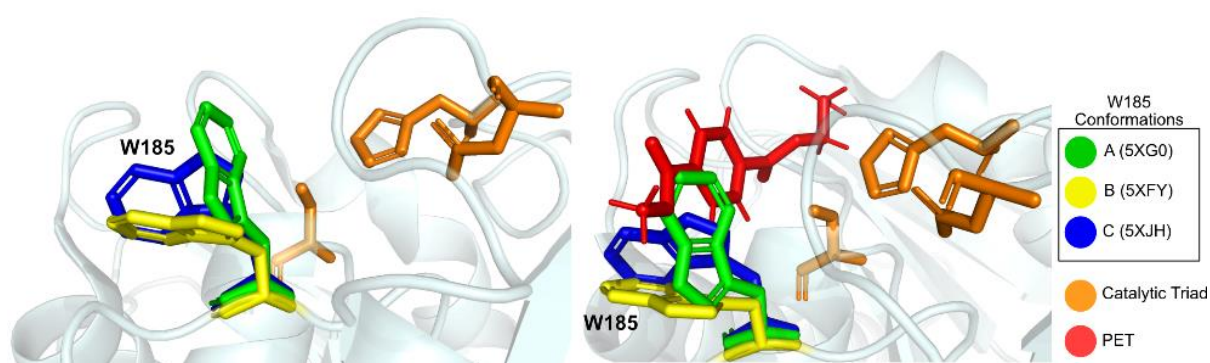


**Figure 10.** Several conformations of residue Trp185. The catalytic triad is represented in orange and the PET substrate in red. Conformation A (PDB: 5XG0), Conformation B (PDB: 5XFY), and Conformation C (PDB: 5XJH) are represented in green, yellow, and blue, respectively.

At this point of time, there are 25 structures available in the Protein Data Bank (42) and includes, apo, complexed, mutated and wild type form. Han et al. (40) determined the first *Is*PETase structures in 2017. The apo-structure was solved at 1.58 Å (PDB: 5XG0) and reveals the descriptions previously stated. The authors attempted to obtain co-crystallized structure with wild type (WT) *Is*PETase and different ligands, however they were unable to do so. Thus, a double mutation was implemented in Ser160 (catalytic serine) and Arg132, with a replacement of these residues with alanine and glycine, respectively turning the enzyme inactive. The produced structures were complexed with substrate (PDB: 5XH3) and product (PDB: 5XH2) analogues, with resolutions of 1.30 and 1.20 Å, respectively. These mutations were also applied in the apo-form to verify if the overall enzymatic fold and structure were unaffected.

Joo et al. (39) solved several *Is*PETase structures since 2017. The group performed molecular docking with 2-HE(MHET)<sub>4</sub>, a molecule that mimics a 4-moiety PET chain using the apo-form with resolution of 1.54 Å (PDB: 5XJH) (39). The first moiety binding confirmed the catalytic triad comprised by Ser160, His237 and Asp206 and the oxyanion hole, which is composed of Tyr87 and Met161. Moreover, the

docking of a longer molecule revealed that the binding site is mostly hydrophobic. The author also states that the binding site is divided into two subsites – subsite I, which is defined by Tyr87, Ile208, Met161 and Trp185 and subsite II, defined by Thr88, Ala89, Trp159, Ile232, Asn233, Ser236, Ser238 and Asn241. Subsite II is further subdivided into subsites IIa, IIb, and IIc. One of the PET moieties binds the catalytic center in subsite I, which is aided by Met161 and Ile208, while the remaining moieties are accommodated by subsite II through mostly hydrophobic interactions (39).

### 2.1.3. Activity

Several studies regarding activity and mutagenesis of *h*PETase have confirmed the role of many amino acid residues, especially the ones of the active site.

The melting temperature ( $T_m$ ) of the enzyme was determined to be 48.81 °C, which is below the  $T_g$  of PET (43). Therefore, engineering efforts to increase the enzymatic activity were paired with engineering efforts to improve the enzymes' thermal stability and durability (44).

Mutagenesis of the catalytic triad with alanine (S160A, H237A, and D206A) resulted in a complete loss of enzymatic activity, confirming their essential role (39,41). The disulfide bond (Cys203–Cys239) was mutated with serine (C203S–C239S), disrupting the bridge. The variant resulted in very low activity and a decrease  $T_m$  by over 10 °C, confirming their critical role in both activity and stability (39,40). Nearly all studies regarding the oxyanion hole and substrate interacting residue Tyr87 with several substrates (PET bottle, PET film and BHET monomers) resulted in loss of activity and reduced amount of products released (39,40,45). Trp185 was also replaced with an alanine, which resulted in a significantly decrease of activity (38–41). A residue thought to influence the flexibility of Trp185 is Ser214, which has been engineered to a histidine (conserved in other PET hydrolases) in two different studies. However, the results are non-consensual (40,41).

Binding site residues were also a target for engineering approaches. Ile208, Trp159 and Thr88 were mutated to alanine residues, resulting in decrease of enzymatic activity, revealing the importance of these enzymes in catalysis (40). Moreover, Joo et al. (39) replaced Trp159, Ser238 and Asn241 also with alanine that resulted in reduced activity. The group also simulated the *Tf*Cut2 binding site, where Ser238 was replaced with a phenylalanine (S238F) and Trp159 with a histidine (W159H) that resulted in drastic activity consequences. Interestingly, Arg280, a residue located ~23 Å away from the catalytic center, was mutated to alanine and presented an enhancement of enzymatic activity against PET film by 22.4% in 18 h and 32.4% in 36 h, when compared with the WT enzyme. These observations reveal that conformational changes away from the active site can impact the enzymatic activity. Later, the group found that Pro181

disrupts the secondary structure of the enzyme, indicating a negative effect on enzymatic thermal stability and catalytic efficiency (43). Therefore, the variant P181A was produced. However, it resulted in diminished activity at 30 and 40 °C and only increased the  $T_m$  value by 0.5 °C. After inspecting the P181A structure (PDB: 6IJ5) the group observed that the mutation caused the shifting of Asp206 away from His237, collapsing that way the catalytic site. Inspired again by *TCut2* the group produced the double mutant S121D/D186H to increase the stability of the  $\beta_6$ – $\beta_7$  loop. As expected, the mutation increased the  $T_m$  value by roughly 7 °C (56.02 °C) and an activity increase of 2.2- and 2.6- fold after 24 and 72 h, respectively, at 30 °C, and a 4.7 and 6.0-fold increase after 24 and 72 h, respectively, at 40 °C. The authors produced two triple mutants with the previous findings – S121D/D186H/R280A and S121E/D186H/R280A. The  $T_m$  measurements were 56.41 and 57.62 °C (7.6 and 8.81 °C higher than WT *sPETase*), respectively. The second variant also showed higher enzymatic activity, with a 4.3 and 5.2-fold increase after 24 and 72 h, respectively, at 30 °C and 9.1 and 13.9-fold increase after 24 and 72 h, respectively, at 40 °C.

In the latest study by the group, they performed molecular docking experiments with a 2-HE(MHET)<sub>4</sub> molecule and several point mutations were designed. Most mutations led to lower activity (45). However, S242T and N246D variants significantly increased the activity. Thus, these mutations were incorporated into the previously described triple mutation. The quadruple S121E/D186H/N246D/R280A exhibited a decrease in activity and thermal stability when compared to the triple variant due to R280A and N246D being non-compatible. By producing triple mutant variants of these single variant, it was concluded that N246D had more beneficial effects for enzymatic activity and thermal stability. Therefore, the quadruple S121E/D186H/S242T/N246D mutant was developed (PDB: 6KUS). This variant demonstrated a 58-fold increase in activity than WT *sPETase* at 37 °C, increasing the degradation activity up to 20 days.

Austin et al. (38) based in a cutinase-like active site cleft produced the double variant S238F/W159H. This variant showed an increase in product release (higher enzymatic activity) and crystallinity reduction against PET film than WT *sPETase*. After performing induced fit docking the group realized that Phe238 performed stabilizing aromatic interactions with the substrate and other amino acid residues of the active site.

So far, the best performing *sPETase* variant was developed by Cui et al. (46) using a novel computational strategy named GRAPE (Greedy Accumulated Strategy for Protein Engineering) (47). The strategy employs a cluster of optimized mutations, creating several functional variants. Using a clustering model (*K-means algorithm*) the group produced the most successful variant - DuraPETase

(S214H/I168R/W159H/S188Q/R280A/A180I/G165A/Q119Y/L117F/T140D). This variant exhibited a 300-fold activity increase in 10 days of incubation with crystalline PET at 37 °C and an increase of  $T_m$  by 31 °C. Moreover, DuraPETase remained active and functional for up to 3 days when incubated at 60 °C. The variant also showed ability to degrade nano and microplastics higher than that shown by WT *IsPETase*. Furthermore, the enzyme showed less specificity than the WT enzyme towards PET and is able to degrade other types of plastics such as polybutylene terephthalate (PBT) and polyethylene 2,6-naphthalenedicarboxylate (PEN). The solved three-dimensional structure of DuraPETase (PDB: 6KY5) at 1.63 Å allowed the understanding of the enhancement of enzymatic activity. The highlighted features were novel electrostatic interactions (T140D, I168R, W159H and S188Q), improved hydrophobic packaging (Q119Y, A180I, S214H, R280A and L117F), reduction of conformational entropy (G165A) and additional stabilization of the typical binding mode (L117F and Q119Y) (46).

Chen et al. (48) built a whole biocatalyst of PET functionalized on the surface of *Pichia pastoris* yeast cell in order to enhance *IsPETase* activity and stability. Assays have shown a 36-fold increase in activity (determined by measuring the amount of MHET product produced) towards PET films for 18 h at pH 9 and 30 °C. Moreover, the complex system showed degradation ability against commercial highly crystalline PET bottles, indicating a promising direction for *IsPETase* activity increase and wider industrial applicability.

Moog et al. (49) and Kim et al. (50), inspired by the advantages of using microalgae for expression and production of plastic degrading enzymes employed *P. tricornutum* and *C. reinhardtii* microalgae, respectively for *IsPETase* production. In both studies it was observed *IsPETase* activity with morphological changes on PET substrate and production of TPA, suggesting that using microalgae for *IsPETase* expression and its introduction in the environment is a promising strategy.

#### 2.1.4. Proposed mechanism

Presently, the most accepted mechanism starts with the binding of *IsPETase* to the substrate, in which one moiety binds to the subsite I and three onto subsite II, as previously stated. This is only allowed due to the presence of a shallow cleft on the apo-form enzyme (39,40).

Upon binding, the considered mechanistic proposal suggests as a first step a charge-relay system between Asp206 and His237, which allows His237 to deprotonate the hydroxyl group on Ser160 that becomes a stronger nucleophile and attacks the carbonyl group of the PET ester (44). This attack leads to the formation of a tetrahedral intermediate that is stabilized by the oxyanion hole. However, the negative charge of the intermediate is highly unstable and breaks down, resulting in the first product released and

in a formation of an acyl-enzyme intermediate (40,44). This acyl-enzyme intermediate is subjected to nucleophilic attack by a water molecule that is deprotonated by the same Asp206-His237, resulting in the formation of a second tetrahedral intermediate, which is equally unstable and breaks down, releasing the second product. This step concludes the full regeneration of the catalytic triad, and the system is ready for another cycle (40,44).

## 2.2. *Ideonella sakaiensis* (*Is*MHETase)

### 2.2.1. Discovery

*Is*MHETase is the other PET hydrolyzing enzyme identified in *Ideonella sakaiensis* 201-F6 by Yoshida et al. (37) in 2016 that further degrades the PET intermediate MHET into EG and TPA. The enzyme is intracellular and is comprised by 603 amino acids. The molecular weight is about 65 kDa. According to the ESTHER database, the enzyme is labelled as a tannase that belongs in the  $\alpha/\beta$ -hydrolase Block X family (51).

### 2.2.2. Structure

Structural studies of *Is*MHETase reveal that the enzyme only exists as a functional monomer (52). The catalytic domain adopts an  $\alpha/\beta$ -hydrolase fold, identical to other serine hydrolases and a lid domain composed of ~240 amino acid residues, involving the active site and a Ca<sup>2+</sup> binding-site. The Ca<sup>2+</sup> binding-site is thought to increase the lid domain stability (53).

The enzyme presents five conserved disulfide bonds (Cys51–Cys92, Cys224–Cys529, Cys303–Cys320, Cys340–Cys348, and Cys577–Cys599) (54). The one bridging Cys224–Cys529 is located at the active site, flanking the catalytic triad (Ser225, His528 and Asp492) and the oxyanion hole (Gly132 and Glu226). This bond most likely tightens the catalytic triad, increasing the enzymatic stability.

The first crystallographic structures of *Is*MHETase were determined in 2019 by Palm et al. (55) in the apo-form (PDB: 6QG9) with 2.05 Å and complexed with benzoic acid (PDB: 6QGB) and mono-(2-hydroxyethyl) terephthalamide (MHETA) (PDB: 6QGA) with resolutions of 2.2 and 2.1 Å, respectively. The authors revealed that *Is*MHETase binds to MHETA, which is a non-hydrolyzable analogue of MHET, through hydrophobic contacts between the  $\alpha/\beta$ -hydrolase residues Phe495, Gly132 and Ala494 and the phenyl ring of the substrate. Identically, the residues from the lid domain Phe415, Leu254 and Trp397 also establish hydrophobic contacts with the phenyl ring. Other studies confirmed the same binding mode towards MHET (52,54).

When comparing the apo and complexed form it is possible to observe that Phe415 undergoes an induced-fit conformational change, where it is pointing in the opposite way (open position) from the active site when the enzyme is in the apo form, promoting that way the substrate binding, and pointing towards the active site (closed form) when bonded with the substrate. Knott et al. (54) determined that Gln410 also shows a concerted movement, pivoting towards the active site when Phe415 is in the open position (Fig.11). Further analysis showed that Arg411 and Ser416 establish hydrogen bonds with the carboxylate motif of MHET.

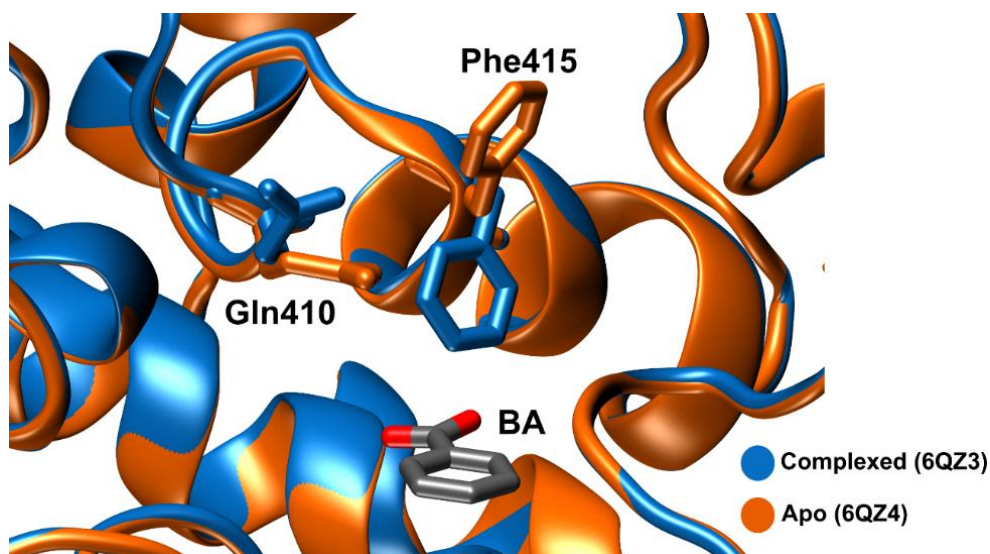


**Figure 11.** Conformational changes of Phe415 and Gln410 upon binding to benzoic acid (BA). The apo-form structure is represented in orange (PDB: 6QZ4) while the complexed form is represented in blue (PDB: 6QZ3).

### 2.2.3. Activity

It was to be expected that *s*MHETase had a relatively high  $T_m$  due to the presence of five disulfide bonds, however it was determined to be only 50.61 °C. The enzyme showed a high affinity and activity for MHET, resulting in a  $K_m$  (binding affinity constant) and  $k_{cat}$  (turnover numbers) of 7.2  $\mu$ M and  $27.6 \pm 2.6$  s<sup>-1</sup> (38,54), respectively and is incapable of efficiently degrade the other PET intermediate BHET, resulting in a  $k_{cat}$  of  $0.0011 \pm 0.0002$  s<sup>-1</sup> (55). The replacement of the catalytic triad by an alanine (S225A, His528A and D492A) revealed a total loss of activity, confirming their crucial role in catalysis (54,55). Furthermore, the mutation of the oxyanion hole amino acid residue Glu226 with a threonine (E226T) resulted in an activity loss of ~50% (54).

Several engineering efforts were produced to increase the *s*MHETase performance (activity and stability). Determined to be involved in the substrate binding, the amino acid residue Trp397 was mutated with the hydrophobic residue alanine (W397A), resulting in enhancement of activity towards MHET substrate (55).



Like previously stated, Arg411 establishes hydrogen bonds with the carboxylate motif of MHET. The mutations of this amino acid residue with the more hydrophobic residue alanine, the positive charged amino acid lysine and polar amino acid glutamine (R411A, R411K and R411Q, respectively). As expected, the variants resulted in impaired activity and affinity towards MHET. However, the variant R411K increased the activity against BHET by 1.7-fold when compared to WT *MsMHETase* (52,55).

Interestingly, a mutation of the residue that undergoes induced-fit conformational change to histidine (F415H) resulted in an enhancement of turnover rate against MHET, while the other variants (F415A and F415S) exhibited lower turnover rate and affinity or lower activity towards MHET (55). Phe424 is located at the inner substrate binding-site and is potentially hindering the optimal BHET binding. Therefore, several variants were produced (F424Q, F424N, F424H, F424D, F424E, F424T, F424V, F424L, F424I, F424A, and F424S). Expectedly, all variants resulted in higher turnover rates and activity, especially F424N, F424V, F424I, and F424Q (55). A hypothesis of the enzyme having a catalytic tetrad was ruled out when the variant His488 (H488A) resulted in unaltered turnover rate (55).

Knott et al. (54) removed the lid domain of *MsMHETase* (Gly251–Thr472) and replaced it with a *MsPETase* loop residues (Trp184–Phe191) to possibly confer *MsMHETase* the ability to degrade PET. However, this was not possible, and the variant resulted in a 1000-fold decrease of turnover rate against MHET when compared to WT *MsMHETase*. The group also disrupted the disulfide bond located in active site with tryptophan and serine (C224W–C529S) or histidine and phenylalanine (C224H–C529F), which almost conferred a complete loss of activity against MHET, with  $k_{cat}$  values of  $0.10 \pm 0.06 \text{ s}^{-1}$  and  $0.06 \pm 0.03 \text{ s}^{-1}$ , respectively. Finally, the group added two other disulfide bonds – one from PETase-like (G489C–S530C) and other from modified *AoFaeB* (S136C with 15-residue loop), making a total of seven disulfide bonds. The variant was successfully expressed however, had very low activity towards MHET, with a  $k_{cat}$  of only  $0.10 \pm 0.06 \text{ s}^{-1}$ .

#### 2.2.4. Proposed Mechanism

Knott et al. (54) proposed a catalytic mechanism of *MsMHETase*, based on quantum mechanical/molecular mechanical (QM/MM) approach with 2D umbrella sampling. The resulting structure suggests that the enzyme follows a classical serine hydrolase mechanism.

The catalysis of MHET involves a two-step reaction – acylation and deacylation. The acylation starts when His528 deprotonates Ser225, which becomes a nucleophile that readily attacks the carbonyl of MHET, resulting in formation of an acyl-enzyme intermediate (AEI) and the release of the EG product, that exits within 4 ns after the formation of AEI. The minimum free-energy path (MFEP) that is calculated from the

formed C–O bond between the MHET carbonyl and Ser225, predicts an acylation free-energy barrier ( $\Delta G^\ddagger$ ) of  $13.9 \pm 0.17$  kcal/mol with an overall reaction free energy ( $\Delta G$ ) of  $-5.2 \pm 0.04$  kcal/mol. A nucleophilic water molecule, which is deprotonated again by His528 attacks the AEI, resulting in the release of the second product TPA and transfers the proton to the catalytic Ser225, regenerating it for a new catalytic cycle. MFEP predicts a deacylation  $\Delta G^\ddagger$  of  $19.8 \pm 0.10$  kcal/mol and  $\Delta G$  of  $2.60 \pm 0.07$  kcal/mol, resulting in an exergonic reaction ( $-2.60 \pm 0.08$  kcal/mol). Furthermore, deacylation seems to be the rate-limiting step, due to the very low calculated  $k_{cat}$  ( $7.1 \pm 1.1 \times 10^{-2}$  s $^{-1}$ ) when compared to the one from acylation ( $1.02 \pm 0.28 \times 10^3$  s $^{-1}$ ) (54).

### 2.3. *Pseudomonas aestusnigri* PETase (*Pa*PETase)

#### 2.3.1. Discovery

*Pa*PETase, frequently known as PE-H, was first identified by Bollinger et al. (56) in 2017. The enzyme is produced by the gram-negative rod-shaped bacteria *Pseudomonas aestusnigri*, a novel species isolated from a marine area where a large oil spill occurred in the last decade (57). Studies of the bacterial genome sequence revealed a potential hydrolase coding gene, which coded for functional PET hydrolase. Indeed, WT *Pa*PETase degrades amorphous PET films. The enzyme is also capable to degrade BHET to MHET, without the production of TPA (58,59).

#### 2.3.2. Structure

*Pa*PETase is constituted by 304 amino acid residues plus a signal peptide of 25 amino acids, making a total of molecular weight of 32 kDa. Bollinger et al. (56) solved the first and only crystallographic structures, that revealed a functional monomer with the typically conserved  $\alpha/\beta$ -fold, which is composed of nine  $\beta$ -strand central twisted  $\beta$ -sheet and seven  $\alpha$ -helices on both sides (Fig. 12).

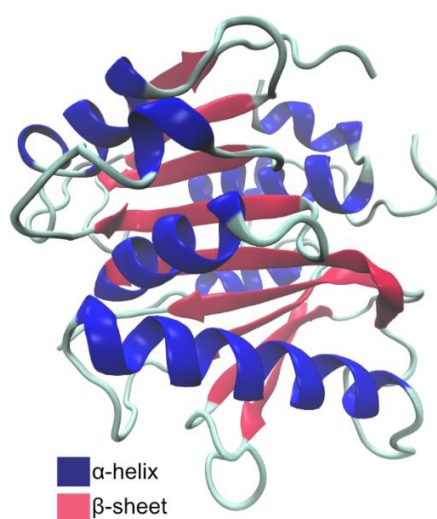


**Figure 12.** Schematic representation of *Pa*PETase secondary structure motifs represented in New Cartoon.

The catalytic site is found right below the surface and is comprised by Ser171, His249, and Asp217. Ser171 occupies the traditional position in the nucleophilic elbow. The oxyanion hole is composed of Met172 and Phe98 and stabilizes the substrate during the reaction. Furthermore, two disulfide bonds (Cys214–Cys251 and Cys285–Cys302) are present, with the first flanking the catalytic triad. Also, it was identified an extended loop region (Gly254, Gly255, Ser256, Ile257, Tyr258, and Asn259) connecting  $\beta 8$ – $\alpha 6$  similar to *h*PETase (Ser242, Gly243, Asn244, Ser245, Asn246, and Gln247) (Fig. 13). Additionally, Tyr250 was determined to be the equivalent to *h*PETase Ser238, an important residue in catalysis. Moreover, interactions between this amino acid and Glu102 seems to be responsible for the tightening of the active site (56).

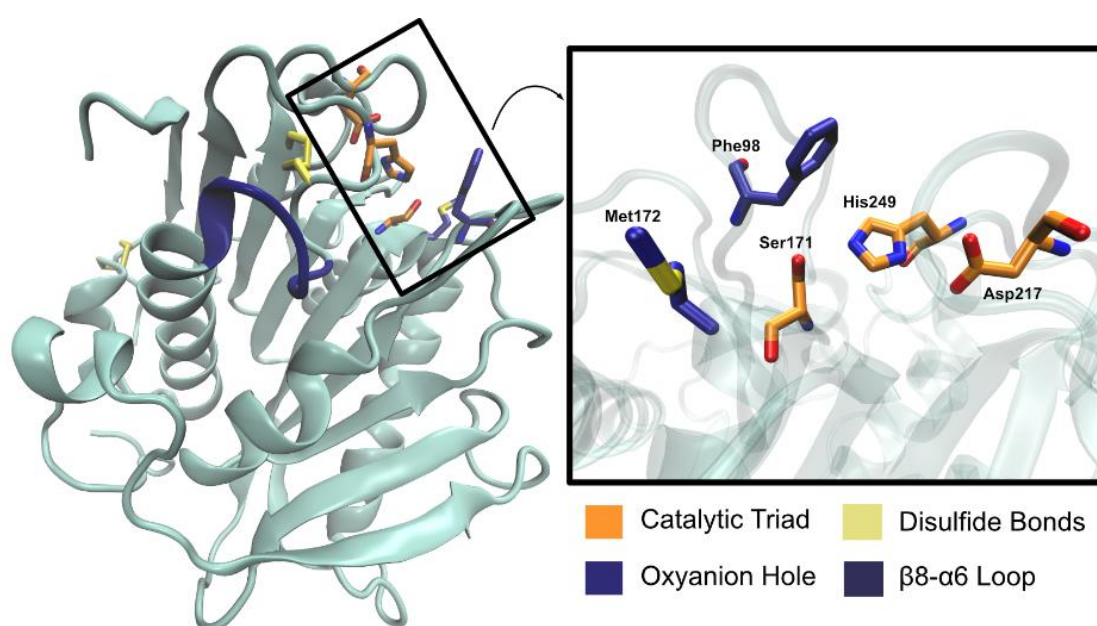


**Figure 13.** Fundamental *Pa*PETase amino acid residues, including the catalytic triad (in orange) the oxyanion hole (in blue) and the disulfide bonds (in yellow) represented in Licorice. The loop (in dark blue) is represented in New Cartoon.

### 2.3.3. Activity

In the same study, Bollinger et al. (56) observed that WT *Pa*PETase is able to degrade BHET and amorphous PET to MHET, with nearly no production of TPA. The degradation of amorphous PET resulted in the production of 4.2 ( $\pm$  1.6) mg/L MHET after 40 h at 30 °C. However, the enzyme was unable to hydrolyze a commercial PET bottle film. Mutations on the amino acid residues that comprise the extended loop were produced and tested for BHET and PET activity. G254S, Y258N, N259Q, and the entire loop variants resulted in significantly decreased activity and lower  $T_m$  when compared to WT enzyme by 5–10 °C. Furthermore, S256N and I257S also resulted in lower activity but with less drastic decrease of  $T_m$ , by 1–3°C. Although Y250S equally showed a decrease in  $T_m$  by 1° C, the activity against *p*NPB, BHET, and PET was higher. The variant yielded 5.4 ( $\pm$  0.6) mg/L of MHET after 48 h at 30 °C against amorphous

PET film, while WT *Pa*PETase yielded about 4.2 ( $\pm$  1.6) mg/L. Unlike WT *Pa*PETase, the variants Y250S and S256N were able to degrade commercial PET, although with a relative low amount of MHET.

The structure of the variant Y250S (PDB: 6SCD) demonstrated a wider and spacious catalytic site cleft than WT *Pa*PETase (PDB: 6SBN). In the WT enzyme, two loop regions (loop composed of residues Phe98–Ser104, that connects  $\beta$ 3– $\alpha$ 2 and the loop composed of residues Asp123–Phe128, that connects  $\beta$ 4– $\alpha$ 3) are parallel to each other, while in the variant structure, these loops are conformed against each other, which allows the more space in the active site. By disrupting the interaction of Tyr250 and Glu102 with the variant Y250S, the active site cavity becomes larger (from 153 Å<sup>3</sup> to 362 Å<sup>3</sup>), which results in a deeper and more accessibility for the substrate, contributing that way to the enhancement of the hydrolytic activity (56).

Through molecular docking studies the group predicted the enzyme-binding mode with 2-HE(MHET)<sub>4</sub>, MHET, and BHET on both structures. BHET and MHET were bounded and stabilized by Ser256, Ser248, Asp106, and Ser104, in a groove adjacent to the catalytic triad. However, this binding position was not optimal for catalysis. With the engineered variant Y250S the structure was found to have a more favourable binding mode for BHET and MHET, being in an appropriate distance for Ser171 nucleophilic attack. No valid binding mode for 2-HE(MHET)<sub>4</sub> was found for both structures (56).

#### 2.3.4. Proposed Mechanism

Bollinger et al. (56) after their structural and computational studies suggest a three-moiety substrate binding mode with one unit binding the catalytic site adjacent groove and the other two bridging the distance to the catalytic site. The last unit would bind at an optimal distance for a serine attack.

### 2.4. LC-Cutinase (LCC)

#### 2.4.1. Discovery

LCC is a secretory protein with high sequence to cutinases and lipases and was first identified and isolated from a leaf-branch compost through metagenomic approach in 2011 (60). However, the source organism is yet to be identified. Due to its high sequence identity to bacterial cutinases (57.4% sequence identity to *Thermobifida fusca*) it is suggested that the source organism is a thermophilic bacterium (61). The enzyme was found to efficiently degrade PET and depolymerize poly( $\epsilon$ -caprolactone) (PCL) (60).

#### 2.4.2. Structure

LCC revealed to be composed of 258 amino acid residues with a molecular mass of 28 kDA, plus a 34-residue signal peptide (60,61). The enzyme adopts a  $\alpha$ / $\beta$ -hydrolase fold, which is composed of nine

stranded  $\beta$ -sheet and eight  $\alpha$ -helices (61). In the catalytic site, the catalytic triad is found to be comprised by Ser165, His242 and Asp210, and the oxyanion hole by Met166 and Tyr195 (Fig. 14). Ser165 is located in a nucleophilic elbow between  $\beta$ 5– $\alpha$ 5 (60). A disulfide bond (Cys275–Cys292) is present and is responsible for anchoring the C-terminus to a  $\beta$ 9– $\alpha$ 8 loop, similar to other PET hydrolytic enzymes. This bridge is typical in thermophilic bacterial cutinases, which goes in the accordance with the previous prediction (60).

Currently, all known three-dimensional structures exists in the apo-form. The first structure (PDB: 4EB0) was solved with a resolution of 1.5 Å by Sulaiman et al. (60), in 2012 that allowed the confirmation of structural features.

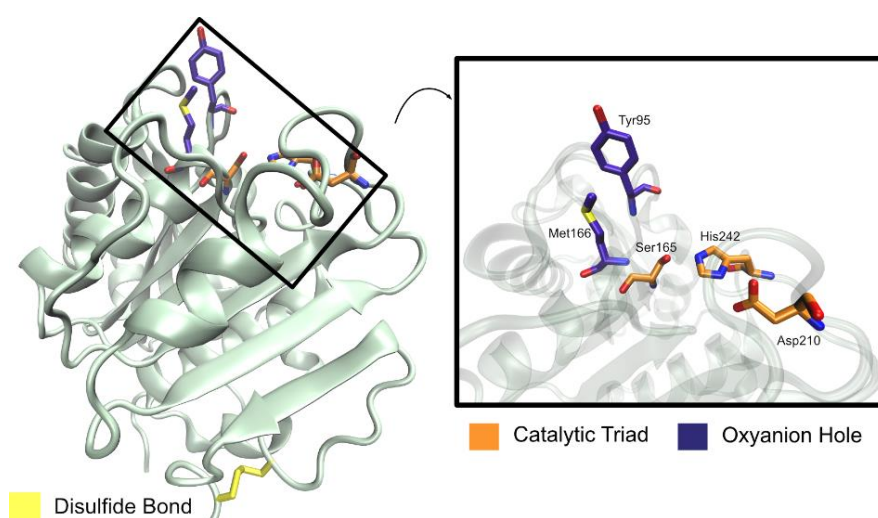


**Figure 14.** Representation of important amino acid residues of LCC: catalytic triad (in orange) the oxyanion hole (in blue) and the disulfide bonds (in yellow) represented in Licorice.

### 2.4.3. Activity

To determine the optimal hydrological pH and temperature of LCC Sulaiman et al. (60) measured its activity against *p*NP-butyrates. The enzyme showed highest activity at pH 8.0 and temperature of 50 °C. The addition of CaCl<sub>2</sub> and EDTA did not change the enzymatic activity. The determination of the substrate specificity was also studied, using *p*NP monoesters with different acyl chain lengths of 2 to 12 as substrates. LCC exhibited preference against *p*NP-butyrates (C4).

In the same study, the group studied the ability of LCC to degrade PET and PCL (60). After 24 hours of incubation, the enzyme degraded 1.45 mg of PET film, which resulted in a specific activity of 12 mg/h/mg enzyme at pH 8.0 and 50 °C. Regarding PCL degradability, the specific enzymatic activity was determined to be 300 mg/h/mg enzyme in the same conditions. The products resulted from the catalysis were TPA

as the major product and some residual MHET. BHET was not detected, meaning that the enzyme fully hydrolyzes PET to TPA and EG. Furthermore, LCC showed activity 230–970-fold higher than other cutinases with PET degradation ability.

Even though the highest activity of LCC occurs at 50 °C, the enzyme remains stable up to 75 °C (61). The same authors concluded that at temperatures above 50 °C the enzymatic activity decreases. To confirm this, kinetic parameters (turnover numbers ( $k_{cat}$ ) and binding affinity constants ( $K_M$ )) were determined at 30, 50 and 70 °C using as substrate *p*NP-butyrate.  $K_M$  values were similar (0.21–0.24 mM), meaning that temperature variation does not influence the binding affinity. However,  $k_{cat}$  values differ with change of temperature, peaking at 50 °C ( $232 \pm 20$ ,  $343 \pm 4$  and  $318 \pm 46$  s<sup>-1</sup> at 30, 50 and 70 °C, respectively). This means that the lowering in activity at 60 and 70 °C is due to the decrease in turnover rate. Nevertheless, activity assays towards PET film showed an increase of activity at 70 °C, much likely due to the PET crystallinity modifications at higher temperatures, which allows a better fitting of the long-chain substrate.

Ser165 was confirmed to be a catalytic triad residue by mutagenesis approach, where its variant to alanine (S165A) led to an almost total loss of activity (60,62). A variant disrupting the disulfide bridge (C275A–C292A) was produced, resulting in no structural changes however, the denaturation curves measurement showed a destabilization of approximately 15 °C than WT LCC, confirming the important role of the disulfide bond in enzymatic thermal stability (61).

LCC activity towards commercially available amorphous PET was compared with other PET hydrolyzing enzymes (*TH*Cut and BTA-2, *Fs*Cut and *Is*PETase) by Tournier et al. (62). At 65 °C the enzyme outperformed all tested enzymes, being 33-fold more efficient than any other tested enzyme. Moreover,  $T_m$  was determined to be 84.7 °C, confirming its high thermal stability. To increase the enzymatic activity and stability the authors performed molecular docking and molecular dynamics calculations to predict the binding mode 2-HE(MHET)<sub>3</sub>. The predicted binding site inspired 11 site-specific mutations and the production of 209 variants. F243I, F243W, T96M, Y127G, N246D, and N246M showed similar increased activity, however the latter four variants also improve the thermostability. An additional disulfide bond (D238C–S283C) was constructed to increase the thermal stability, resulting in an enhancement of 9.8 °C ( $T_m = 94.5$  °C) and in an activity loss of 28%. Two variants were combined with the disulfide bond (F243I/D238C–S283C, named ICC and F243W/D238C–S283C, named WCC), resulting in similar activity to WT LCC with higher melting temperature values. Other, previously described variants (T96M, Y127G, N246D, and N246M) were combined with ICC and WCC. Of which, four variants (ICCG, ICCM,

WCCG, and WCCM) showed similar or slightly higher activity and improved  $T_m$  up to 13.4 °C when compared to WT LCC (62).

A thermophilic whole-cell biocatalyst with high LCC expression was developed by Yan et al. (63) to efficiently degrade PET film. *Clostridium thermocellum*, a thermophilic anaerobe bacterium that grows at an optimal temperature of 60 °C) was used to build a whole-cell biocatalysts with high LCC secretory expression at high temperatures. The system revealed an over 60% weight loss of an amorphous PET sample in a 14-day incubation period, resulting in higher degradation rate than previous whole-cell PET hydrolyzing systems reported.

## 2.5. *Thermomonospora fusca* Hydrolase (*TfH*Cut) and *Thermomonospora fusca* BTA Hydrolase 2 (BTA-2)

### 2.5.1. Discovery

*TfH*Cut, also known as *Thermomonospora fusca* hydrolase, TfH, BTA-hydrolase 1 (BTA-1) (64) or Tf<sub>u</sub>\_0883 (65) is a PET degrading cutinase-like enzyme. The thermophilic filamentous soil bacterium ability to degrade polyester-like substrates was first uncovered by Kleeberg et al. (64) in 1998. The enzyme ability to degrade BTA earned the name BTA-1 (66). Another enzyme expressed by the same organism also showed ability to degrade BTA and PET and was named BTA Hydrolase-2 (BTA-2). Both enzymes share a 92% amino acid sequence identity, and the gene that expresses them are similar (66).

The different terms for the *TfH*Cut are due to the uncertainty in its classification as a lipase or cutinase. Even though Chen et al. (65) identified cutinase-like activity (renaming the enzyme as Tf<sub>u</sub>\_0883), the previous designations are still used. *TfH*Cut has been identified, purified, expressed, and characterized as a thermophilic hydrolase with aliphatic-aromatic copolyesters degrading ability. The enzyme showed specific PET degrading ability in a study by Müller et al. (67), using two different PET samples.

### 2.5.2. Structure

The enzyme is constituted by 261 amino acid residues and revealed a total molecular weight of 28 kDa (68). Like other PET hydrolases, the catalytic triad is comprised by serine, histidine, and aspartate residues (Ser170, His248 and Asp216) (65). The catalytic Ser is located in a nucleophilic elbow and found in a G-H-S-M-G conserved motif (68). Chen et al. (65) built a homology model based on S<sub>e</sub>Lip, a lipase from *S. exfoliates*, and determined that the enzyme adopts the typical  $\alpha/\beta$ -hydrolase fold that is comprised by a central  $\beta$ -sheet with  $\alpha$ -helices on both sides. Moreover, the study revealed that the oxyanion hole is composed of Met171 and Tyr100. Silva et al. (69) later confirmed these findings with a

homology model with a similar protocol. Kleeber et al. (68) revealed that the binding site is exposed and not buried, which facilitates the attack to the ester bonds to be cleaved. These findings were also confirmed by Silva et al. (69).

Up until now only one three-dimensional structure of *THCut* is available and was determined by Dong et al. (70) (PDB: 5ZOA) with a resolution of 1.54 Å. The structure contains all the 261 amino acid residues and indicates that the enzyme is a functional monomer. Furthermore, it confirmed the predicted catalytic triad and oxyanion hole amino acids. The comparison of similar PET hydrolyzing cutinases revealed that a possible disulfide bond is present (Cys281–Cys299). Since the authors were unable to determine the crystallographic structure of the enzyme complexed with BHET and other cutin mimics, they decided to employ molecular docking and molecular dynamics calculations to analyze the active site and binding mode. Molecular docking with an oligo-polyester mimic cutin (C<sub>24</sub>H<sub>42</sub>O<sub>8</sub>, CAS number 10061-30-0) showed that the substrate is partly inserted in a hydrophobic shallow groove and the remaining is exposed to the bulk solvent environment. Moreover, the ligand forms hydrogen bonds with the oxyanion hole residues and a cleavable ester bond is in an optimal distance to be attacked (70).

### 2.5.3. Activity

Kleeberg et al. (68) revealed that *THCut* has a maximum activity at 65 °C and pH 6.0 to 6.5, that quickly decreases at 70 °C. Furthermore, the enzyme showed preference for shorter chain polymers.

Müller et al. (67) used two different PET samples (commercial PET and pellet PET-B) and analyzed the hydrolytic activity of *THCut*. These PET samples showed low crystallinity, which facilitate the enzymatic binding and activity rates. The activity assay was conducted at 55 °C over a 3 week-incubation period, and resulted in a similar degradation rate for both PET samples (8–17 μm·week<sup>-1</sup> per film).

Silva et al. (69) produced two engineered variants to enlarge the active site (I218A) and to enhance hydrophobicity (Q132A/T101A). These variants resulted in a two-fold activity increase when compared to WT *THCut* when a PET fabric was used at 60°C. These improvements may be due to the enlargement of the active site binding space and enforced hydrophobic character. Other catalytic assays revealed that mutant Q132A/T101A is the better-performing variant.

Then et al. (71) tested the activity of *THCut* and BTA-2 in the presence of Ca<sup>2+</sup> and Mg<sup>2+</sup> ions, using PET film as substrate at 50 °C and pH 8.0 for 48 h in a shaker at 125 rpm. The study determined that the effect of the cations is temperature-dependent, with the enzyme being active at 65 °C only in the presence of these cations. Furthermore, the enzyme resulted in a 4.5-fold activity enhancement at 65 °C in the



presence of  $\text{Ca}^{2+}$  and  $\text{Mg}^{2+}$  when compared to the WT *7HCut* at 60 °C. Molecular dynamics simulations concluded that via the carboxyl groups  $\text{Ca}^{2+}$  is likely to bind Asp174 and Asp204 residues and via the amide hydrogen the Gly205, while  $\text{Mg}^{2+}$  probably binds to five residues (Glu253, Asp174, Asp246, Glu26, and Thr41).

Alisch-Mark et al. (72) determined that *7HCut* has the ability to modify PET fibres surface, which is an essential ability for biodegradation in the textile industry. Furthermore, mutation on the catalytic serine (Ser170) resulted in total loss of activity, which confirms the predicted catalytic activity (65).

Su et al. (73) determined that *7HCut* is an extracellular acting enzyme, while studying its activity against phospholipids. Other engineering efforts studies in other substrates showed increased binding site flexibility and better substrate accommodation. Studies to achieve optimal quantity and purity levels have been achieved, which may be important for future engineering studies (66,74,75).

#### 2.5.4. Proposed mechanism

Inspired by its predicted homology model, Chen et al. (65) suggested the typical catalytic mechanism of  $\alpha/\beta$ -hydrolases, performed by the catalytic triad (Ser170, His248, Asp216), where the substrate is stabilized by the oxyanion hole residues (Met171 and Tyr100). The process involves the formation of two tetrahedral transition states and an acyl-enzyme intermediate.

### 2.6. *Saccharomonospora viridis* AHK190 Cutinase (*SiCut190*)

#### 2.6.1. Discovery

*Saccharomonospora viridis* AHK190 Cutinase (*SiCut190*), commonly known as Cut190 was first identified and determined to have ability to degrade PET by Kawai et al. (76) in 2014. The thermophilic bacterium grows at optimal temperatures of 55 °C (77). However, the enzyme is only active in the presence of  $\text{Ca}^{2+}$  ions.

#### 2.6.2. Structure

The enzyme exists as a functional monomer and contains 304 amino acid residues. It adopts the common  $\alpha/\beta$ -hydrolase fold, which is made up of a central twisted  $\beta$ -sheet of nine  $\beta$ -strands and six  $\alpha$ -helices. Short helices  $\alpha 1$ ,  $\alpha 4$ ,  $\eta 1$ , and  $\eta 2$  have also been identified however, no lid domain surrounding the active site was identified. The catalytic triad is comprised by Ser176, His254, and Asp222 and are located on the loops  $\beta 5$ - $\alpha 5$ ,  $\beta 7$ - $\alpha 6$ , and  $\beta 8$ - $\alpha 7$ , respectively (78) and the oxyanion hole is defined by Phe106 and Met177. Moreover, a disulfide bond (Cys287-Cys302) connecting the terminal loop to  $\alpha 8$ - $\beta 9$  loop and three  $\text{Ca}^{2+}$  binding sites located on the  $\beta 1$ - $\beta 2$ ,  $\beta 7$ - $\beta 9$  and  $\beta 6$ - $\beta 7$  loops were also determined (79).

The enzyme undergoes large conformational changes after the binding of  $\text{Ca}^{2+}$  ions, which allows the pocket to open, allowing an easier access for substrate binding (79). All the amino acid residues involved in the three  $\text{Ca}^{2+}$  binding site (named site 1 to 3) were determined by Oda et al. (80). Site 1 is located in the  $\beta 1$ – $\beta 2$  loop and is composed of Ser76, Ala78, and Phe81. This site is reported to have an important role on enzymatic activity. Site 2 is located in the  $\beta 7$ – $\beta 9$  loops and is comprised by Glu220, Asp250, and Glu296. The site is involved in the enzymatic thermostability. Lastly, the Site 3 is found in the  $\beta 6$ – $\beta 7$  loop and is encompassed by Asp204 and Thr206. The site is involved in both enzymatic activity and thermostability.

Currently, no structures of the WT enzyme are available. The first three-dimensional structures were determined by Miyakawa et al. (78) with a mutation in position Ser226 (S226P). The structures are in the apo-form with  $\text{Ca}^{2+}$  present (PDB: 4WFJ and 4WFK with resolutions of 1.75 and 2.35 Å, respectively) and without  $\text{Ca}^{2+}$  (PDB: 4WFI with resolution of 1.45 Å). Later, an inactive form (S176A/S226P/R228S) was determined and complexed with Et-succinate (PDB: 5ZRR with resolution of 1.34 Å) and Et-adipate (PDB: 5ZRS with resolution of 1.40 Å) (79). Analysis on these structures revealed that conformational changes occur on  $\beta 3$ – $\alpha 2$  and  $\beta 4$ – $\alpha 3$  loops and is referred to as the engaged form. Furthermore, the residue Trp107 that forms a hydrogen bond with Arg135 in the apo-form, undergoes induced-fit conformational changes and becomes linked to the ligand ester group.

Other structures with further mutations are also available in the Protein Data Bank.

### 2.6.3. Activity

Ser176 role as a catalytic triad amino acid residue was confirmed when its replacement with alanine (S176A) resulted in a total loss of activity (79).

WT *S*Cut190 showed a  $T_m$  value of 55.4 °C (76). Currently many engineering efforts have been performed to improve the enzymatic activity and thermostability of the enzyme. Inspired by the similarity of *S*Cut190 with *Ta*Est119, the group mutated Ser226 (corresponding to Pro219 in *Ta*Est119) with a proline, which resulted in a  $T_m$  improvement of 3.7 °C (59.1 °C) and an enhancement of enzymatic activity against *p*-nitrophenyl butyrate (76). The positively charged Arg228 was thought to form a salt bridge with a residue with negative charge, which may hinder the reaction. Therefore, Kawai et al. (76) replaced it with serine (R228S) and combined it with the previous variant (S226P/R228S), resulting in an enhancement of thermostability (76.8 °C) in the presence of 300 mM of  $\text{Ca}^{2+}$ . Furthermore, to improve the salt-bridge formation, the group combined T262K to the previous double-mutant (S226P/R228S/T262K), which resulted in an enzymatic activity increase with a slightly decrease in  $T_m$ .

(76.2 °C) in the same conditions. Kawabata et al. (81) developed a three-dimensional model based on the first crystallographic reported structure to analyse several mutations on residues surrounding the catalytic triad, oxyanion hole and Ca<sup>2+</sup> binding site. The double mutant variant (S226P/R228S) resulted in a  $k_{cat}$  of  $27 \pm 0.2 \text{ s}^{-1}$  and  $K_M$  of  $0.089 \pm 0.001 \text{ mM}$  using PBSA as substrate. Overall, the mutations on residues neighbouring the oxyanion hole to an alanine resulted in a decrease of  $k_{cat}$ , apart from Q138D, which increased  $k_{cat}$  to  $61 \pm 0.3 \text{ s}^{-1}$  (81). The combination of (S226P/R228S) with the deletion of the C-terminal residues (Lys305/Leu306/Asn307) further increased  $k_{cat}$  to  $100 \text{ s}^{-1}$  (82).

Oda et al. (80) used the same three-dimensional model to apply mutagenesis in the residues involved in the Ca<sup>2+</sup> binding site, using PBSA as substrate. *Sl*Cut190 lacks some amino acids in the  $\beta$ 1– $\beta$ 2 loop (Site 1) when compared to other cutinases. Thus, the authors introduced a serine between Phe77 and Ala78 (78Ser) that showed enhancement of the enzymatic activity ( $k_{cat} = 151 \text{ s}^{-1}$ ). Unfortunately, its expression was exceptionally low. A disulfide bond (D250C–E296C) was produced in Site 2 and significantly increased  $T_m$  value to 79 °C. In Site 3, the best performing mutant was N202H. Finally, Oda et al. (80) built the most thermostable variant to date ( $T_m = 85.7 \text{ °C}$ ), by combining the best single variants (*Sl*Cut190S226P/R228S/Q138A/D250C–E296C/Q123H/N202H).

Kawai et al. (76) performed studies regarding PET hydrolysis, using PET-GF and PET-S as substrates. The degradation rate of *Sl*Cut190S226P/R228S was about  $10.9 \pm 1.5\%$  and  $26.2 \pm 0.6\%$  for PET-GF and PET-S, respectively at 63 °C for 3 days. TPA was the major released product, with no detection of BHET, which means that the variant fully hydrolyzes PET films. In a later work, Oda et al. (80) studied the degradation rate products of PET-GF with 6.3% crystallinity by the double mutant and other variants that resulted in higher thermostability. *Sl*Cut190S226P/R228S revealed a degradation rate of  $16.0 \pm 1.4\%$  at 65 °C for 3 days. Expectedly, the best thermostable variant showed the highest degradation rate ( $33.6 \pm 3.0\%$ ) at 70 °C for 3 days. The variant resulted in a 30% activity increase when compared to WT *Sl*Cut190 at 63 °C for 3 days.

#### 2.6.4. Proposed Mechanism

Based on its molecular docking models, Kawabata et al. (81) proposed a catalytic mechanism with the variant S226P/S228R. The mechanism starts with the deprotonation of Ser176 by His254, which becomes active for nucleophilic attack, and attacks the carbonyl group of the substrate, resulting in the formation of an acyl-enzyme intermediate. The intermediate is later subjected to nucleophilic attack by a water molecular that is deprotonated by His254 with the resulting proton being transferred to Ser225, regenerating the catalytic triad for a new catalytic cycle.

## 2.7. *Thermobifida* Genus Cutinase 1 and Cutinase 2 (Cut1 and Cut2)

### 2.7.1. Discovery

*Thermobifida* genus produces many enzymes with PET degrading ability. This includes Cutinase 1 (Cut1) and cutinase 2 (Cut2), which are produced by *Thermobifida fusca*, *Thermobifida alba*, and *Thermobifida cellulosilytica*. *T. cellulosilytica* and *T. fusca* are both thermophilic bacteria that grow at temperatures up to 45 and 55 °C, respectively. Meanwhile, *T. alba* is less thermostable (mesophilic bacterium) and can only grow at temperatures up to 37 °C. Both Cut1 and Cut2 from these species are similar, differing in only up to 18 amino acid residues (83). Their ability to degrade PET was first reported by Herrero et al. (84) in 2011.

### 2.7.2. Structure

All enzymes consist of 262 amino acid residues, apart from Cut2 from *T. fusca*, which has one less amino acid.

Roth et al. (85) solved in 2013 the first three-dimensional structures of Cut2 from *Thermobifida fusca* KW3 (*Tc*Cut2). The structures include the enzyme in its free state (PDB: 4CG1 and 4CG3, with resolutions of 1.4 and 1.55 Å, respectively) and complexed with the inhibitor phenylmethylsulfonyl fluoride (PMSF) (PDB: 4CG2, with resolution of 1.44 Å). The enzyme was found to adopt the classical  $\alpha/\beta$ -hydrolase fold, which constitutes a central nine-stranded  $\beta$ -sheet encompassed by 11  $\alpha$ -helices on both sides. The catalytic triad is located in a superficial cleft and is made up by Ser130, His208, and Asp176, while oxyanion hole is composed of Met131 and Tyr60. The residues Ala55 to Ala65, Leu175 to Pro180 and His208 to Pro211 are believed to be part of the active site and showed high flexibility (85). Furthermore, a disulfide bond (Cys241–Cys259) is located surrounding another highly flexible region around the amino acid sequence Arg245–Gly247. This disulfide bond may explain the relative high  $T_m$  value of  $71.2 \pm 0.2$  °C (85).

Cut1 and Cut2 from *Thermobifida cellulosilytica* (*Tc*Cut1 and *Tc*Cut2, also referred to as *Thc*\_Cut1 and *Thc*\_Cut2, respectively) crystallographic structures were solved by Ribitsch et al. (86) in 2016 in their free state. Only one crystallographic was solved for *Tc*Cut1 (PDB: 5LUI, with resolution of 1.5 Å). Meanwhile, *Tc*Cut2 was solved in its WT form (PDB: 5LUJ, with resolution of 2.2 Å), double mutant (R29N/A30V) variant (PDB: 5LUK, with resolution of 1.45 Å) and triple mutant (R19S/R29N/A30V) variant (PDB: 5LUL, with resolution of 1.90 Å). Both cutinases are similar to the previously characterized *Tc*Cut2, apart from the number of  $\alpha$ -helices (11 vs. 10) found to be flanking the  $\beta$ -sheet.

No crystallographic structures were determined for *Thermobifida alba* Cut1 (*Ta*Cut1 also defined as *Tha*\_Cut1). However, the cutinase has high similarity to *Tc*Cut1, only differing in 4 amino acids that are located outside the active site (83).

### 2.7.3. Activity

*Tc*Cut1 and *Tc*Cut1 (DSM44342) were identified to fully catalyze PET, with the major product release being TPA (84). However, an inhibitory effect by BHET has been reported (87). Furthermore, *Tc*Cut1 activity was faster while using semi-crystalline PET film (24% crystallinity) as substrate when compared to amorphous PET film (12% crystallinity) (87). Meanwhile, *Tc*Cut2 revealed a limiting rate on the hydrolysis of MHET to TPA, resulting in MHET as the major product release (84).

*Tc*Cut2 also revealed to be unable to hydrolyze MHET efficiently to TPA (88–90). Barth et al. (88) measured the kinetic parameters of MHET and BHET substrate by the protein, which resulted in very low  $k_{cat}$  and  $K_M$  values against MHET ( $0.31 \pm 0.01 \text{ s}^{-1}$  and  $7.33 \times 10^{-3} \pm 3.62 \times 10^{-4} \text{ mol L}^{-1}$ , respectively). As for BHET substrate, the same inhibitory effect was also observed, resulting a  $k_{cat}$  and  $K_M$  of  $26.76 \pm 0.85 \text{ s}^{-1}$  and  $3.97 \times 10^{-2} \pm 2.50 \times 10^{-3} \text{ mol L}^{-1}$ , respectively.

Wei et al. (89) while studying the *Tc*Cut2 complexed with a dimer PET model (2PET) observed that the residues Gly62, Thr63, Ile178, and Ile213 become in close vicinity to the substrate. The authors, inspired by this movements applied mutagenesis in the involved amino acid residues. The replacement of Gly62 with an alanine (G62A) resulted in the best performing mutation, with a weight loss of PET amorphous film of  $42.6 \pm 2.9\%$ , while the WT *Tc*Cut2 resulted in a weight loss of only  $15.9 \pm 1.8\%$ . Furthermore, the variant I213S revealed to be the highest thermal stable variant.

Then et al. (71) confirmed the involvement of residues Asp174, Asp204, and Glu253 in the  $\text{Ca}^{2+}$  binding site of *Tc*Cut2 by replacing the residues with arginine. The variants D204A and E253A revealed significantly increased of the  $T_m$  values ( $85.2 \pm 0.5 \text{ }^\circ\text{C}$  and  $86.2 \pm 0.8 \text{ }^\circ\text{C}$ , respectively) when compared to WT *Tc*Cut2 ( $71.2 \pm 0.2 \text{ }^\circ\text{C}$ ). In a later study, Then et al. (91) introduced a disulfide bond in the previous studied positions (D204C–E253C) that increased  $T_m$  to  $92.8 \pm 0.3 \text{ }^\circ\text{C}$ . The combinations of variants in the residue Asp174 (D174N and D174R) to the previous variant further increased the PET films weight loss, with D204C–E253C/D174N resulting in a weight loss of  $24.2 \pm 0.8\%$ , while D204C–E253C/D174R showed a weight loss of  $25.0 \pm 0.8\%$  when comparing to WT enzyme ( $16.3 \pm 2.2\%$ ).

Even though *Tc*Cut1 and *Tc*Cut2 differ in only 18 amino acids, their activity towards PET films are different, being *Tc*Cut1 much more effective than *Tc*Cut2. While comparing the two enzymes, Herrero et

al. (84) determined two regions with different electrostatic potential and hydrophobicity. The first region in *TcCut1* is defined by Ser19, Asn29, Val30, and Glu65, while in *TcCut2* the same region is comprised by the more positively charged residues Arg19, Arg29, Ala30, and Gln65. Meanwhile, the second region in *TcCut1* is made up of Ala183 and Lys187, whereas in *TcCut2* the involved residues are the hydrophobic residues Leu183 and Arg187 (Fig. 15). In a later study (92), engineering effort approach was applied in regions 1 and 2 of *TcCut2* to simulate the same regions from *TcCut1*. The double mutant R29N/A30V resulted in a four-fold activity increase against PET films, when compared to WT *TcCut2*.

Ribitsch et al. (83) studied the hydrolysis of *TaCut1* against the PET model bis(benzoyloxyethyl) terephthalate (3PET), which resulted in a release of MHET and 2-hydroxyethyl benzoate (HEB) as major products and marginal amounts of TPA and BA.

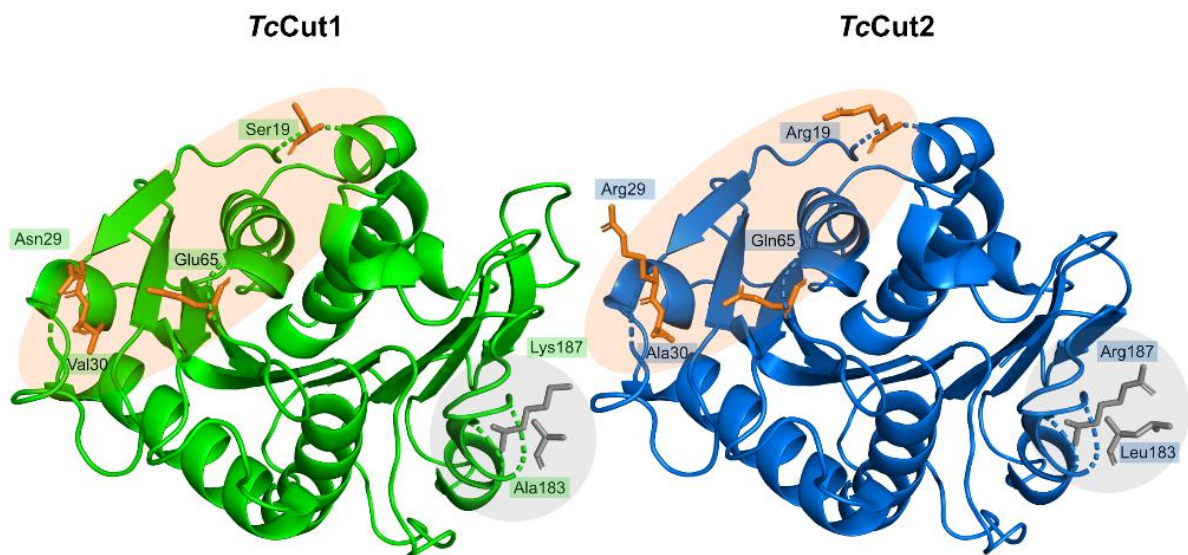


**Figure 15.** Comparison between two different regions in *TcCut1* (PDB: 5LUI), in green, and *TcCut2* (PDB: 5LUJ), in blue. Region 1 and region 2 are represented in orange and grey, respectively. Amino acid residues are identified by their three-letter code.

## 2.8. *Fusarium oxysporum* Cutinase 5 (*FoCut5a*)

### 2.8.1 Discovery

*FoCut5a* is a cutinase first expressed and characterized in 2015 by Dimarogona et al. (93). The organism that produced the enzyme is called *Fusarium oxysporum*, which is an ascomycete fungus and is commonly found in soil (94).

## 2.8.2. Structure

The enzyme is constituted by 230 amino acid residues, making the total molecular weight of 23 kDa (93). The structure analyses revealed that the enzyme adopts the  $\alpha/\beta$ -hydrolase fold, with a central  $\beta$ -sheet made up of 5 parallel  $\beta$ -strands and 11  $\alpha$ -helices. The catalytic triad is defined by Ser121, His189, and Asp176, which is located in the nucleophilic elbow, in close vicinity of strand  $\beta$ 5 and helix  $\alpha$ 5 loop (Fig. 16) (93,95). Reports about the oxyanion hole comprising residue are unavailable, however an analysis of its X-ray structure indicates Ser43 and Gln123 as possible residues involved in the oxyanion hole (Fig. 16).

Two disulfide bonds were identified to connect the loop  $\alpha$ 1- $\beta$ 1 to loop  $\alpha$ 4- $\beta$ 3 (Cys32-Cys110) and the loop  $\beta$ 5- $\alpha$ 8 to helix  $\alpha$ 8 (Cys172-Cys179), respectively. The later disulfide bond is also flanking the catalytic triad (93,95). The interactions between the polar Lys63 and Tyr64 with Asp209 is thought to increase the overall enzymatic thermostability. However, repulsive forces between Glu165 and Asp166 can influence negatively the thermostability (93) (Fig. 16).

Currently, only one three-dimensional structure was solved for *Fo*Cut5a in its free state (PDB: 5AJH, with a resolution of 1.9 Å) by Dimarogona et al. (93) in 2015.

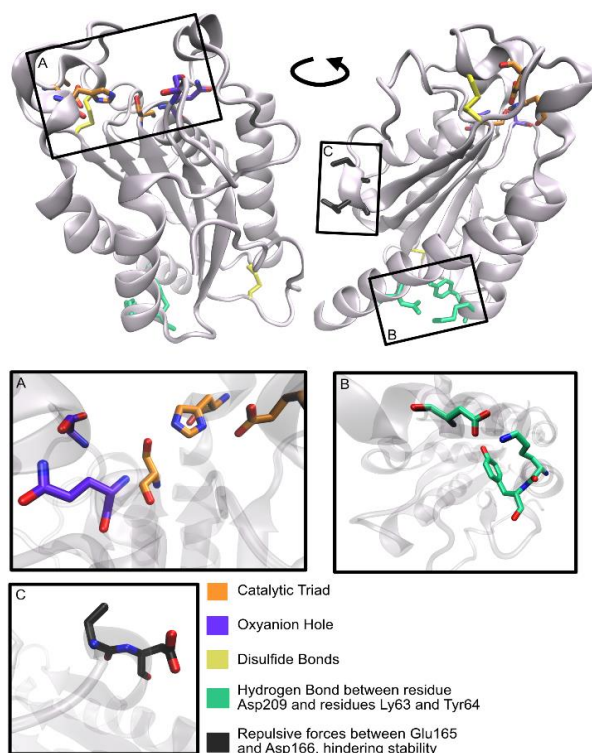


**Figure 16.** Schematic representation of main structural aspects of *Fo*Cut5a. **(A)** Detailed view of the catalytic triad and oxyanion hole residues. **(B)** Schematic representation of the hydrogen bond between residues Lys63 and Asp209 **(C)** View of the two repulsing amino acid residues Glu165 and Asp166.

### 2.8.3. Activity

The optimal parameters for the enzyme were determined to be 40 °C, pH 8.0 and 1.92 mg enzyme loading per gram of PET substrate (93,95,96). Nikolaivits et al. (95) showed that the selection of the expression host can influence the formation of disulfide bond, thus thermostability, by expressing the host in two different organisms. The highest performing  $T_m$  ( $44.9 \pm 0.5$  °C) was obtained in the oxidative cytoplasm of Origami 2 competent cells.

Dimarogona et al. (93) confirmed that the cutinase is able to degrade PET when incubation of *FcCut5a* with 3PET resulted in a product release of TPA, BHET and BA (0.19, 0.20 and 1.09 mM, respectively). The enzyme also further hydrolyzes BHET to MHET, which resulted in a 46% abundance of MHET. Furthermore, when using PET fabrics, the enzyme successfully released 26  $\mu$ M of TPA and derivatives. Currently, no engineering efforts studies are report.

## 2.9. *Humicola insolens* Cutinase (*HCut*)

### 2.9.1. Discovery

*HCut*, also referred to as HiC is a well-known enzyme, with its first findings reported in 1964. *Humicola insolens* is a thermophilic fungus with the ability to grow at temperatures up to 58 °C (97). The first association of this cutinase with PET degradation ability was reported by Ronkvist et al. (98) in 2009.

### 2.9.2. Structure

*HCut* is composed of 194 amino acids, resulting in a total molecular weight of 32 kDa. The structure analyses of the cutinase showed a typical  $\alpha/\beta$ -hydrolase fold with a central five-stranded  $\beta$ -sheet, containing six  $\alpha$ -helices on both sides. The conserved catalytic triad is defined by Ser130, His173, and Asp160 (99). References regarding the oxyanion hole comprising residues are unavailable, however upon analysis of the X-ray structure, residues Ser28 and Gln106 are likely to be the ones involved. Three amino acid residues (Leu66, Leu167, and Ile169) located in the hydrophobic loops adjacent to the active site are thought to restrain the entrance of larger substances (100).

*HCut* also exhibited a presence of two disulfide bonds (Cys17–Cys94 and Cys156–Cys163), according to UniProtKB (101). Only two three-dimensional structures of *HCut* are currently available. Kold et al. (99) determined the structures in its free form (PDB: 4OYY, with a resolution of 3 Å) and complexed with mono-ethyl phosphate (PDB: 4OYL, with a resolution of 2.05 Å).



### 2.9.3. Activity

The cutinase showed maximum initial activity at 80 °C and pH 8.5. However, it becomes totally inactive at 90 °C presumably because of enzymatic denaturation (98). Studies on the substrate specificity revealed that *HCut* has a preference towards long-chain alcohols and acids (102,103).

Ronkvist et al. (98) reported that *HCut* was able to fully catalyze amorphous PET (7% crystallinity) to TPA at 70 °C resulting in a surprising  $97 \pm 3\%$  weight loss in 96 h. However, Castro et al. (104) and Carniel et al. (105) while using PET and BHET as substrate revealed that the enzyme has a limiting rate on the MHET hydrolysis to TPA. Therefore, a system involving *HCut* and an enzyme that can properly hydrolyze MHET to the building block was implemented by Carniel et al. (105). The selected enzyme was *CaLipB* and the double enzymatic system resulted in a 7.7-fold enhancement of TPA concentration. While using PET films with different crystallinity (7 and 35%), Ronkvist et al. (98) determined an activity decrease by 10-fold when the enzyme was exposed to PET film with 35% crystallinity compared to the amorphous PET.

Quartinello et al. (106) developed an interesting two-step system, where first occurs the depolymerization of the virgin PET fibre at 250 °C and 39 bar. This process results in a powder that is consisted of 85% TPA and small PET oligomers. To further hydrolyze these oligomers, *HCut* was used, resulting in a total of 97% TPA production.

Carniel et al. (107) determined that the hydrolysis reaction of post-consumer PET is 2.39-fold higher in an unbuffered reaction (alkaline water – pH 8.5) when compared to Tris-HCl-buffered (pH 8.5) at 50 °C. Meanwhile, Eugenio et al. (108) uncovered that 1.68 mgprotein mL<sup>-1</sup> is the best fitting enzymatic concentration for optimal reaction.

## 2.10. *Fusarium solani* Cutinase (*FsCut*)

### 2.10.1. Discovery

*FsCut* or *FsC* was first characterized by Lin et al. (109) in 1980. The fungus is a known spread soil pathogen (110,111) and several biochemical and structural studies are currently available.

### 2.10.2. Structure

*FsCut* is defined by 230 amino acid residues with a total molecular weight of 23 kDa. The enzyme exists as a functional monomer and structural studies revealed a typical  $\alpha/\beta$ -serine fold with a central  $\beta$ -sheet comprised by five parallel  $\beta$ -strands and five  $\alpha$ -helices on either side (110,112,113). The catalytic triad

is defined by the residues Ser136, His204, and Asp191 (110), while the oxyanion hole is comprised by Gln137 and Ser58 (112).

The spacious binding site was determined to be mostly hydrophobic, being partly covered by two “bridges”, which are formed by Leu97, Val200, Leu198, and Asn100 (110,112,113). A conserved water molecule is located in the catalytic site and is bounded to Leu192, Ala201, Ile199, and catalytic residue Asp191 and was determined to have a role in properly orienting sidechains, facilitating the catalysis (112). A higher B factor in the binding site amino acids was observed, suggesting conformational changes upon binding (110). Currently there are 46 three-dimensional structures of *FsCut* available on PDB.

### 2.10.3. Activity

Heumann et al. (114) determined activity of *FsCut* towards BHET and the ability to modify the PET fabric surface with positive yields.

Several points aiming to enlarge the binding site, thus the enzymatic activity, towards PET were developed by Araújo et al. (115). Through molecular dynamics and free energy calculations and using a substrate that mimics the tetrahedral intermediate (TI), five single mutations (L198A, V200A, L205A, L97A, and N100A) were predicted to favorably increase the stability of the TI model and enzymatic activity. However, when testing these variants with PET fabric as substrate at temperature of 37 °C, pH 7.0 for 48 h, only L198A, L97A, and V200A resulted in an enhanced activity. Following studies revealed that the best fitting variants showed a less restrained active site, which allows a better accommodation of TI, without affecting the hydrophobicity.

The effect of PET crystallinity (7 and 35%) on enzymatic activity of *FsCut*, *HCut* and *PmCut* was studied by Ronkvist et al. (98). Of these three enzymes, *FsCut* showed the worst affinity for PET and the lowest thermostability, showing a maximum activity at 50 °C. As the PET crystallinity increases the *FsCut* activity decreases.

## 2.11. *Candida antarctica* Lipase B (*CaLipB*)

### 2.11.1. Discovery

*CaLipB* also known as CalB or lipase B from *Candida antarctica*, is a well-known organism, being the target of many studies that was first isolated in 1988 (116,117). Several roles have been attributed to the enzyme, including desymmetrization of diacetates and diols, pharmaceutical production, synthesis of substrate intermediates, resolution of amines (118) and alcohols (119). These extensive number of

applications are due to the high thermal stability and enantioselectivity, low substrate specificity, and stability in diverse solvents properties (120).

### 2.11.2. Structure

*CaLipB* is composed of 317, has a total molecular weight of 33 kDa and exists as a functional monomer. The optimal pH for maximum catalytic activity was measured at 7 and the enzyme remains stable at 3.5 to 9.5 pH (121). The lipase adopts the  $\alpha/\beta$ -hydrolase fold with the catalytic triad being defined by Ser130, His249, and Asp212 while the oxyanion hole contains the residues Thr65 and Gln131 (119,122).

The catalytic triad is found in a carboxy-terminal hedge of the main parallel  $\beta$ -sheet, where Ser130 is located between the  $\alpha 4$ - $\beta 4$  loop, which has a tight turn and His249 is found in the  $\alpha 9$  and is in an optimal distance from Asp212. Furthermore, the catalytic serine forms hydrogen bonds with the polar residues Thr65, Asp159 and Gln182 (122). Moreover, Stauch et al. (121) determined the presence of a water molecule, which is shared between the catalytic His249 and Ser130. On the other hand, Strzelczyk et al. (118) determined the presence of a water molecule bonded to catalytic Asp212 and nearby Ser252.

The first three-dimensional structure of *CaLipB* was solved by Uppenberg et al. (119) that revealed the presence of 3 disulfide bonds (Cys47–Cys89, Cys241–Cys283, and Cys318–Cys336), contributing to the overall protein fold and stabilization of the enzymatic C-terminal. The existence of a lid domain with double conformation (open and closed) was predicted, however only later Stauch et al. (121) was able to confirm both conformations when a two-monomer structure representing the conformations was solved (PDB: 5A71 with a resolution of 0.91 Å). Monomer A represents the classical open confirmation, while monomer B showed a huge conformational change (closed conformation). The conformational change occurs in the helix  $\alpha 5$  (Leu165 to Leu172) that becomes unfolded in the monomer B, hindering substrate accessibility and preventing catalytic activity.

Up until now, 25 *CaLipB* three-dimensional structures were solved and are available in the Protein Data Bank.

Regarding the binding mode, many studies with different complexes were developed. Uppenberg et al. (119,122) determined the structure of *CaLipB* complexed with Tween 80 (PDB: 1LBT with resolution of 2.50 Å) and with a phosphonate inhibitor (PDB: 1LBS, with resolution of 2.60 Å). The former resulted in an unchanged overall enzymatic fold while the latter disrupted the optimal distances for catalysis. In order to understand the stereoselectivity of *CaLipB*, Xu et al. (123) determined a complexed structure with a synthesized stereoisomer product (PDB: 6J1T, with resolution of 1.78 Å).

### 2.11.3. Activity

Carniel et al. (105) determined that *CaLipB* can efficiently degrade BHET and MHET to TPA and EG. Furthermore, while used synergistically with *HCut* the system showed higher activity and affinity towards PET (Fig. 17). However, after 3 weeks of activity on both PET bottle and pellet, the lipase only showed a maximum of 0.4% weight loss, with MHET and BHET being almost totally degraded to TPA. Thus, the enzyme reveals a limiting rate in the hydrolysis of PET into the intermediates MHET or BHET. Although several studies are not specific to PET, they suggest valuable results and strategies, including engineering efforts that increase activity and higher stability of various substrates and circular permutation (124–130).

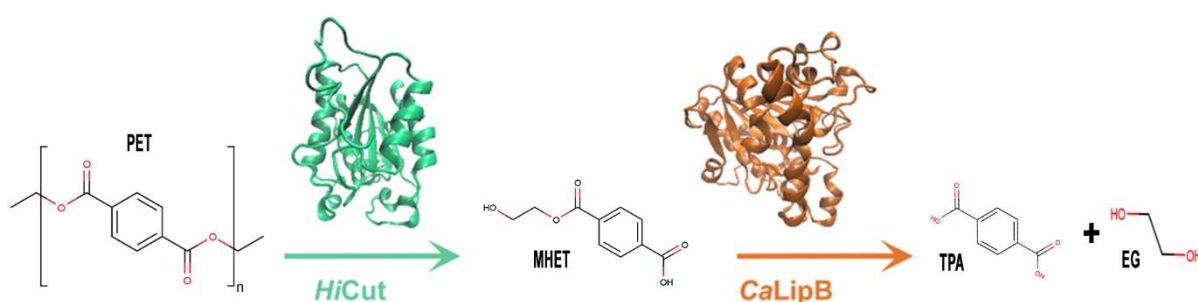


**Figure 17.** Dual-system action of *HCut* and *CaLipB* to fully degrade PET to TPA and EG.

## 2.12. *Thermomyces lanuginosus* Lipase (*TLip*)

### 2.12.1. Discovery

*Thermomyces lanuginosus*, previously known as *Humicola lanuginosa*, lipase (*TLip*, also described as TIL) was first discovered by Tsiklinskaya et al. (131) in 1889. The organism is a basophilic fungus that has been studied for serial industrial areas (132–135), where PET hydrolysis is included, being first reported in 2008 by Brueckner et al. (136).

### 2.12.2. Structure

*TLip* is made up by 269 amino acid residues with a total molecular weight of 31 kDa. The lipase revealed a  $\alpha/\beta$ -hydrolase fold with a central  $\beta$ -sheet made up of eight predominantly parallel  $\beta$ -strands, and five  $\alpha$ -helices with the catalytic triad defined by Ser146, His258, and Asp201 while the oxyanion hole is composed of Ser83 and Leu 147 (137,138). The enzyme also presents three disulfide bonds (Cys22–Cys268, Cys36–Cys41, and Cys104–Cys107).

Holmquist et al. (139) suggested that the residue Glu87 is involved in the electrostatic stabilization of the open-lid (active) conformation while Trp89 has critical role in substrate interactions. These findings were later confirmed (140,141). The first crystallographic structure of *TLip* was first solved by Derewenda et al. (138) in its free state (PDB: 1TIB, with resolution of 1.84 Å).

### 2.12.3. Activity

Omar et al. (142) determined that the optimal activity conditions are pH 7.0 and temperature 45 °C. Furthermore, the enzyme was stable for 20 h at 60 °C and 1 h at 65 °C, becoming inactive at temperatures higher than 70 °C. A later study, confirmed these findings, revealing that the lipase has a  $T_m$  around 65 to 70 °C (142,143).

Peters et al. (144) replaced the catalytic serine with an alanine (S146A) and the enzyme revealed a completely loss of activity, confirming its essential role as a catalytic triad residue. Holmquist et al. (139) and Martinelle et al. (140) replaced the residues Glu87 with alanine (E87A) and Trp89 with either phenylalanine or glutamate (W89F or W89E) that resulted in a lower specificity against tributyrin when compared to WT enzyme, which indicates that these residues have important roles in substrate binding. The introduction of a disulfide bond (I186C–I255C) resulted in thermostability loss of 5 °C, suggesting a secondary structure destabilization (143).

Brueckner et al. (136) revealed that the enzyme is able to degrade both amorphous and semi-crystalline PET fibres, with 5 and 40% crystallinity, respectively. However, the amount of products released were much too lower when compared to *Thermobifida fusca* cutinase (136).

Using the PET model 3PET, Eberl et al. (145) determined that the enzyme is able to hydrolyze the PET model, while releasing TPA, BHET, MHET, and HEB. In the presence of Triton X-100, the lid-opening undergoes conformation changes, which lead to a 7-fold enhancement of products release. Furthermore, the incubation of *TLip* with BHET resulted in insignificant amounts of TPA.

## 2.13. *Thermobifida fusca* Carboxylesterase (*TCa*)

### 2.13.1. Discovery

*TCa* is produced by *Thermobifida fusca*, a well-known meso-thermophilic bacterium that produces several biocatalysts (66,88,146). The enzyme is a highly hydrophobic carboxylesterase with its ability to degrade PET firstly described by Oeser et al. (147) in 2010.

### 2.13.2. Structure

Little information about *TcCa* is known because its three-dimensional structure is yet to be reported. The enzyme exists as a functional monomer that is defined by 497 amino acids. The catalytic triad is made up of Ser185, His415, and Glu319, with the catalytic serine involved in a motif that contains Glu184 and Ala186 residues (148).

### 2.13.3. Activity

*TcCa* was reported to be able to degrade PET nanoparticles at 50 °C and cyclic PET trimers with optimal conditions of 60 °C and pH 6.0 (147,148). The latter resulted in products release of 1,2-ethylene-mono-terephthalate-mono(2-hydroxyethyl terephthalate (EMT) (95%), MHET (3%), and BHET (2%). Furthermore, the binding affinity ( $K_m$ ) for cyclic PET trimers was  $0.5 \pm 9\%$  mM. Later, Belisário-Ferrari et al. (149) studied the hydrolysis of the carboxylesterase with 2PET and BHET. The kinetic parameters for BHET hydrolysis ( $k_{cat} = 0.35 \text{ min}^{-1}$ ;  $K_m = 0.085 \text{ mL/mg}$ ) were much better when compared to those of 2PET ( $k_{cat} = 0.10 \text{ min}^{-1}$ ;  $K_m = 0.042 \text{ mL/mg}$ ), meaning that the enzyme has a preference for smaller esters. The enzyme revealed a thermostability between 30 and 50 °C (148).

A dual enzymatic system (similar to the previous *HcCut-CaLipB* system) was built by Barth et al. (150) involving LCC and *TcCa*, with the latter being employed for hydrolysis of MHET to TPA. When comparing the product release of *TcCut2* ( $4.44 \pm 0.57 \text{ mM}$ ) with the system, a 2.4-fold increase was observed ( $10.42 \pm 1.85 \text{ mM}$ ). The important roles of the motif sequence (Glu184, Ala186, and Glu319) were confirmed when in-site mutagenesis in these residues (E184Q, A186M, and E319D) revealed an activity loss up to 88%.

## 2.14. *Thermobifida alba* Esterase 1 (*TaEst1*)

*TaEst1* is comprised by 260 amino acid residues and is produced by *Thermobifida alba*, being identified in 2013 (151,152). Comparing the enzymatic activity of *TaEst1* with *TaEst119*, a similar enzyme from the same organism against *p*NPB revealed that the former has a two-fold increase activity. Furthermore, the enzyme showed the ability to hydrolyze a PET film surface and to fully depolymerize 3PET to TPA (151,152).

An attempt to determine the three-dimensional structure of *TaEst1* have been reported by Kitadokoro et al. (153), however the group was not able to produce it. A homology model of *TaEst1* inspired by *TaEst119* was built by Thumarat et al. (152), where the catalytic triad (Ser169, His247, and Asp215) and oxyanion

hole (Met170 and Tyr99) were identified. The esterase revealed a  $\alpha/\beta$ -serine hydrolase fold, with a central made up by nine-stranded parallel  $\beta$ -sheet, which are flanked on each side by eight  $\alpha$ -helices.

$T_m$  of *TaEst1* was found to be 61 °C by Kitadokoro et al. (153). Furthermore, the group studied the enzymatic activity against *p*NPB at pH 6.0 and 50 °C and observed that the presence of  $Ca^{2+}$  ions resulted in a  $T_m$  increase by 15 °C (76 °C). Moreover, inspired by a conserved valine residue in most cutinases in the position Ala68, the group developed the variant A68V, which resulted in an activity enhancement. Thumarat et al. (152) also engineered several enzymatic variants, also tested in *p*NPB substrate. The best performing variant (A68V/T253P) resulted in further increase of  $T_m$  (79 °C) and revealed to have the highest activity against 3PET, however in the assay with PET film it was only evidenced a hydrolyzation of ester bonds in the film surface with no weight-loss recorded.

## 2.15. Lesser-known Enzymes

Many other enzymes revealed the ability to degrade PET, however only a few studies have been made for each one. In this section these enzymes are described.

### 2.15.1. *Enterobacter* sp. HYI Esterase B (*EsEstB*)

*EsEstB* also referred to as *EstB*, is an esterase produced by *Enterobacter* sp. HYI and was first characterized in 2020 by Qiu et al. (154), which determined the enzymatic ability of degrading BHET to MHET and TPA. The enzyme adopts the typical  $\alpha/\beta$ -hydrolase fold and the catalytic triad is defined by Ser110, His190, and Asp158. Furthermore, the esterase revealed maximum activity at an optimal pH of 8.0 and temperature of 40 °C, resulting in an 80.8% degradation of BHET in 120 h.

### 2.15.2. HR29 Hydrolase (*BhrPETase*)

*BhrPETase* is a hydrolase produced from the thermophilic bacteria HR29, that reveals ability to fully degrade PET. Furthermore, the enzyme only differs in 16 amino acid residues from LCC (94% sequence identity). *BhrPETase* is defined by 275 amino acids and adopts the typical  $\alpha/\beta$ -hydrolase with a catalytic triad composed of Ser165, His242, and Asp210. A disulfide bond (Cys275–Cys292) is also present (155).

The hydrolase activity against PET powder revealed a depolymerization of the substrate resulting in TPA as major product and BHET and MHET as secondary products. Furthermore, the enzymatic thermostability is the highest reported so far, with a  $T_m$  of 110 °C, which increases in the presence of  $Ca^{2+}$  ions by 6.4 °C (155).

### 2.15.3. *Bacillus subtilis* Lipase (*BsEstB*)

*BsEstB* is a lipase produced by *Bacillus subtilis*, firstly isolated in 2000 by Eggert et al. (156) and later determined to have activity against PET by Ribitsch et al. (157). The enzyme adopts the  $\alpha/\beta$ -hydrolase fold, being the catalytic triad defined by Ser189, His399, and Glu310.

The lipase was able to fully degrade PET film, being the major product released TPA and benzoic acid (157).

### 2.15.4. *Streptomyces scabies* Sub1 (*ScSub1*)

*ScSub1*, also known as Sub1, is a cutinase-like enzyme produced by a gram-positive plant pathogen bacterium (*Streptomyces scabies*) (158). A predicted structure (158) was determined using ESYPred3D (159) and revealed a canonical  $\alpha/\beta$ -cutinase-like fold, comprised by five parallel strands central  $\beta$ -sheet encompassed by ten  $\alpha$ -helices. Furthermore, the catalytic triad is suggested to be defined by Ser114, His195, and Asp182, and the presence of two disulfide bonds (Cys31–Cys103 and Cys178–Cys185) were also determined.

The activity of *ScSub1* against PET commercially available granules, was assayed at pH 7.5 and 37 °C for 20 days, resulting in a constant TPA production during the assay time (158).

### 2.15.5. *Pseudomonas mendocina* Cutinase (*PmCut*)

*PmCut*, also referred to as PmC, is a cutinase produced by *Pseudomonas mendocina* and was first described with PET degrading ability by Yoon et al. (160) in 2002. Later, Ronkvist et al. (98) compared the activities of *PmCut* with *FsCut* and *HfCut* against two PET samples. *FsCut* showed the highest binding specificity for the low crystallinity PET, however resulted in only the second highest activity, with a weight loss of 5% at 50 °C for 96 h.

### 2.15.6. PET1–PET13

Danso et al. (161) identified 504 possible enzymes with PET hydrolytic activity, of which 13 were selected and named PET1 to PET13. Of these 13 enzymes, PET2, 5, 6, and 12 were tested against PET agar plates containing PET nanoparticles, with PET2 standing out, revealing PET degrading activity up to 90 °C, meaning that is one the most thermostable enzymes currently studied. Furthermore, other activity assay, where 100  $\mu$ g of enzyme was used to degrade 14 mg of amorphous PET, resulted in a production of 900  $\mu$ M of TPA after 24 h period incubation.



### 2.15.7. *Thermomonospora curvata* Cutinases 0390 and 1278 (*TcCut0390* and *TcCut1278*)

*TcCut0390* and *TcCut1278*, or *Tcur0390* and *Tcur1278*, respectively are two cutinases produced by the facultative aerobic thermophilic bacterium *Thermomonospora curvata*, which grows at optimal conditions pH 7.5 to 11 and temperature of 50°C. Both enzymes share an 82% sequence identity (162).

Molecular docking and molecular dynamics studies by Wei et al. (162) revealed that both enzymes adopt the canonical  $\alpha/\beta$ -hydrolase fold, where the catalytic triad are located in the surface of the proteins, in a solvent exposed substrate-binding groove and is defined by Ser130, His207, Asp176. Furthermore, *TcCut1278* showed higher thermostability than *TcCut0390*. The activity assays against PET nanoparticles revealed that both enzymes have PET degradation ability (162).

### 2.15.8. *Thermobifida halotolerans* Esterase (*ThEst*)

*ThEst*, also referred to as *Thh\_Est*, is an esterase produced by *Thermobifida halotolerans*. The esterase is defined by 262 amino acid residues and shows high similarity to *TaEst119*. A sequence analysis performed by Ribitsch et al. (163) predicts a structural  $\alpha/\beta$ -serine hydrolase fold, being Ser131 the catalytic triad serine. Its hydrolytic activity against 3PET at 50 °C, pH 7.0 for 2h resulted in the release of benzoic acid (BA) and 2-hydroxyethyl benzoate (HEB) as the major products, and residual MHET and TPA. Against PET film, the enzyme was able to release MHET and TPA, with no BHET detected.

## 3. Microorganisms with PET Degradation Activity

Often it is not possible to identify the enzyme involved in the PET degradation. However, some microorganisms have been reported to be responsible for PET depolymerization and will be described in this section.

*Penicillium citrinum* was identified by Liebminger et al. (164) to have PET degradation activity, which showed optimal conditions for enzymatic activity against 3PET and PET fabrics at pH 8.2 and 30 °C. Furthermore, the enzyme was able to alter the surface of PET fabric and degrade 3PET to MHET, BHET, TPA and BA.

*Yarrowia lipolytica* was shown by Costa et al. (165) to have PET degrading activity. While incubated with amorphous PET, the enzymatic activity resulted in the release of MHET as the main product and residual TPA.

A bacteria consortium containing *Bacillus* and *Pseudomonas* species was developed by Roberts et al. (166), which resulted in a more effective PET degradation and surface alteration.

#### 4. Potential PET hydrolases with activity to be confirmed

*A $\alpha$* Cut or AoC is an enzyme produced by *Aspergillus oryzae*, and has the ability to degrade PCL, with suggestions indicating a similar effect on PET (167,168). Currently two crystallographic structures are available (PDB: 3GBS and 3QPD) that reveal an  $\alpha/\beta$ -serine hydrolase fold, with a central  $\beta$ -sheet encompassed by  $\alpha$ -helices on either side. The catalytic triad is defined by Ser126, His194, and Asp181, while the oxyanion hole is comprised by Ser48 and Gln127. Moreover, three disulfide bonds (Cys63–Cys76, Cys37–Cys115, and Cys177–Cys184) are present and near the active site a long and deep groove is observed, which may be the reason why the enzyme showed a relatively high thermostability ( $T_m = 62$  °C) (168). Shirke et al. (167) enhanced the  $T_m$  value by 6 °C using rotational mutation design.

Almeida et al. (169) identified SM14est, an esterase produced by *Streptomyces* sp., which was able to degrade PCL, thus having a potential to be a PET hydrolase. A homology model developed by the group revealed the typical  $\alpha/\beta$ -serine hydrolase fold with nine  $\beta$ -sheets and seven  $\alpha$ -helices, being the catalytic triad defined by Ser156, His234, and Asp202 and no disulfide bond was predicted. Furthermore, the enzyme has a similar binding subsite I when compared to *Is*PETase.

An esterase produced by *Thermobifida fusca* (*TAXE*) was reported by Huang et al. (170) in 2010 to have high similarity to *T $\mathcal{H}$* Cut, therefore being potentially a PET hydrolase.

*TaEst*119 is an esterase produced by the mesophilic bacterium *Thermobifida alba* (171). The enzyme shares 95% identity and 98% similarity to the reported *TaEst*1 (151,152). The enzyme is defined by 300 amino acids with a molecular weight of 30 kDa. Presently, three three-dimensional structures are available reveal that the enzyme only exists as a functional monomer and adopts an  $\alpha/\beta$ -hydrolase fold with a central twisted  $\beta$ -sheet of nine  $\beta$ -strands, surrounded by nine  $\alpha$ -helices on both sides, being the catalytic triad made up of Ser169, His247, and Asp215 and oxyanion hole composed of Met170 and Tyr99. Thumarat et al. (172) performed molecular docking with PET, which showed a good fitting of docked PET unit in the catalytic site for catalysis to occur. In a later study, Thumarat et al. (152) suggested that the oxyanion hole is defined by Met166 and Tyr99. Furthermore, the enzyme also displays a disulfide bond (Cys280–Cys298). Activity assays revealed that the optimal conditions for maximum enzymatic activity are 45 to 55 °C and pH 6.0 (60).

## **B. Theoretical Background**

Experimental techniques can explain and reveal important information about biological systems, giving crucial clues about their catalytic mechanisms. However, they cannot fully characterize many aspects of a reaction at the atomic and molecular level, such as breaking and formation of chemical bonds, which are fundamental to understand catalyses. Therefore, computational and theoretical chemistry methods are utilized for a detailed view of the mechanism, providing a complete interpretation of the catalytic process. These methods are often used to study biological system aspects, such as structure, energy, reaction mechanisms, catalysis, etc.

Presently, four theoretical levels of theory are commonly used for enzymatic reaction mechanism, namely *ab initio*; Density-Functional Theory (DFT); semi-empirical; and Molecular Mechanics (MM). It is up to the user opinion and experience to select the most appropriate strategy and theoretical level for the enzyme and the reaction that are being studied because each theoretical level has a different direct impact on the accuracy of the calculations, the number of atoms that can be used and computational cost. Therefore, it is necessary to take into account a balance between accuracy and computational cost.

The *ab initio* and Density-Functional Theory (DFT) methods are the most accurate and reliable ones to describe a molecular system. The *ab initio* method uses approximations to the Schrödinger's equation through the use of wave functions where atomic orbitals are described for the calculation of molecular properties. Some *ab initio* methods are: Monte Carlo, Hartree-Fock (HF) and Post-Hartree-Fock (Post-HF). Meanwhile, DFT methods utilize a different approach that involves an electron density function, allowing a description of biological and chemical systems with high accuracy. In the general scientific opinion, this method is the most balanced one out of the four theoretical levels of theory.

Semi-empirical methods are based on HF formalisms, with several parameters and approximations that turn them less demanding but also significantly less accurate.

Lastly, Molecular Mechanics (MM) methods are the simplest ones and utilizes classical physics to predict interactions and movements. These methods do not include electrons explicitly in their description, being the smallest particle of the system the atom. Therefore, MM cannot be used for chemical reaction simulations and phenomena that involves electronic events, such as catalysis. However, there is the advantage of using these methods in systems with many atoms (up to tens of thousands) with reduced computational cost.

One notable example of developed computational methods is the Quantum Mechanical/Molecular Mechanic (QM/MM) hybrid method, which has been widely used for chemical and biological studies,

particularly after the attribution the Nobel Prize in Chemistry to their initial creators in 2013 (Martin Karplus, Michael Levitt and Arieh Warshel) (173). The development of hybrid methods emerged from the necessity to study larger systems, with a compromise between accuracy and computational cost.

For this work, the hybrid QM/MM method is applied in the system. Therefore, in the next section MM, QM and QM/MM methods will be described in more detail.

## 1. Molecular Mechanics

As previously described the smallest particle of the system is the atom and therefore these methods cannot be used for chemical reactions studies because it involves the formation and cleavage of bonds, which requires an electronic description. Moreover, the atoms are treated as charged spheres linked by springs representing bonds. However, MM methods can be used to explore the conformational spaces of a system, for example in molecular structure refinement, molecular dynamics (MD), Monte Carlo (MC) and ligand-docking simulations (174). All interactions (bonded and non-bonded) are calculated using simple mathematic approaches, such as Hooke's law for bonded interactions and Coulombic and Lennard-Jones potentials for electrostatic and van der Waals interactions, respectively (174).

### 1.1. Force Fields

Force fields are referred as the combination of mathematical formula and associated parameters obtained by experimental works or *ab initio* calculations that are utilized to describe the energy system as a function of its atomic coordinates (175). These MM force fields approximate the quantum mechanical energy surface with significant decrease of computational cost (176).

Several force fields have been developed namely, AMBER (Assisted Model Building with Energy Refinement), which is one of the most used software, where ff99SB, ff19SB, ff14SB and GAFF (General AMBER force field) are included; CHARMM (Chemistry at Harvard Macromolecular Mechanics) (177); OPLS (Optimized Potentials for Liquid Simulations) (178); Gromos (Groningen Molecular Simulation package) (179) and many others. In this work, AMBER ff14SB and GAFF force fields were used due to the fact of ff14SB showing highest accuracy when compared with previous version (namely, ff99SB and ff19SB) and improvements on secondary structure content.

Typically, force fields use a simple additive potential energy function called "Class I" to achieve the system total energy. This is accomplished by the addition of all terms for the bond interactions and all terms for the non-bonded interactions (**Equation 1**) (175).

$$V_{system} = V_{bonded} + V_{non-bonded}$$

**Equation 1.** Potential energy function (Class I).

### 1.1.1. Bonded interaction

The bonded interaction, as previously described, are calculated using the Hooke's law and it is divided in 3 groups: bond stretching, angle bending and dihedral (also known as torsional) terms (**Equation 2**).

$$V_{bonded} = \sum_{bond} V_{bond} + \sum_{angle} V_{angle} + \sum_{dihedral} V_{dihedral}$$

**Equation 2.** Bonded interactions energy function.

The bonding stretching is represented by a simple harmonic oscillator as a function of the bond length ( $r$ ) that controls the covalent bonds (**Equation 3**) (175,180).

$$V_{bond} = \frac{1}{2}k_b(r - r_0)^2$$

$k_b$  is the force constant;  $r$  is the bond length;  $r_0$  is the bond length at the equilibrium.

**Equation 3.** Potential energy function of bond stretching.

An equivalent harmonic oscillator approximation is also utilized for the angle bending potential energy as a function of the valence angle (**Equation 4**) (176).

$$V_{angle} = \frac{1}{2}k_a(\theta - \theta_0)^2$$

$k_a$  is the force constant;  $\theta$  is the bond length;  $\theta_0$  is the bond length at the equilibrium.

**Equation 4.** Potential energy function of angle-bending.

Only two parameters are needed for each of these potential energy calculations, the force constant ( $k_b$  and  $k_a$ , for bonding stretching and angle bending, respectively) and bond length ( $r_0$ ) and angle value ( $\theta_0$ ).

The dihedral angle (or torsion angle) terms are associated with rotation of the dihedral angles defined by four atoms. In other words, considering a quadruplet of atoms (A, B, C and D), bonded to each other (A bonded to B, B bonded to C and C bonded to D), the dihedral angle is given by the angle of the planes ABC and BCD. The potential energy associated with the dihedral angle term is calculated by **Equation 5** (176).

$$V_{dihedral} = \frac{1}{2}v_n(1 + \cos(n\omega + \gamma))$$

$v_n$  is the force constant;  $n$  is the multiplicity;  $\omega$  is the dihedral angle (0 to 360°);  $\gamma$  is the dihedral angle value for which the energy is minimum.

**Equation 5.** Potential energy function of dihedral angle.

### 1.1.2. Non-bonded interactions

Earlier in this work, we revealed that the non-bonded interactions are comprised by electrostatic and van der Waals interactions (**Equation 6**) (176).

$$V_{non-bonded} = V_{electrostatic} + V_{van\ der\ Waals}$$

**Equation 6.** Non-bonded energy function.

Electrostatic interactions result of charges or permanent dipoles. For its analytic calculation the Coulombic law is used where the atoms are considered as charged points separated by their interatomic distance (**Equation 7**) (176).

$$V_{electrostatic}(i,j) = \frac{q_i q_j}{4\pi\epsilon r_{i,j}}$$

$\epsilon$  is the dielectric constant;  $q_i$  and  $q_j$  are the atomic charges of atoms  $i$  and  $j$ , respectively;  $r_{i,j}$  is the distance between atom  $i$  and  $j$ .

**Equation 7.** Potential energy function of electrostatic between two atoms ( $i$  and  $j$ ).

Finally, the van der Waals interactions are designated by repulsive and attractive non-bonded interactions that are not described by the electrostatic interaction. AMBER uses a 12-6 Lennard-Jones potential as a function of the distance between two atoms to describe the van der Waals potential energy (**Equation 8**) (176).

$$V_{van\ der\ Waals}(i,j) = 4\epsilon_{i,j} \left( \left( \frac{\sigma_{i,j}}{r_{i,j}} \right)^{12} - \left( \frac{\sigma_{i,j}}{r_{i,j}} \right)^6 \right)$$

$\epsilon_{i,j}$  is the well depth;  $\sigma_{i,j}$  is the interatomic distance for which the energy is zero;  $r_{i,j}$  is the distance between atoms  $i$  and  $j$ .

**Equation 8.** Potential energy function of van der Waals interactions between two atoms ( $i$  and  $j$ ).

If we replace the terms of **Equation 1** by the terms of the previous equation, we end up with **Equation 9**:

$$V_{system} = \sum_{bond} \frac{1}{2}k_b(r - r_0)^2 + \sum_{angle} \frac{1}{2}k_a(\theta - \theta_0)^2 + \sum_{dihedral} \frac{1}{2}k_d(1 + \cos(n\omega + \gamma)) + \\ + \sum_{electrostatic} \frac{q_i q_j}{4\pi\epsilon r_{i,j}} + \sum_{van\ der\ Waals} \epsilon_{i,j} \left( \left( \frac{\sigma_{i,j}}{r_{i,j}} \right)^{12} - \left( \frac{\sigma_{i,j}}{r_{i,j}} \right)^6 \right)$$

**Equation 9.** Final potential energy function of the system.

## 1.2. Molecular Dynamics (MD)

Molecular Dynamics (MD) simulations predict how the atoms of the system will move over time and can be used for a variety of important biomolecular purposes, such as conformational change, ligand binding, protein folding, transport through the cellular membrane, among others. MD simulations can also predict, at the atomic level, how the systems will respond to perturbations, such as mutation, protonation, phosphorylation or addition/removal of a ligand.

MD simulations were firstly developed in the late 1950s (181) and the first simulation of a protein was performed in 1977 (182). Recently, MD simulations are frequently used when studying enzymatic mechanisms. Also, in neuroscience, these simulations have proven to be important when used to study neural signalling by critical protein (183), development of drugs targeting the nervous system (184) and mechanisms of protein aggregation related to neurodegenerative disorders (185).

In MD a set of conditions can be controlled, namely duration time, pressure, temperature, cut-off, periodic boundary and timestep. It is up to the user to set the best fitting conditions according to the movement of the system to be studied. For example, if the movement to be studied are the loops and terminal regions movements, the duration time of the MD simulation should be between the nano to microseconds time scale because that is the time that takes for those movements to happen.

Newton's equation is integrated in the MD simulation to predict the atom movement which results in data about velocity and position for each atom. The differential equation derivative from the Newton's Second Law (**Equation 10**) is defined for each system's time at each time point. However, due to the difficulties behind the analytical solution for this equation, it is necessary a finite integration step ( $\Delta t$ ) to numerically calculate individually the position (**Equation 11**) and velocity (**Equation 12**) for each atom in the system (186).

$$\frac{d^2 x_i}{dt^2} = \frac{F_{x_i}}{m_i}$$

**Equation 10.** Differential equation derivative.

$$\vec{x}_i(t_0 + \Delta t) = \vec{x}_i(t_0) + \vec{v}_i(t_0) \times \Delta t + \frac{1}{2} \vec{a}_i(t_0) \times \Delta t^2$$

$\vec{x}_i(t_0)$  is the atomic position at  $t_0$ ;  $\vec{v}_i(t_0)$  is the atomic velocity at  $t_0$ ;  $\vec{a}_i(t_0)$  is the atomic acceleration at  $t_0$ .

**Equation 11.** Atomic position calculation using the finite integration step  $\Delta t$ .

$$\vec{v}_i(t_0 + \Delta t) = \vec{v}_i(t_0) + \vec{a}_i(t_0) \times \Delta t$$

**Equation 12.** Atomic velocity calculation using the finite integration step  $\Delta t$ .



As suggested by the equations above, it is necessary to know at the beginning three different variables: position, velocity and acceleration. The atomic position can be obtained from X-ray crystallography or NMR, the velocity of each atom of the system is attributed randomly from a Maxwell-Boltzmann distribution and finally acceleration is described by the Newton's second law by the ratio of the force acting on the atom and the atomic mass (186).

### 1.2.1. Integration step

As previously mentioned, it is necessary to incorporate a finite integration step to set the time interval for position and velocity calculations for each atom. It is desirable to use a small integration step because it minimizes the errors and becomes closely to the analytical solution. However, it is necessary to consider that the smaller the integration step, the highest will be the computational cost. Therefore, to overcome this situation, it is common to use a ten times smaller integration than the fastest movement of the system.

For our system, the fastest event is the bond stretching of the hydrogen bonds that occurs with time lapses ranging the 10 fs. Applying the previous practice, we should end up with an integration step of 1 fs. However, we decided to set the integration step at 2 fs because of the integration of the SHAKE algorithm, which will be later described.

### 1.2.2. Non-bonded interactions cut-off

The non-bonded interactions can be split into short and long range, where the first are described by the van der Waals potential energy and calculated recurring to a 12-6 Lennard-Jones potential, where the highest term is  $r^{-6}$ . The second ones are described by Coulombic interaction, which have a  $r^{-1}$  interatomic distance dependency.

The calculation of all non-bonded atoms from all replicas is not possible because of the infinite number of interactions. Thus, an approximation is needed to reduce the number of interactions calculated. For this work, a 10.0 Å cut-off radius was set. We selected this radius because for distances higher than 10.0 Å the van der Waals interactions are practically insignificant and the Coulombic interactions could be easily cancelled out by the repulsive ones, which can result in a weak contribution for the energy calculation.

### 1.2.3. Periodic boundary conditions

When using MD simulations, the systems to be studied are composed of the protein and a surrounding water box, which is normally modelled as a cubic box. This can lead to a problem related to surface

effects, because the water molecules near the box surface are treated in different conditions comparing with water molecules inside the box, leading to additional errors.

Therefore, the periodic boundary conditions are resorted to overcome the surface effects, so the system is a central spot in an infinite cubic network consisted of cell replicas. To prevent abnormal results, it is necessary to set a cubic box that is big enough to prevent interactions of protein atoms from the replica units. Having that in mind, we set a minimum distance of 12.0 Å between the protein atoms and the unit surface, since we used a non-bonded interaction cut-off of 10.0 Å.

#### 1.2.4 SHAKE algorithm

The application of constrains in the MD simulations allows an increase of the integration step, because, as previously mentioned, integration step is directly related to the frequency of the fastest motions of the system. If we constrain these motions, which are the bonds involving a hydrogen, we can increase the integration step by a factor of 2-3 (187) leading to a less demanding computational cost. Many algorithms have been developed for the application of these constrains, being the most popular one the SHAKE algorithm, which was firstly introduced by Ryckaert et al. (188) in 1977.

## 2. Quantum Mechanics

Several quantum mechanics theories have been developed through the years. In this work, the electronic calculations were performed using Density-Functional Theory (DFT) with the B3LYP hybrid functional (189) and the basis set 6-31G(d,p) (190) was used. Therefore, in this section, a description of the methodology will be developed.

### 2.1. Density Function Theory (DFT)

DFT predicts the energy of the system using easier concepts and mathematically-less complex approaches when compared to wave function-based theories. The total number of electrons can be calculated by the integral of the electron density ( $\rho$ ) (**Equation 13**) (191).

$$N = \int \rho(r) dr$$

**Equation 13.** Total number of electrons calculated by the integral of electron density  $\rho(r)$ .

Nuclei are point charges, therefore they can be described as local maxima in the electron density. With this, calculations of electron density in the vicinity of a specific atomic nucleus can be determined according to the **Equation 14** (191).

$$\left. \frac{\delta \bar{\rho}(r_A)}{\delta r_A} \right|_{r_A=0} = -2Z_A \rho(r_A)$$

$\bar{\rho}(r_A)$  is the spherically averaged density;  $r_A$  is the radial distance from the atomic nucleus A;  $Z_A$  is the atomic number for atom A.

**Equation 14.** Electron density calculation.

With these concepts, the energy can be calculated using DFT as a functional of the electron density, named  $E[\rho]$ . Moreover, these calculations are much faster than *ab initio* methods when used in systems with more than 100 atoms.

### 2.1.1. Kohn-Sham Self-Consistent Field (SCF)

In 1965, the energy calculation of a system recurring to density function was achieved by Kohn and Sham (192). According to their proposal, the electron density of a hypothetical system where the electrons do not interact with each other, is identical to the ground-state density (**Equation 15**).

$$E[\rho(r)] = T_{ni}[\rho(r)] + V_{ne}[\rho(r)] + V_{ee}[\rho(r)] + \Delta T[\rho(r)] + \Delta V_{ee}[\rho(r)]$$

$T_{ni}[\rho(r)]$  is the kinetic energy of the non-interacting electrons;  $V_{ne}[\rho(r)]$  is the potential energy associated with nucleus-electron attraction;  $V_{ee}[\rho(r)]$  is the potential energy associated with electron-electron repulsion;  $\Delta T[\rho(r)]$  is the correction to the kinetic energy deriving from the interacting nature of the electrons  $\Delta V_{ee}[\rho(r)]$  is all the non-classical corrections to the electron-electron repulsion energy.

**Equation 15.** SCF theory energy calculation according to Kohn-Sham.

The total kinetic energy of this system is given by the sum of all individual electronic kinetic energies. This calculation requires the energy correction terms  $\Delta T[\rho(r)]$  and  $\Delta V_{ee}[\rho(r)]$  that are also referred to as exchange-correlation energy. The orbital expression can be written according to **Equation 16**.

$$E[\rho(r)] = \sum_{i=1}^N \left( \langle \chi_i | -\frac{1}{2} \nabla^2 | \chi_i \rangle - \langle \chi_i | \sum_{a=1}^M \frac{Z_k}{|r_i - r_k|} | \chi_i \rangle \right) + \sum_{i=1}^N \langle \chi_i | \frac{1}{2} \int \frac{\rho(r_j)}{|r_i - r_j|} dr_j | \chi_i \rangle + E_{xc}[\rho(r)]$$

**Equation 16.** Energy calculation considering orbitals.

### 2.1.2. Exchange-correlation functionals

DFT needs a technique to get a good exchange-correlation energy approximation. The functional can be divided into two, the exchange functional, which is associated to interactions between electrons with the same spin and the correlation functional, which is related to the interactions between electrons of the opposite spin.

Currently, the most used and the best functional to use in the enzymatic catalytic mechanism studies, such as ours, is the B3LYP hybrid functional that combines the parameters, Becke functional (B3) and LYP (Lee-Yang-Parr) functional with some HF terms (**Equation 17**) (191).

$$E_{XC}^{B3LYP} = (1 - a)E_X^{LSDA} + aE_X^{HF} + b\Delta E_X^{B88} + (1 - c)E_C^{LSDA} + cE_C^{LYP}$$

$a, b, c$  are empirical parameters.

**Equation 17.** B3LYP exchange-correlation energy calculation.

### 2.1.3. Basis Sets

Basis sets are defined as mathematical functions that can be used to describe atomic orbitals in quantum mechanical calculations such as DFT and *ab initio*. The more accurate is the orbital description the better are the results. However, this method has a computational cost and, therefore a compromise should be taken into account between accuracy and computational cost.

Gaussian-type orbitals (GTO) were introduced in 1950 by Boys and is defined accordingly to **Equation 18**.

$$\chi^{GTO}(x, y, z; \alpha, i, j, k) = \left(\frac{2\alpha}{\pi}\right)^{\frac{3}{4}} \left[\frac{(8\alpha)^{(i+j+k)} i! j! k!}{(2i)! (2j)! 2k!}\right]^{\frac{1}{2}} x^i y^j z^k e^{-\alpha(x^2+y^2+z^2)}$$

$\alpha$  determines the GTO width;  $i, j, k$  are non-negative integers;  $x, y, z$  are the atom position coordinates.

**Equation 18.** GTO function in atom-centered Cartesian coordinates.

If the sum of the  $i, j, k$  in equation 18 integers is zero, the GTO is an s-type of orbital. Meanwhile, if one of the integers gets the unitary value the GTO is defined by a p-type orbital that can have three combinations:  $p_x, p_y$  and  $p_z$ . Finally, the d-type of orbitals are defined by the sum of the integers being equal to two, which leads to a six Cartesian prefactors:  $x^2, y^2, z^2, xy, xz$  and  $yz$  (191).

The split-valence basis concept was introduced by Pople where the core orbitals are treated under a scheme of Gaussian primitives while the valence orbitals are treated using different schemes of Gaussian contraction. For example, in this work, the basis set used was 6-31G that can be characterized by six primitive GTOs for the core orbitals while the valence orbitals are divided into two: the most internal orbital is described by 3 primitives GTOs, while the external ones use only one (191).

Furthermore, polarization and diffusion functions can also be added in the basis sets. Polarization functions are characterized by a higher angular momentum of the valence orbitals. For example, in a hydrogen atom, a p-type orbital can polarize the s-type orbital, distorting their electron cloud, defining the chemical bond. Moreover, it is possible for d-orbitals to polarize p-orbitals, which are relevant for the second-period elements. The nomenclature for these characterization is defined with (d) or “\*” for orbital

polarization (e.g. 6-31G(d) or 6-31G\*) and with (d,p) or “\*\*” for p-orbitals polarization (e.g. 6-31G(d,p) or 6-31G\*\*) (190). Diffusion functions are used for the correct description of highly negative molecules, which electron cloud is considerably more displaced relatively to the nucleus. These functions are denoted by “+” for assignment of heavy atoms and with “++” for heavy and hydrogen atoms (193).

#### 2.1.4. Thermal corrections

In order to fully calculate the energy, internal energy calculation needs to be added to the previously described electronic energy. This calculation is of extreme importance because it provides the activation and reaction of free Gibbs variation ( $\Delta G$ ). This energy calculations, at a certain temperature can be calculated according to **Equation 19**.

$$E_T = E_{\text{electronic}} + [E_{\text{translational}} + E_{\text{rotational}} + E_{\text{vibrational}}]_T$$

**Equation 19.** Internal energy calculation considering a certain temperature.

The translational energy is calculated under the classical approach, rotational energy is calculated based on rigid rotor model and the vibrational energy is computed for each vibrational mode of a molecule.

Moreover, analysis of the vibrational energies gives the values of the frequencies in the system that are used to confirm and validate the minima of reactant and product and the transition state (TS). While both minima have only positive frequencies, TS is characterized only by one imaginary frequency.

### 3. QM/MM hybrid method

The application of DFT method is limited above a hundred atoms due to the high computational requirements and thus, it cannot be used for the whole system. Therefore, QM/MM hybrid methods have been developed where a small part of the system, which includes the active site, uses a QM-based method while the remaining system uses MM. Once again, it is up to the user to select the atoms that encompasses the QM area in order to obtain good results and accomplishable computational calculations.

In the present work the QM/MM methodology was used in order to analyse the catalytic mechanism, where DFT was used to describe the key atoms of the active site, and MM approach for the remaining system.

Commonly, the QM area encompasses the substrates and/or co-factor, amino acid residues involved in the reaction, and oxyanion-hole amino acid residues for their roles in the substrate stability. This area corresponds to the high-level layer (HL). All the remaining system and solvent is treated under MM methods and corresponds to the low-level layer (LL).

The energy system calculation can be provided by two types of approaches: The additive and subtractive methods. Because additive method has not accurate equation and parameters, the subtractive method was used in the present work. The energy calculation of this methodology can be accomplished according to **Equation 20** (194). At first, all the system is calculated under the MM theoretical level. Then, only the energy associated to the HL region is considered under the MM method. The subtraction of these two energy results in the calculation of the LL region. Lastly, the energy of the HL region is calculated using QM theoretical level. In this work, the energy calculation was obtained using ONIOM.

$$E_{QM/MM}^{All} = E_{MM}^{All} - E_{MM}^{HL} + E_{QM}^{HL}$$

**Equation 20.** Subtractive type of hybrid method energy calculation.

### 3.1. ONIOM

ONIOM (Our own *M*layered integrated molecular orbital molecular mechanics) (194,195) is currently one of the most used subtractive hybrid methods that requires an explicit description of charges and spin multiplicities for the different regions.

In this work, a two-layer system was set, where the HL layer calculations were performed under DFT (B3LYP) method, while for LL layer, MM approach was used. Adapting the previous equation, the energy of the system can be defined according to **Equation 21**.

$$E_{DFT/MM}^{All} = E_{MM}^{All} - E_{MM}^{HL} + E_{DFT}^{HL}$$

**Equation 21.** Energy calculation using the two-layered ONIOM method.

However, the hybrid method approach has a problem related with atoms linkage between different layers (194). This problem was solved using link atoms approach, where a hydrogen atom binds to the HL atoms whose bonds were cut in the separation of layers. The approach was performed using the Gaussian software, where the link atoms are added through a vector whose direction is dictated by the HL atom configuration. These added hydrogens are considered as LL atoms and the energy that were associated with the bonds that were cut were evaluated by MM method.

One other problem is related to the electrostatic and van der Waals interactions between atoms of different layers, where the boundary region tends to be over polarized. Thus, mechanical and electrostatic embedding methods were developed (194).

Mechanical embedding method is the simplest one where the HL region is calculated using the QM method with no concerns regarding the polarization. Afterwards, the LL region is calculated using the MM method sensing the HL polarization, which is introduced through punctual charges.

Contrarily to mechanical embedding method, electrostatic embedding approach allows the HL polarization through the LL region. This happens through the introduction of an additional mono-electronic term that is added to the QM Hamiltonian. In this method, the polarization of the LL region is neglected. Nevertheless, the results are usually considerably better than the ones obtained by mechanical embedding approach.

#### 4. Gaussian software

Gaussian is a software that is among the most popular software applications used in computational (bio)chemistry that was first developed by Pople in 1970 (196). Through the years the software has been continuously updated, being the most recent one the Gaussian16. The program packages all theoretical levels of theory that were previously described and can predict energies, vibrational frequencies and molecular properties of compounds, molecular structures and reactions in a wide variety of chemical environments. Furthermore, ONIOM computational technique is also included in the program. Transition state (TS) and minima structures of reactants and products can also be predicted and with these we can obtain the reaction energies and barriers of the mechanism.

The program also includes other functionalities such as: prediction of molecular properties in different solutions, modelling spectroscopy (Raman, NMR spectra and spin-spin coupling constants, Raman optical activity (ROA), Resonance Raman, UV/Visible, among others), which predicts a variety of spectra, in gas phase and in solution and excited state chemistry studies.

For this work, Gaussian09 (197) was utilized for the MD simulation and energy calculation of the catalytic mechanism.

#### 5. ORCA

Much like Gaussian software, ORCA (198) is also a multipurpose quantum chemistry research tool that can be used for a variety of computational chemistry applications. However, here it will only be focused the Coupled Cluster (CC) theory.

Coupled cluster theory is the most accurate way of introducing dynamic electron correlation into the wavefunction. CCSD(T) (coupled cluster singles and doubles with perturbative triples) method in ORCA shows remarkable accuracy in computing energies. Furthermore, the development of local correlation theories based on pair natural orbitals (PNOs) to a domain based local PNO (DLPNO) (199) method resulted in about 99.9% of the canonical correlation energy, while reducing the computational efforts.

Extrapolation techniques can overcome the problem with the slow convergence with respect to the basis set. The technique requires a systematic series that can be provided by cc-pVnZ, where  $n$  can be defined as D for the double-zeta basis set, T for triple-zeta basis set, etc (200). The convergence of HT energy to basis set limit (CBS) can be given by **Equation22**.

$$E_{SCF}^{(X)} = E_{SCF}^{(\infty)} + Ae^{(-\alpha\sqrt{X})}$$

$E_{SCF}^{(\infty)}$  is the basis set limit SCF energy;  $A$  and  $\alpha$  are constants;  $X$  is the cardinal number of the basis set.

**Equation 22.** Convergence energy calculation to CBS.

While the correlation energy is given by **Equation23**.

$$E_{corr}^{(\infty)} = \frac{X^\beta E_{corr}^{(X)} - Y^\beta E_{corr}^{(Y)}}{X^\beta - Y^\beta}$$

$X$  and  $Y$  are the cardinal numbers of the basis set;  $\beta$  is a constant.

**Equation 23.** Correlation energy calculation.

The final energy can be given by the sum of the convergence and the correlation energy. In this work DLPNO CCSD(T) Extrapolate (2/3,cc) cc-pVTZ/c was used for the single-point calculations.



# C. RESULTS

The work developed during this M.Sc. thesis involved two main parts. Part 1 comprises the creation and development of detailed database containing the experimental tridimensional structures of all enzymes currently known to be involved in the degradation of plastic. Part 2 involves the study of the catalytic mechanism of *α*-MHETase by hybrid QM/MM methods.

## 1. Plastic Biodegradation Enzyme Database

### 1.1. Scope

The Plastic Biodegradation Enzyme Database is a collection of structural, kinetics, mutagenesis, activity, and thermostability data of several enzymes with ability to degrade plastic. This is the first structural database regarding plastic biocatalysts, and we believe that it will be very useful for researchers working on the field of plastic degradation, because it integrates a variety of information at different levels concerning enzymatic properties of these enzymes. The overall data was manually checked and validated with the available literature for each enzyme. Currently, 223 entries of 28 different enzymes have been deposited. Each entry corresponds to one structure with an individual PDB code and by the name of protein and organism.

### 1.2. Methodology

To develop the database, the group searched manually several fields of search, regarding molecular, structural, and functional data.

In particular, articles with the keywords “plastic”, “biodegradation” and “structure” were searched on Scopus and Web of Science. Information was crossed with Uniprot database (101), BRENDA (201,202), and Protein Data Bank (42). In addition, the following databases were also used to check and validate information: Metacyc (203) and ESTHER database (204).

Presently, the database is composed by the following sections:

#### 1.2.1. Polymer

Indicated the type of plastic polymer that can be degraded by each enzyme is displayed in the database.

#### 1.2.2. Enzyme

Lists the most common name of each enzyme with plastic biodegradation ability. Other common designations are also listed.

#### 1.2.3. Organism

Organism from which the enzyme belongs.

#### 1.2.4. PDB code

4-letters code associated to the crystallographic structures of each of the enzymes, as used in the Protein Data Bank.

#### 1.2.5. Resolution (Å)

Resolution is a measure to the electron density map of a molecule's resolvability. The resolution range can influence the geometrical and structural studies, meaning that low resolution, shows a structure with almost no errors. Therefore, the resolution of each structure is displayed.

#### 1.2.6. Year of Deposition

The year of each crystallographic structure deposition on PDB database was also added. As technology advances it is common that the resolution of crystallographic structures is enhanced.

#### 1.2.7. Methods

Several methodologies to solve a crystallographic structure have been developed, including X-Ray diffraction (205), Nuclear Magnetic Resonance (NMR) (206), neutron diffraction (207), cryo-EM (208) and many others.

#### 1.2.8. State

Each enzyme can be in its free state or complexed with a ligand, substrate analogue, inhibitor, product, etc. This is an important field due to the conformational differences of each state. Furthermore, the field can facilitate the search of the researcher, depending on the study involved.

#### 1.2.9. Substrate / Ligand

Each complexed enzyme has its substrate/ligand identified and the database also provides information such as systematic name, identifies, molecular weight, isomeric SMILES, molecular formula, and several other properties.

#### 1.2.10. Mutations

Some three-dimensional structures are only available in the mutated form. This happens because often enzymes cannot be solved in its wild-type form, thus it is necessary to apply in-site mutagenesis in key residue positions. Furthermore, some variants represent engineered variants, reported to influence the enzymatic activity and thermostability.

#### 1.2.11. DOI Publication

DOI of the article describing the associated experimental structure.

#### 1.2.12. Chain

Several information relating the chains of each enzyme (number of chains, length, sequence and missing positions) available on PDB databank were included in the Plastic Biodegradation Enzyme Database.

#### 1.2.13. EC number and Gene name

Enzyme can be divided according to its Enzyme Commission number (EC number) or by its gene name. Both methodologies are commonly used and were added in the database. The data was obtained in PDB database and Brenda.

#### 1.2.14. Metal Ions

Some enzymes have metal ions, which can play a role in their activity or thermostability. This field presents this information.

#### 1.2.15. Metacyc

Metacyc Metabolic Pathway Database displays several metabolic pathways where some involve the enzymes of interest. Furthermore, the database displays a general information of the reaction and a summary of the enzymatic available data. Thus, whenever available, metacyc links regarding each enzyme were employed.

#### 1.2.16. Enzymatic Activity

All information regarding enzymatic activity against the desirable polymer is deployed here, whenever the data is available. Furthermore, if the data is available, assays regarding analogue substrates and mutated variants are also reported. The pH and temperature conditions are also included.

If information regarding the enzymatic activity against the target polymer is available in the paper where the crystallographic structure was solved, it is also mentioned in the database. Furthermore, if other substrates were used in those papers, they are also mentioned, as well as the assay conditions.

#### 1.2.17. Kinetic Parameters

Kinetic data such as turnover rate ( $k_{cat}$ ) and substrate binding affinity ( $K_M$ ) is a useful field that can give much information when it comes to the enzymatic reaction with the substrate. Therefore, it is employed in the database. All kinetic parameters values were obtained in literature.

#### 1.2.18. Thermostability

Thermostability is a key field when it comes to plastic biodegradation. For example, PET has a glass temperature ( $T_g$ ) of 76 °C and for a good enzymatic activity against PET substrates, the enzyme needs to

be thermostable around that temperature. Therefore, thermostability values, which are given by each enzymatic melting points are displayed in the database. These values were obtained in literature.

#### 1.2.19. Disulfide Bond

Disulfide bonds are bridges that are believed to influence the thermostability of an enzyme. Therefore, all disulfide bonds are displayed in the database.

#### 1.2.20. Catalytic Triad

The catalytic triad is a set of three amino acid residues found in the active site and are fundamental for the catalysis to occur. The mutation of one or more residues comprising the catalytic triad leads to an almost or completely activity loss. For this reason, the catalytic triad of each enzyme is included in the database. Information regarding this field was obtain in literature.

#### 1.2.21. Oxyanion Hole

Oxyanion hole is a pocket located in the active site where the backbone amine groups stabilize the substrate. This stabilization is important for the reaction to occur and therefore the amino acid residues comprising the oxyanion hole of each enzyme are reported. This information was obtained from the literature.

#### 1.2.22. Uniprot

Uniprot database grants many useful information when it comes to protein sequence and functional fields. Often, protein sequence of different crystallographic structures of the same enzyme are different, due to the usage of different methodologies to obtain the three-dimensional structures. This can lead to confusion when it comes to interpreting the data, because the same residues (e.g., catalytic triad residues) can have different position in the different crystallographic structures. Nevertheless, Uniprot uniforms the protein sequence, solving the previous problem. Thus, in the Plastic Biodegradation Enzyme Database it is employed the Uniprot protein sequence for key residues such as the ones comprising the catalytic triad, oxyanion hole and disulfide bond and also for mutated variants.

#### 1.2.23. FASTA sequence

The FASTA format sequence is a text-based format where the first line is a general description of the protein, which is followed by the amino acid residues sequence. With this, we can easily identify similar proteins, which might help uncover new biocatalysts.

### 1.3. Results and Discussion

Currently, the Plastic Biodegradation Enzyme contains structural information on 223 molecular systems of 28 different enzymes with the ability to degrade plastic. Some examples of these entries are displayed in Table 1. Of these 223 structures, 158 are responsible for the degradation of PET polymers, 31 Nylon, 14 polyhydroxybutyrate (PHB), 8 polyvinyl alcohol (PVA), 5 polylactic acid (PLA), 4 polybutylene succinate-co-butylene adipate) (PBSA), 2 polybutylene adipate terephthalate (PBAT), 1 polyacrylic acid (PAA) (Fig. 18). PET and Nylon are considered nonbiodegradable polymers while the remaining polymers are biodegradable.

**Table 1.** List of database entry examples in Plastic Biodegradation Enzyme Database.

Polymer	Enzyme	Organism	PDB code	Resolution (Å)	Disulfide bond	Catalytic triad	Oxyanion hole
PET	<i>IsPETase</i>	<i>Ideonella sakaiensis</i>	5XFZ	1.55	C203-C239; C273-289	S160; D206; H237	Y87; M161
PET	Cut2	<i>Thermobifida fusca</i>	4CG1	1.40	C241-C259	S130; D176; H208	Y60; M131
PET	<i>IsMHETase</i>	<i>Ideonella sakaiensis</i>	6QGA	2.10	C51-C92; C224-C529; C303-C320; C340-C348; C577-C599	S225; D492; H528	G132; E226
PET	<i>CaLipB</i>	<i>Candida antarctica</i>	1TCA	1.55	C47-C89; C241-C283; C318-C336	S130; D212; H249	T65; Q131
PET	<i>PaPETase</i>	<i>Pseudomonas aestusnigri</i>	6SBN	1.09	C214-C251; C285-C302	S171; D217; H249	F98; M172
PET	<i>SiCut190</i>	<i>Saccharomonospora viridis</i>	4WFK	2.35	C287-C302	S176; D222; H254	F106; M177
PET	<i>FoCut5a</i>	<i>Fusarium oxysporum</i>	5AJH	1.90	C48-C126; C188-C195	S137; D192; H205	Ser43; Gln123

PET	<i>TLip</i>	<i>Thermomyces lanuginosa</i>	4FLF	2.15	C44-C290; C58-C63; C126-C129	S168; D223; H280	S105; L169
PET	<i>FsCut</i>	<i>Fusarium solani</i>	1FFD	1.69	C47-C194; C125-C187	S136; D191; H204	S58; Q137
PLA	<i>cle</i>	<i>Cryptococcus</i> sp. S-2	2CZQ	1.05	C6-C78; C161-C168	S119; D199; H214	T51; Q120
PHB	<i>PhaZ7</i>	<i>Paucimonas lemoignei</i>	4BTV	1.59	C41-C49; C74-C123; C209-C222; C284-C293; C363-C368	S174; D280; H344	N87; M175
PHB	PHB depolymerase	<i>Penicillium funiculosum</i>	2D80	1.71	C70-C79; C169-C180; C234-C241; C250-C304	S39; D121; H155	S40; C250
PBAT	<i>estA</i>	<i>Clostridium botulinum</i>	5AH1	1.20	-	S210; D412; H454	-
PAA	<i>PahZ1KT-1</i>	<i>Sphingomonas</i> sp.	6VE6	2.45	-	S176; D244; H299	-
PLA	MGS0156 Metagenomic carboxylic esterase	uncultured organism	5D8M	1.95	C173-C287	S232; D350; H373	L169; K233
Nylon	<i>nylB</i>	<i>Flavobacterium</i> sp. K172	2ZM8	1.55	-	S112; K115; Y215	-
Nylon	<i>nylA</i>	<i>Arthrobacter</i> sp. K172	3A2Q	1.80	-	K72; S150; S174	A171; A172
PVA	<i>oph</i>	<i>Pseudomonas</i> sp.	3WL5	1.60	C53-C185; C288-C298; C323-C370	S203; D284; H329	-

“-“ Missing information

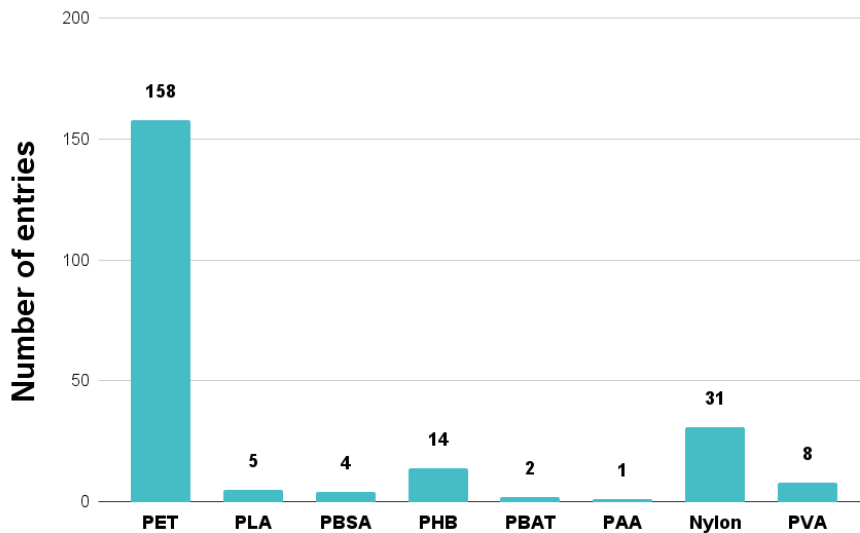


Figure 18. Number of polymer entries.

The organisms that are responsible for the production of biocatalysts for plastic degradation are mostly bacteria and fungus and a few yeasts. The database contains 34 entries for *Ideonella sakaiensis*, 46 for *Fusarium solani*, 25 for *Candida antarctica*, 25 for *Thermomyces lanuginosa*, 11 for *Saccharomonospora viridis*, among others (Fig. 19). Furthermore, the entries of the enzymes produced by these organisms are demonstrated in Figure 20.

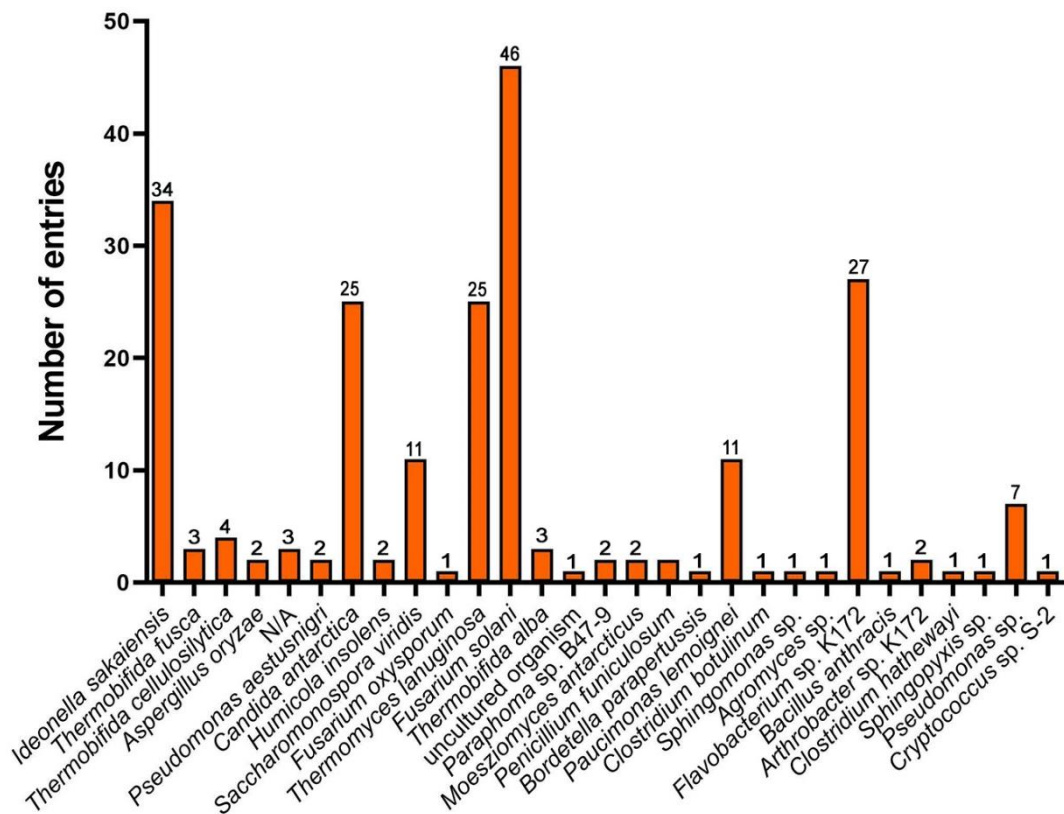


Figure 19. Number of organism entries.



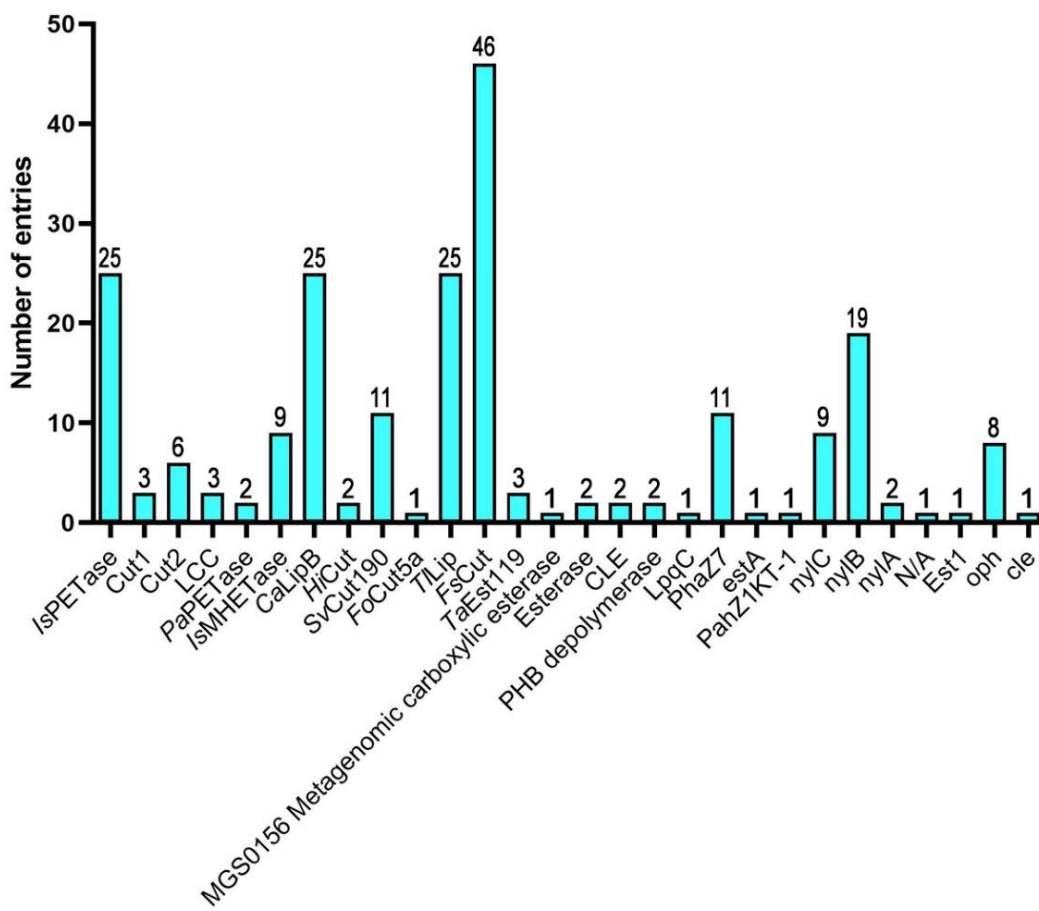


Figure 20. Number of enzymatic entries.

Mutagenesis data can reveal critical information of amino acid residues with special roles in enzymatic activity, thermostability, ligand binding, etc. For that reason, whenever there is a mutation in the enzymatic crystallographic structure, a description of the effects by the variants on the enzymatic activity and thermostability, kinetic parameters and structural conformations are employed.

#### 1.4. Conclusion and Future Works

In conclusion, the database developed includes several data relating plastic biocatalysts. We believe that the database will be important for researchers of the plastic biodegradation field as it is the first database of the sort to be developed. Presently, 223 entries involving 28 enzymes are displayed. In the future, we will keep updating the entries as new crystallographic structures are solved and we believe that soon the database will be publicly available. Furthermore, features such as “advanced search” where the viewer can select specific fields in order to facilitate the research will be employed. Also, 3D interactive structure of the protein and 2D and 3D interactive maps of the complexed structures will be displayed. Lastly, it

will be displayed an option selection where the viewer can suggest a new crystallographic structure that will be reviewed and confirmed manually by the team.

## 2. *l*sMHETase Catalytic Mechanism

### 2.1. Scope

The main goal of this work is the study of the catalytic mechanism of *l*sMHETase complexed with the PET polymer intermediate MHET, using the hybrid QM/MM method, to understand with the atomic level detail how the enzyme performs its activity. The calculations revealed that the mechanism is divided into two global steps – acylation, where an acyl-enzyme intermediate is formed and deacylation, where hydrolytic release of the intermediate occurs, making the enzyme ready for a new catalytic cycle. These overall steps are further divided into a 3 and 2-step processes, respectively. When we were acquiring information relating the enzyme and computational studies, no computational studies on the catalytic mechanism of *l*sMHETase had been reported. However, while we were preparing our first structures, a paper published by Knott et al. (54) provided some light into the catalytic mechanism of this enzyme. Therefore, a comparison of our results with the ones obtained by the group will be also presented.

### 2.2. Methodology

#### 2.2.1. Structure preparation

According to the Plastic Biodegradation Enzyme Database, only 9 experimental structures of *l*sMHETase had been reported. From these, only one had a nonhydrolyzable ligand, mono-(2-hydroxyethyl) terephthalamide (MHETA), which is an analogue of the substrate MHET. Therefore, a model of the substrate MHET was constructed based on the previous ligand, using Gaussian09 (197). In the following section a description of the structures and the procedures realized to prepare the models will be described.

##### 2.2.1.1. PDB analyses

Two structures were selected from the Protein Data Bank for the modelling of the system (PDB codes: 6QGA (chain A) and 6QZ4 (chain A)) determined by Palm et al. (55) and Knott et al. (54), respectively. Both structures are monomers.

The structure under the 6QGA PDB code is complexed with the MHETA ligand. The difference between MHETA and MHET is the appearance of an amide group instead of a carboxyl group. Using GaussVIEW, we replaced this nitrogen with an oxygen atom, restoring the model of interest for this study (Fig. 21).

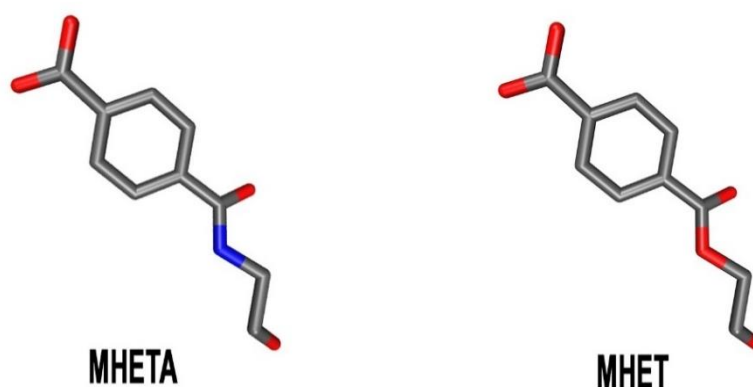


**Figure 21.** Representation of MHETA and MHET substrates.

However, the protein under the same PDB code lacks some amino acid residues in positions 1-42, 50-51, and 603 containing, in total, 558 amino acids. The other structure 6QZ4 is currently the most complete structure with 568 amino acids and was used to fill the gaps in positions 35-42, 50-51 and 603. Before the structural alignment of the two structures, all surrounding sulfates were removed.

#### 2.2.1.2. Protonation states

Protonation of all the ionizable amino acid residues in the enzyme, namely lysine, arginine, histidine, glutamate and aspartate were checked in order to increase the accuracy of the results using two different methods. The first initial protonation proposal was given by the server H++ at pH 7 and the second was given by PROPKA 3 software. Both resulted in the single protonation of His91 and His528 at N $\delta$ ; His293, His467 and His488 were protonated at N $\epsilon$ ; His166 and His241 were doubly protonated. Furthermore, the MHET substrate and a glutamate in the position 230 were also protonated. The remaining amino acids were maintained in their dominant form at pH 7.

#### 2.2.1.3. LEaP

LEaP program from the AMBER package was used to prepare the system using the ff14SB forcefield. MHET substrate was parameterized accordingly. The resulting structure was solvated with a TIP3P type water molecule with a 12 Å minimum distance. The system resulted in a total solute charge of -7, being neutralized by adding 7 sodium ions and its ready for the molecular dynamics simulation.

#### 2.2.1.4. Molecular Dynamics Simulation

The resulting system was then minimized through a set of four sequential minimization protocols with the non-bonded interactions cut-offs set to 10 Å. The first three sequential minimizations relate to the minimizations of water molecules, all hydrogen bonds and the whole system, except backbone atoms, respectively were set with 2500 (1250 steepest descent (ST) + 1250 conjugated gradients (CG)) steps. The last minimization is the minimization of the whole system, and 10000 (5000 ST + 5000 CG) steps were set. The MD simulation was performed using the algorithm SHAKE to constraint the bonds involving hydrogen atoms, allowing the use of a 2-fs integration step and had a simulation length of 1.3 μs. Furthermore, temperature and pressure were set to 303 K and 1 bar, respectively, using the Langevin thermostat to simulate the temperature and Berendsen to simulate the pressure. The model selected for the QM/MM calculation was the one obtained in the fourth minimization due to critical distances being more optimal for the reaction to occur (Fig. 22).

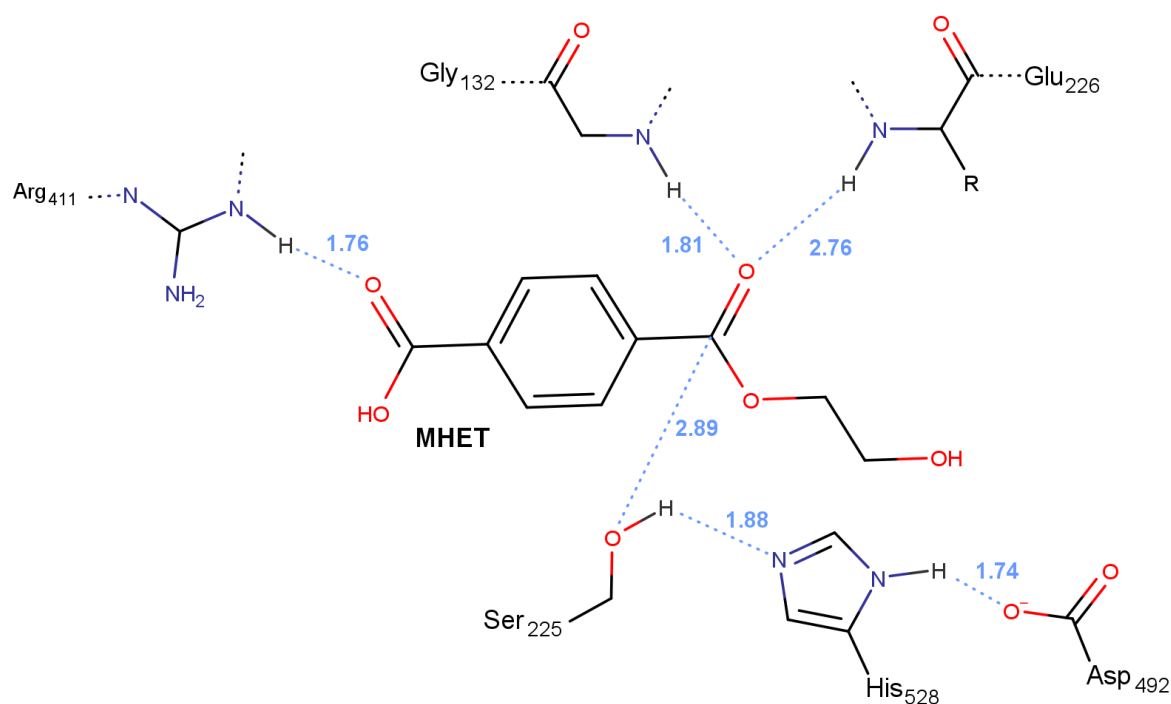


**Figure 22.** Fourth minimization model with critical distances represented.

#### 2.2.1.5. QM/MM model

The minimized structure was loaded using the molUP (209) plugin for Visual Molecular Dynamics (VMD) (210), a plug-in is available in the VMD Store (211). This extension is able to prepare the Gaussian09 (197) input files.

The QM/MM model selected from the minimized structure is encompassed by *s*MHETase structure and an 8 Å coat of water molecules surrounding the structure. Because no significant rearrangements of the enzymatic structures are to be expected during the catalysis, we opted to fix the atoms located more than 7 Å away from the active site. All the atoms within this range were maintained free during the geometric optimizations in order to accommodate the conformational changes that occur in the active site. However, the active site was too exposed to the exterior. Therefore, a shell comprised by water molecules was added in the outer side of the protein up to 15 Å from the active site.

In this model, the high-level (HL) layer was set to be comprised by 71 atoms involving the MHET substrate, the catalytic triad sidechains (Ser225, His528 and Asp492), the backbones of two residues (Gly132 and Glu226) involved in the stabilization of the oxyanion hole, and a surrounding arginine residue (Arg411). In deacylation stage a water molecule was added, making a total of 74 atoms for the HL. These amino acids, apart from the substrate itself, were selected due to their proximity to the MHET substrate. Meanwhile, the remaining atoms were selected to be part of the low-level (LL) layer. The HL layer is treated with quantum mechanics B3LYP/6-31G(d,p) (191) calculations, while LL layer is treated with molecular mechanics method using AMBER ff14SB (212). Before the relaxed coordinate scan, the structure was optimized using first a mechanical-embedding optimization and later an electrostatic embedding optimization scheme. The relaxed coordinate scans and geometry optimization of transition states (TS) and minima (reactant and product) were also performed using B3LYP/6-31G(d,p):ff14SB with optimizations being done considering the electrostatic embedding scheme.

#### 2.2.1.6. Thermal corrections

In addition to the electronic energies, thermal corrections were calculated, allowing the determination of all thermodynamic quantities ( $\Delta S$ ,  $\Delta H$ , and  $\Delta G$ ). These corrections provide a good estimative activation and reaction Gibbs free energies.

#### 2.2.1.7. Single-point calculations

In order to refine the computed energies, single-points energy calculations using DLPNO-CCSD(T)/CBS (199), extrapolated from cc-pVDZ and cc-pVTZ calculations (200). The single-point energy calculations were performed using ORCA 4.2.1 (213). The HL layer was isolated from the QM/MM system for each minimum and transition state. A single-point energy calculation was performed on these systems using B3LYP/6-31G(d,p) and DLPNO-CCSD(T)/CBS considering the surrounding molecular mechanics point charges of the LL layer. The energy difference was summed to the total energy of the system as an energy correction.

## 2.3. Results

According to the calculations performed, the catalytic mechanism occurs through five sequential steps, which are divided into acylation and deacylation.

### 2.3.1. Acylation

The first overall step is the acylation where the formation of the acyl-enzyme intermediate and the exiting of EG product occurs. This process occurs in three sequential steps.

#### 2.3.1.1. Step 1

The first step occurs when His528 deprotonates Ser225, which enhances its nucleophilic character and attacks the carbonyl carbon of MHET. It is also observed a simultaneous hydrogen transfer from His528 to Asp492 (Fig. 23). These findings were confirmed when comparing the reactant and product minima calculations. The proton involved in the deprotonation of Ser225 by His528 is found at 1.64 Å from the hydroxyl group of Ser225 while the hydrogen bond between His528 and Asp492 is found within 1.54 Å from His528-N in the reactant minima structure while in the product these distances are 1.03 and 1.04 Å, respectively (Fig. 23).

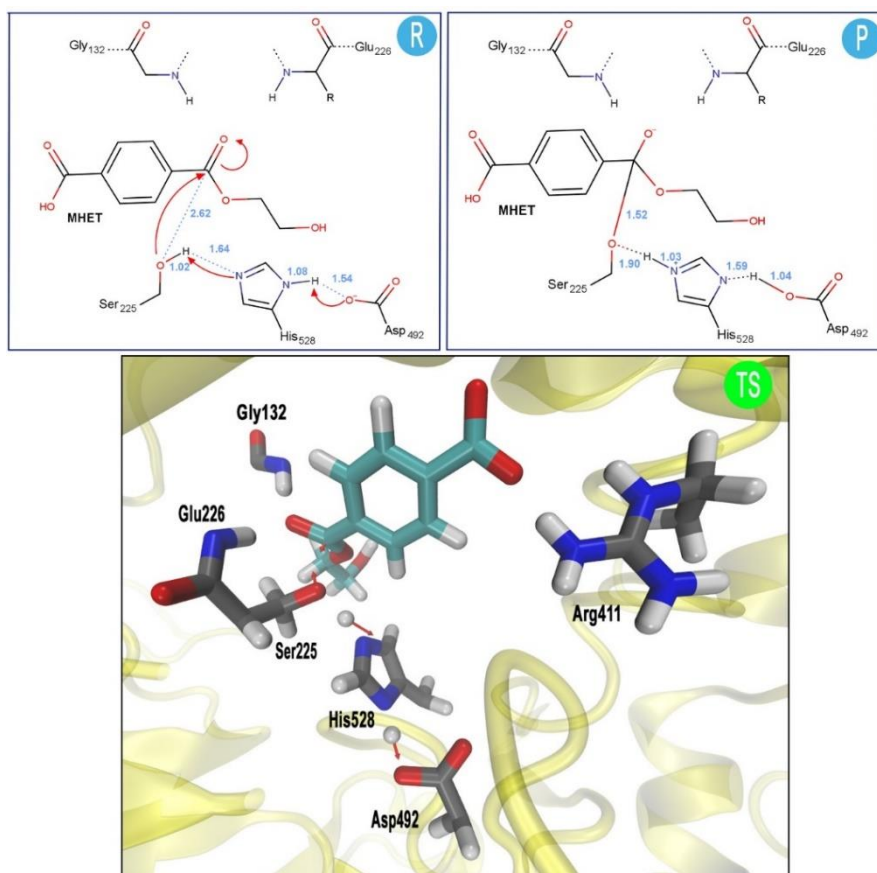


**Figure 23.** Reactant (R), transition state (TS) and Product (P) structures with distances of the atoms involved in the step 1 displayed.

TS was confirmed with a single imaginary frequency at  $260.34i \text{ cm}^{-1}$ . The activation energy ( $E_a$ ) resulted from this step was about  $6.90 \text{ kcal/mol}$ , which is a feasible result, while the reaction energy ( $E_r$ ) revealed a slightly exothermic reaction ( $-0.75 \text{ kcal/mol}$ ) (Fig. 24). Furthermore, it is possible to observe that HL layer contributes the most for the activation and reaction energies, once LL layer contribution is only  $-0.23$  and  $0.56 \text{ kcal/mol}$ , respectively (Fig. 25). This low contribution of the LL layer means that a good assessment of HL-LL layers was accomplished. When using thermal corrections, the activation and reaction energies are referred as free Gibbs energy of activation ( $\Delta G^\ddagger$ ) and reaction ( $\Delta G_r$ ). For this step, it was obtained a  $\Delta G^\ddagger$  of  $4.25 \text{ kcal/mol}$  and a  $\Delta G_r$  of  $-0.59 \text{ kcal/mol}$ . After single-point (SP) calculations, the  $\Delta G^\ddagger$  and  $\Delta G_r$  were  $6.44$  and  $-1.74 \text{ kcal/mol}$ , respectively (Fig. 24).

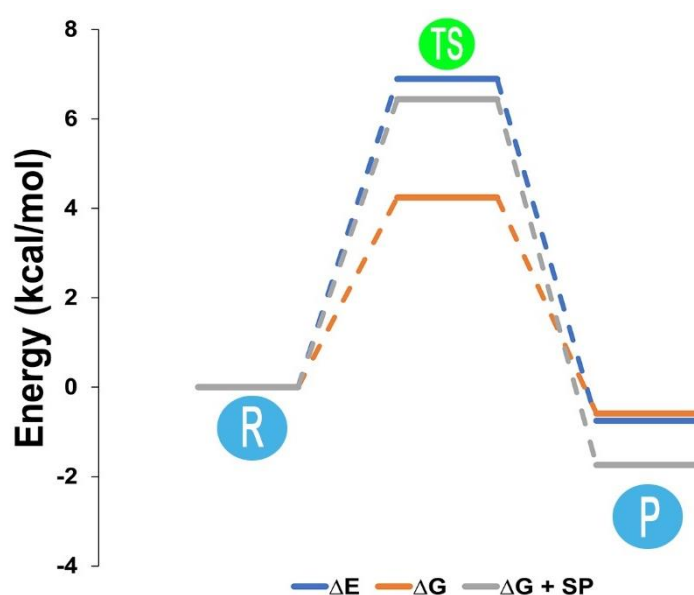


**Figure 24.** Energy profile of  $\Delta E$  ( $6.90$  and  $-0.75 \text{ kcal/mol}$ , for activation and reaction, respectively)  $\Delta G$  ( $4.25$  and  $-0.59 \text{ kcal/mol}$ ) and  $\Delta G + SP$  ( $6.44$  and  $-1.74 \text{ kcal/mol}$ ) of step 1.

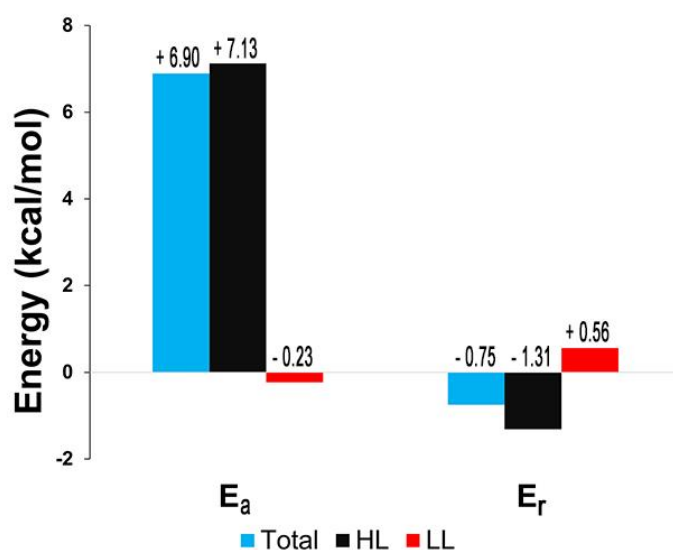


**Figure 25.** Activation and reaction energies and the contribution of HL and LL layers in step 1.



### 2.3.1.2. Step 2

The second step is the breaking of the MHET substrate C $\alpha$ -C bond, originating the EG product. This is confirmed by the distance deviation in the reactant and product minima (1.55 and 2.43 Å, respectively).

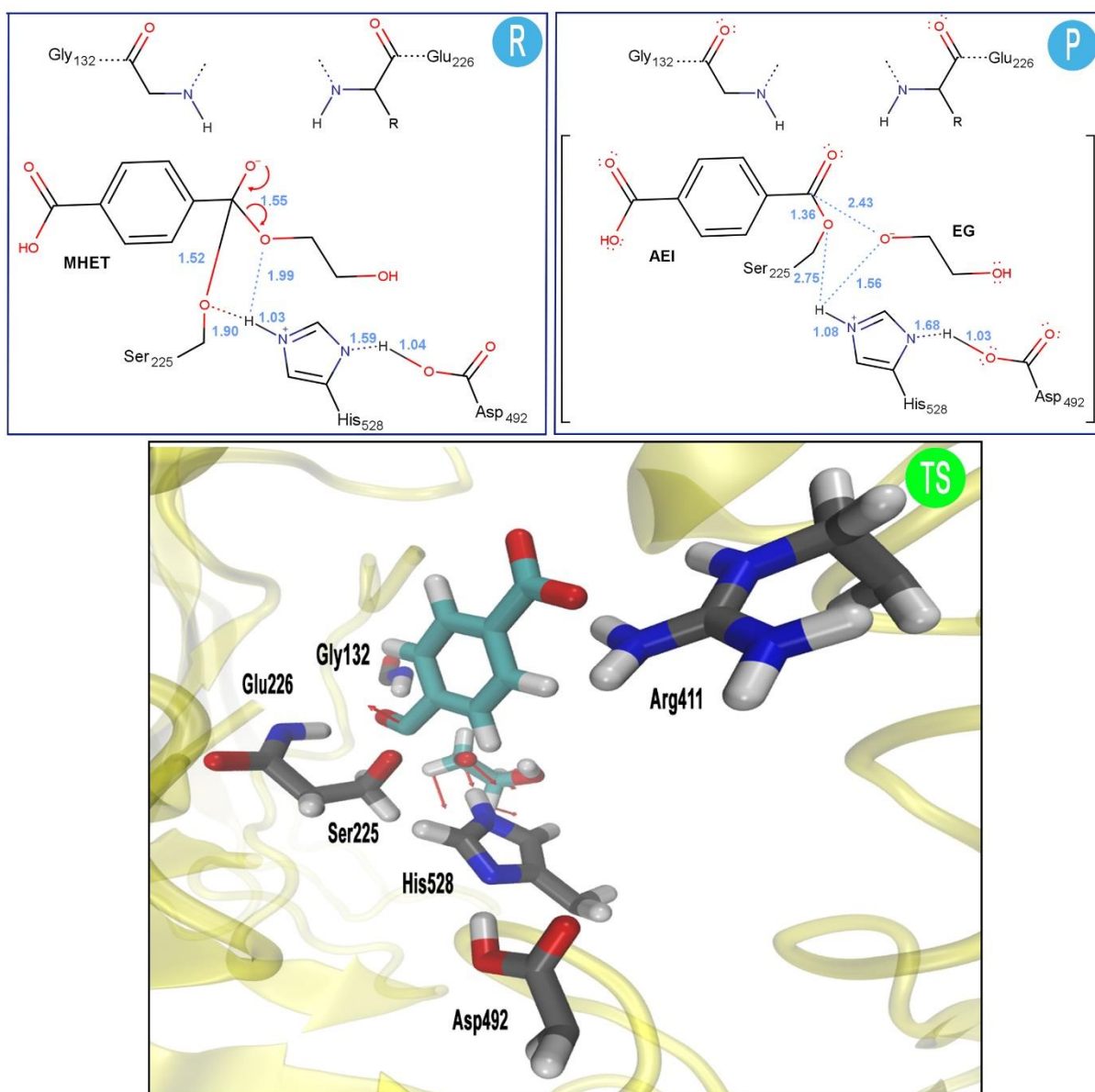


**Figure 26.** Reactant (R), transition state (TS) and Product (P) structures with distances of the atoms involved in the step 2 displayed.

After careful analyses we can see that the proton that was transferred to Ser<sub>225</sub> by His<sub>528</sub> approximates to the negatively charged oxygen of EG block (1.99 Å at reactant vs 1.56 Å at product) (Fig. 26). However, this approximation is not enough for the protonation of EG, suggesting that it will only occur in the next step.

The activation energy was 3.90 kcal/mol, and TS was confirmed by the imaginary frequency at 67.04i  $\text{cm}^{-1}$ . Meanwhile, the reaction energy revealed an endothermic reaction ( $E_r$  3.79 kcal/mol) (Fig. 27). The influence of LL layer in these results is insignificant (0.49 and 0.79 kcal/mol, for activation and reaction energies, respectively), validating the selection of the QM model atoms (Fig. 28). Combining these results with the thermal corrections resulted in a  $\Delta G^\ddagger$  of 3.97 kcal/mol and a  $\Delta G_r$  of 2.85 kcal/mol. After SP calculations, the final energy barrier of activation and reaction were revealed to be 8.84 and 7.73 kcal/mol, unravelling an exergonic step (Fig. 27).

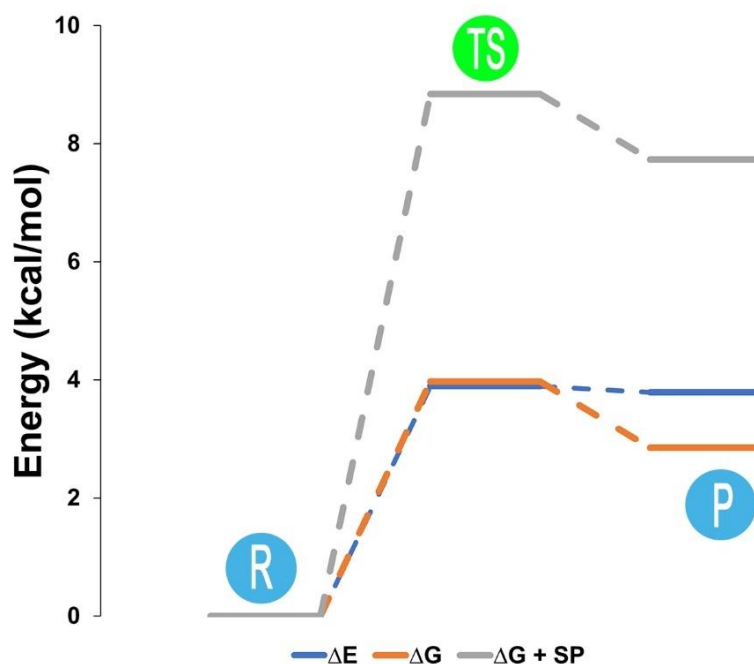


**Figure 27.** Energy profile of  $\Delta E$  (3.90 and 3.79 kcal/mol, for activation and reaction, respectively)  $\Delta G$  (3.97 and 2.85 kcal/mol) and  $\Delta G + SP$  (8.84 and 7.73 kcal/mol) of step 2.

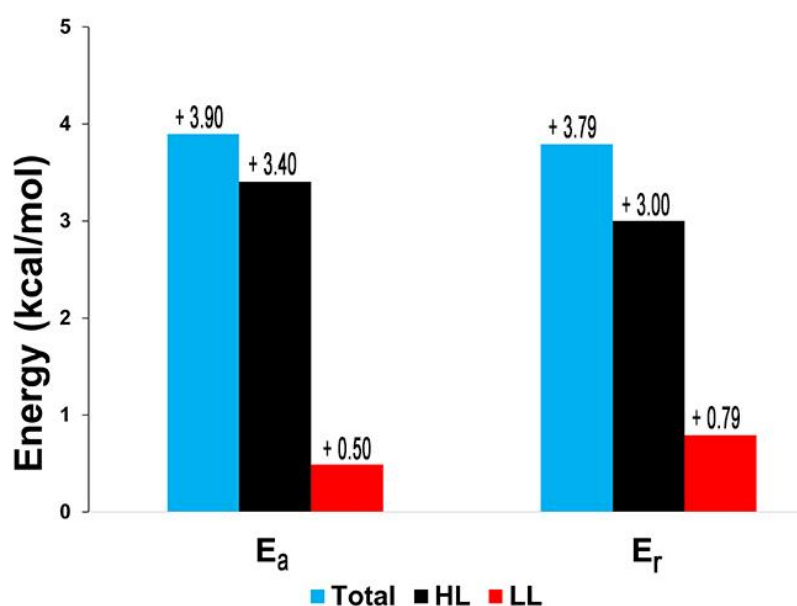


**Figure 28.** Activation and reaction energies and the contribution of HL and LL layers in step 2.

### 2.3.1.3. Step 3

The third and final step of acylation, confirmed the previous suggestion of the proton binding to the negatively charged oxygen of EG. This was confirmed while comparing the distance of the two atoms in the reaction and product minima (1.56 and 1.01 Å, respectively) (Fig. 29).

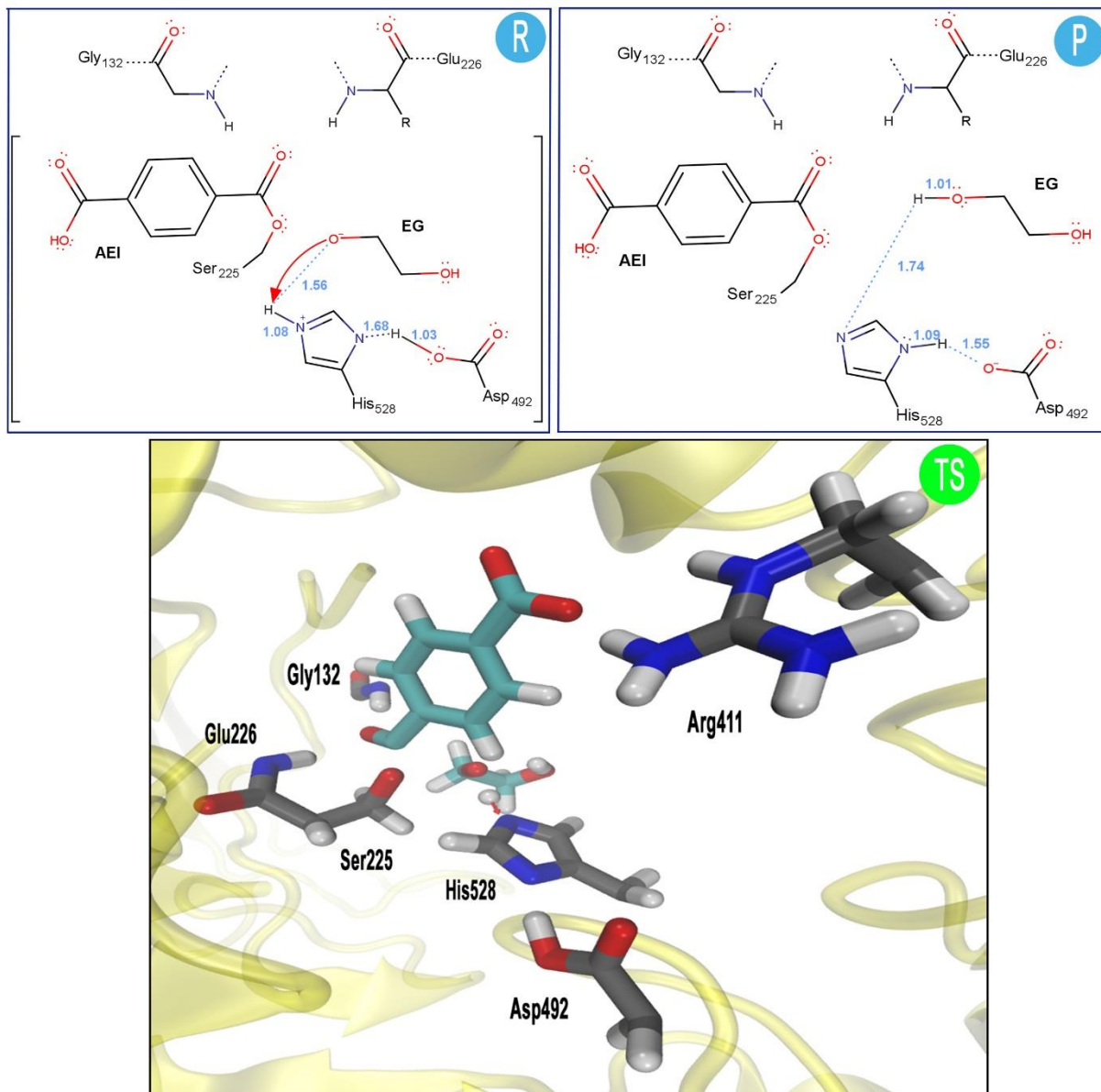


**Figure 29.** Reactant (R), transition state (TS) and Product (P) structures with distances of the atoms involved in the step 3 displayed, confirming the proton transference.

In this step, the activation and reaction energies were 0.53 and -4.38 kcal/mol, revealing an exothermic reaction (Fig. 30). TS was confirmed by the imaginary frequency at 655.89i  $\text{cm}^{-1}$ . Adding the thermal corrections to this, both energies become negative (-1.16 and -3.26 kcal/mol for  $\Delta G^\ddagger$  and  $\Delta G$ , respectively). We believe that the negative value of the activation energy suggests a spontaneous step triggered by the entropic contribution. After SP calculations the final activation energy was set to be -1.12

kcal/mol while the final reaction energy revealed a very exergonic reaction (-6.80 kcal/mol) (Fig. 30).  
 Once again, the contribution of LL layer was relatively low (Fig. 31).

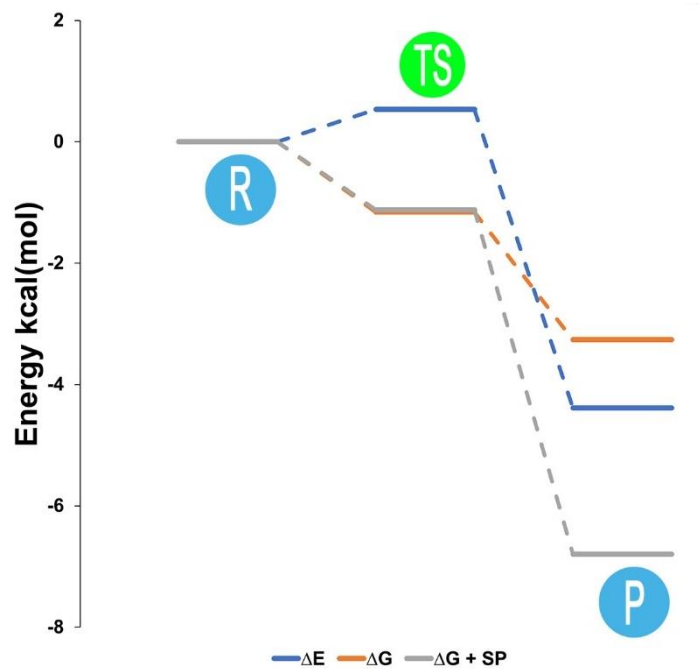


**Figure 30.** Energy profile of  $\Delta E$  (0.53 and -4.38 kcal/mol, for activation and reaction, respectively)  $\Delta G$  (-1.16 and -3.26 kcal/mol) and  $\Delta G + SP$  (-1.12 and -6.80 kcal/mol) of step 3.

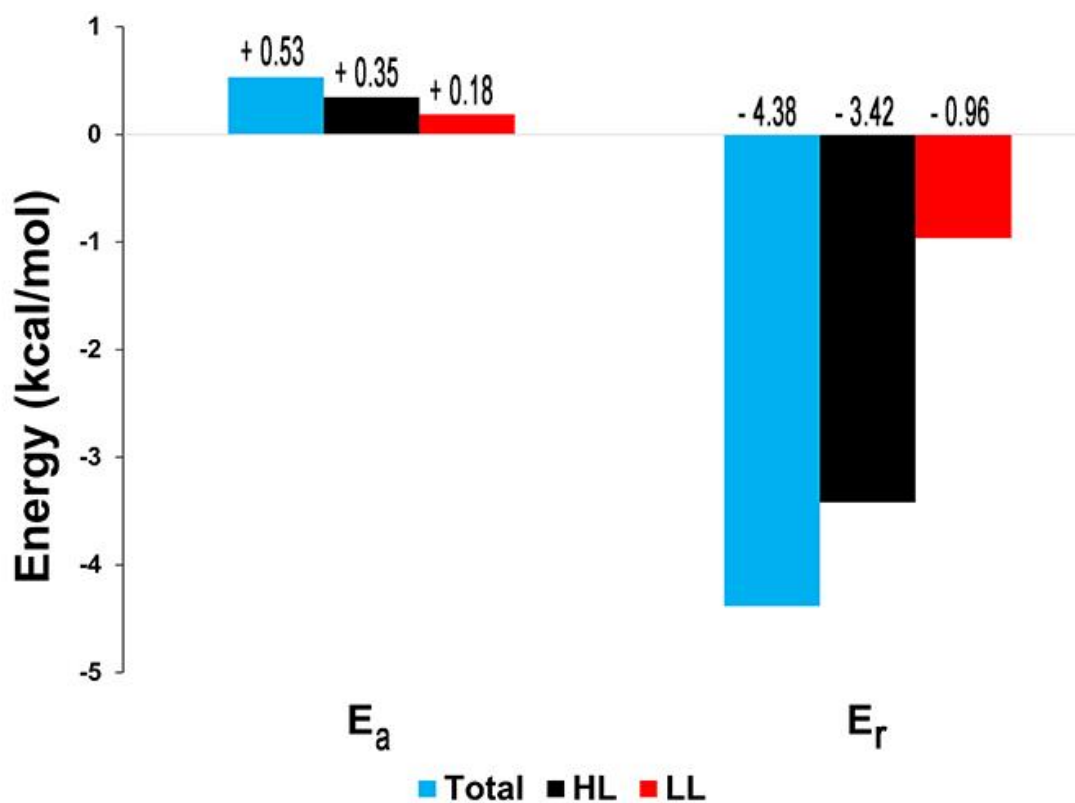


**Figure 31.** Activation and reaction energies and the contribution of HL and LL layers in step 3.

At the end of this step, the acyl-enzyme intermediate is formed. Overall, the acylation step resulted in an activation energy of 8.87 kcal/mol.

### 2.3.2. Deacylation

After the exiting of the EG block and consecutive formation of the acyl-enzyme intermediate a water molecule from the LL layer was included into the HL layer for the hydrolysis to occur, adding up a total of 74 amino acid residues treated with B3LYP/6-31G(d,p).

#### 2.3.2.1. Step 4

This step marks the start of deacylation. Because of the liberation of EG block, a water molecule can occupy its previous space. Therefore, a water molecule was moved into the according position. In this step, the water molecule makes a nucleophilic attack to the acyl-enzyme intermediate. In order to uncover the TS, linear scan was performed. However, due to some issues with microinteractions on the TS optimization, we are unable to show the energies of activation and reaction of step 4. Nevertheless, we are still working in this step.

#### 2.3.2.2. Step 5

The final step of deacylation and the overall mechanism, reveals a regeneration of Ser225, by the transference of the proton originated from the deprotonation of the water molecule by His528. This transference was confirmed while comparing the distance of the proton with the oxygen of the hydroxyl group of Ser225 in the reactant and product minima. The distance decreased from 1.48 Å in reactant to 1.01 Å in product (Fig. 32). Again, linear scan was run to uncover the TS point, which was confirmed by the single imaginary frequency of 302.87i cm<sup>-1</sup>. The minima and TS structures revealed an activation energy of 8.59 kcal/mol and an endothermic reaction of 1.57 kcal/mol (Fig. 33). After the thermal corrections, it was observed a decrease of energies, being  $\Delta G^\ddagger$  and  $\Delta G_r$ , 4.16 and -0.34 kcal/mol respectively. Finally, the SP calculations revealed a final energy of 8.74 and 1.95 kcal/mol for activation and reaction, respectively (Fig. 33). Moreover, the LL layer contribution was much lower than the HL layer contribution (Fig. 34).

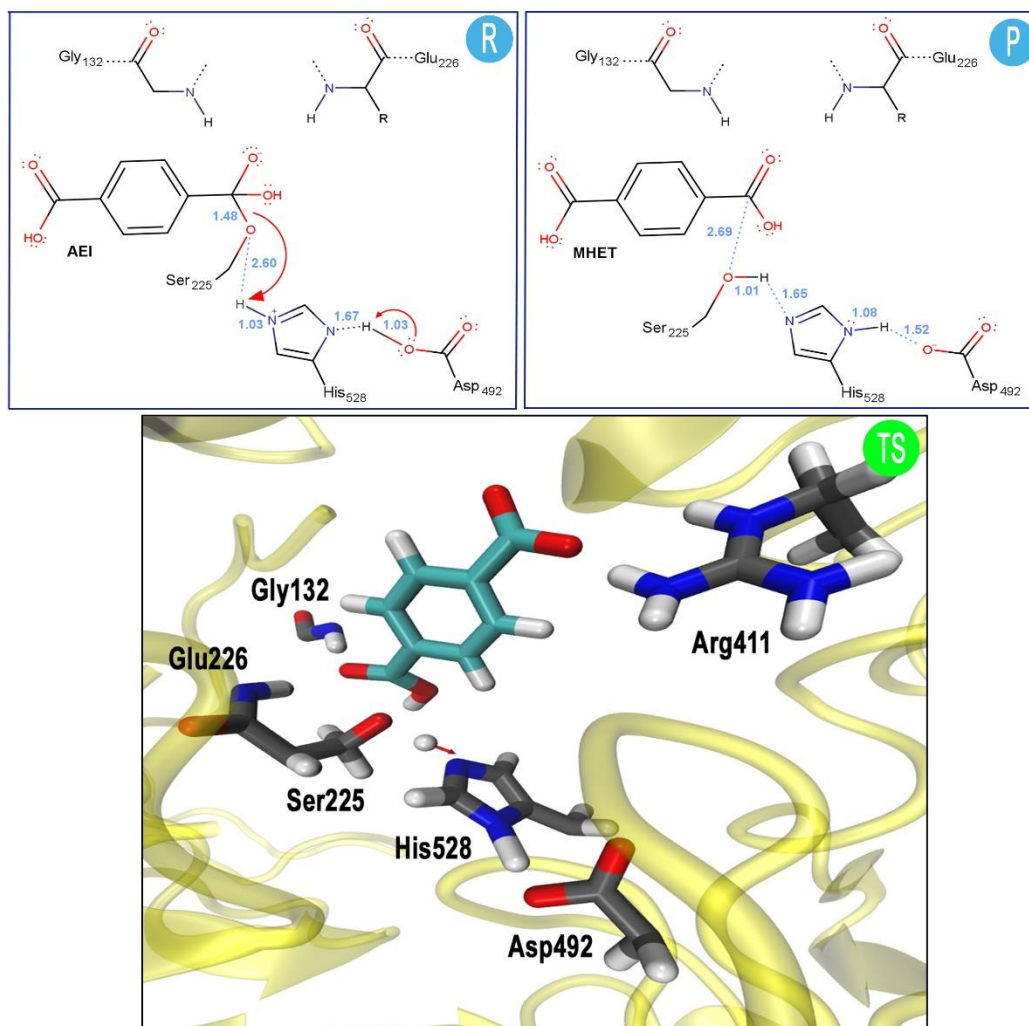


**Figure 32.** Reactant (R), transition state (TS) and Product (P) structures with distances of the atoms involved in the step 5 displayed, confirming the regeneration of Ser225.

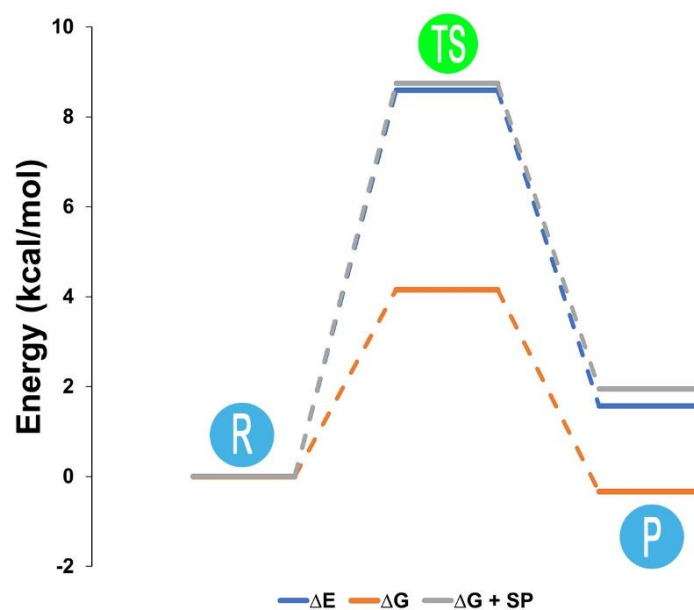


**Figure 33.** Energy profile of  $\Delta E$  (8.59 and 1.57 kcal/mol, for activation and reaction, respectively)  $\Delta G$  (4.16 and -0.34 kcal/mol) and  $\Delta G + SP$  (8.74 and 1.95 kcal/mol) of step 5.

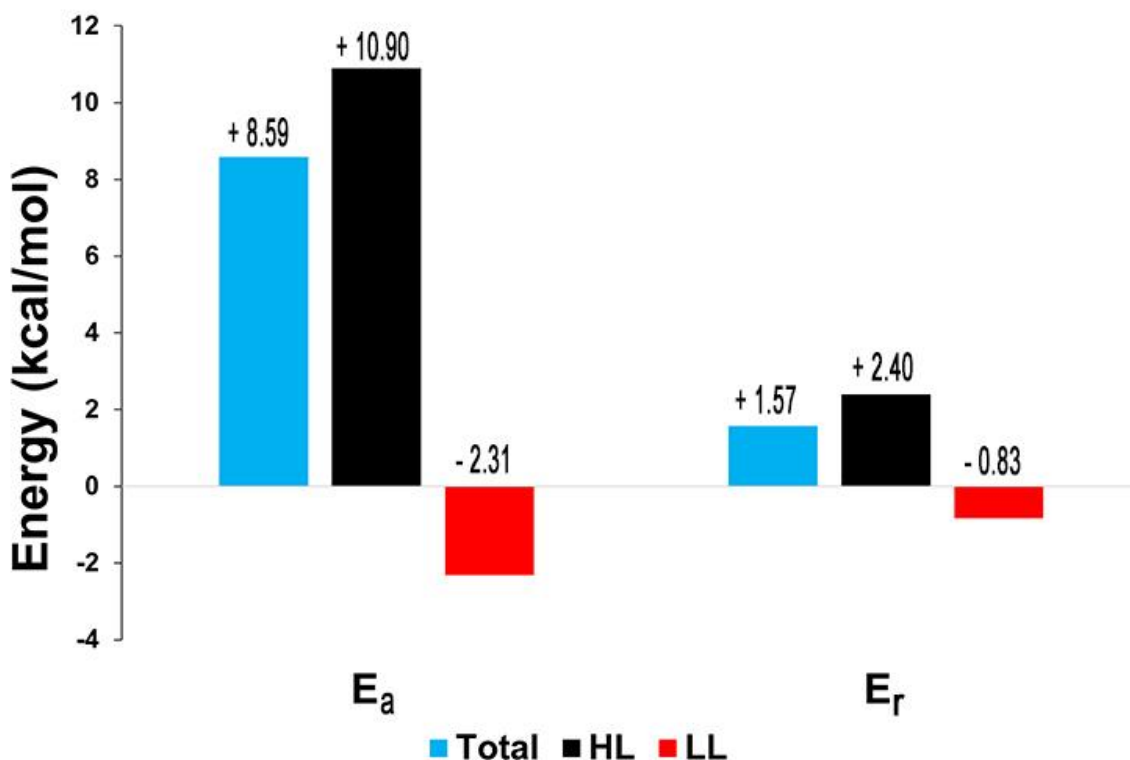


**Figure 34.** Activation and reaction energies and the contribution of HL and LL layers in step 5.

## 2.4. Comparison with other catalytic mechanism

As previously stated, in this section a comparison of the catalytic mechanism reported in this paper with the one reported by Knott et al. (54) will be described.

While in our system, the substrate MHET was obtained by replacing an atom in the ligand of 6QGA PDB structure and minimized using Gaussian09, the other group built it from scratch, using Schrodinger's Protein Preparation Wizard (214) and minimized it using Schrödinger LigPrep (215). Furthermore, they used the H++ server (216) at 7.0 pH in order to look for the initial protonation states (in our study we used both H++ server and PROPKA3 (217) at pH 7.0). The results were according to ours, with a single protonation at N $\delta$  in His91 and His528, single protonation at N $\epsilon$  in His293, His467, and His488 and doubly protonated in His166 and His241. Glu230 was found also protonated in both systems.

When it comes to MD simulation performances, we used AMBER software and ff14SB force fields, while Knott et al. (54) went with CHARMM (Chemistry at HARvard Macromolecular mechanics) (177) using CHARMM36 force fields (218). In both simulations, temperature, pressure, timestep, cut-off (303 K, 1 bar, 2 fs and 10 Å, respectively) and the application of SHAKE algorithm were the same.

In both studies, QM/MM methodology was performed, however with different methodologies. In our model, we performed the calculations using B3LYP/6-31G(d,p):ff14SB, while they used 2D umbrella sampling (219) with SCC-DFTB semiempirical force fields (220).

The selection of the amino acid residues of the QM region is fundamental for the energetic calculation. In our system, we selected the MHET substrate, backboneless catalytic triad, oxyanion hole backbones, and a surrounding arginine (71 atoms in total). Meanwhile, the other group only selected the MHET substrate and the catalytic triad (46 atoms in total), neglecting the residues involved in the stabilization of the oxyanion hole. As for the deacylation process, we added a water molecule, making a total of 74 atoms. Meanwhile, the other group fully removed the EG product and added the water molecule in its place, making a total of 39 atoms. Furthermore, the charge of our model was set to be -1 in the HH layer, while in their work the QM area charge was set to be -2. This difference is resulted due to the presence of an arginine in the QM region of our work.

The energetic calculations revealed by the group only relates to the overall acylation and deacylation activation and reaction energies. The acylation step calculations determined a free Gibbs energy of activation of  $13.9 \pm 0.17$  kcal/mol and an exergonic reaction, with the free Gibbs energy of reaction being  $-5.2 \pm 0.04$  kcal/mol. Our calculation of the free Gibbs energy for the acylation step resulted in a  $\Delta G^\ddagger$  of 8.84 kcal/mol, which is significantly lower when compared to the ones obtained by the group. This dissimilarity may be due to the different methodologies used throughout both studies. Comparisons between the results of the deacylation step cannot be done due to the lack of results of the step 4.



## **D. Conclusion and Future Works**

Synthetic polymers have been massively over-produced in the last decades. The combination of properties such as durability, low-cost, non-degradability, and capability of being moulded when pressure and heat are applied contributes to the high plastic demand. However, due to these factors and the non-degradability efficiency by the plastic degradation industry several hazard problems are being caused by plastic such as, marine, freshwater and atmosphere pollution, human health diseases, and overall negative impact in ecosystems, which can be potentially lethal for living beings.

Currently, the plastic degradation industry methods require high pressure and temperature, and often organic solvents, causing additional environmental pollutants. Therefore, it is necessary to develop a greener strategy. One of the solutions is the degradation of plastic by biocatalysts, such as enzymes.

PET polymer is by far the biggest target for biodegradation studies and currently several enzymes have been reported to have the ability to degrade the polymer. The catalytic reaction of this synthetic polymer with biocatalysts often leads to the production of the intermediates MHET and BHET and the building blocks TPA and EG. However, studies regarding the catalytic mechanism of MHET reaction are scarce. Therefore, in this work we provide a better insight of the catalytic mechanism of *h*MHETase towards MHET as well as the energies involved in each step using theoretical and computational means.

Based on the obtained results we suggest that the catalytic mechanism occurs in five sequential steps that are divided into acylation and deacylation, where the acylation process occurs in three steps and the deacylation in two.

The first step is initiated when Ser225 is deprotonated by His528, which enhances the nucleophilic character of Ser225 and attacks the carbonyl carbon of MHET. A simultaneous hydrogen transfer is observed between His528 and Asp492. The step resulted in an activation energy of 6.44 kcal/mol and an exergonic reaction of -1.75 kcal/mol.

In the second step the breaking of MHET substrate C $\alpha$ -C bond and consequently production of EG is observed and resulted in an activation energy of 8,84 kcal/mol and an endergonic reaction of 7,73 kcal/mol.

Step three is the final step of the acylation process that results in the transference of a proton to the negatively charged oxygen of EG. After the single point calculation, we obtained an activation energy of -1.12 kcal/mol and an exergonic reaction of -6.80 kcal/mol. We believe that the negative result of the activation energy suggests a spontaneous step triggered by the entropic contribution.

Step four marks the start of the deacylation process where a water molecule is introduced in the previous space where the EG block was. This water molecule makes a nucleophilic attack to the acyl-enzyme intermediate. Due to problems with microinteractions on the optimizations of the TS we were unable to obtain the energy barrier values. However, work is still undergoing.

Finally, step five marks the end of the catalytic mechanism where the catalytic triad is regenerated and the second product, TPA, is released. Here, we obtained an activation energy of 8,74 kcal/mol and an endergonic reaction of 1,95 kcal/mol.

Future work will entail the calculation of activation and reaction energies of step 4. With this, we obtain all energies barriers involved in the catalytic mechanism and can conclude the study. Furthermore, in-site mutagenesis will be applied in order to investigate the impact of some mutants on the overall enzymatic efficiency.

## E. References

1. Amobonye A, Bhagwat P, Singh S, Pillai S. Plastic biodegradation: Frontline microbes and their enzymes. *Science of The Total Environment*. 2021 Mar;759:143536.
2. Plastics—The Facts 2020. Available online: <https://plasticseurope.org/knowledge-hub/> (accessed on 13 December 2021).
3. Geyer R, Jambeck JR, Law KL. Production, use, and fate of all plastics ever made. *Science Advances*. 2017 Jul 5;3(7).
4. Zalasiewicz J, Waters CN, Ivar do Sul JA, Corcoran PL, Barnosky AD, Cearreta A, et al. The geological cycle of plastics and their use as a stratigraphic indicator of the Anthropocene. *Anthropocene*. 2016 Mar;13:4–17.
5. Yonan Y. Plastics—The Facts 2021. Available online: <https://plasticseurope.org/knowledge-hub/> (accessed on 22 December 2021).
6. Nguyen HTH, Qi P, Rostagno M, Feteha A, Miller SA. The quest for high glass transition temperature bioplastics. *Journal of Materials Chemistry A*. 2018;6(20):9298–331.
7. Carr CM, Clarke DJ, Dobson ADW. Microbial Polyethylene Terephthalate Hydrolases: Current and Future Perspectives. *Frontiers in Microbiology*. 2020 Nov 11;11.
8. Nowlin TE. *Business and Technology of the Global Polyethylene Industry*. Hoboken, NJ, USA: John Wiley & Sons, Inc.; 2014.
9. Jambeck JR, Geyer R, Wilcox C, Siegler TR, Perryman M, Andrady A, et al. Plastic waste inputs from land into the ocean. *Science*. 2015 Feb 13;347(6223):768–71.
10. Awuchi C, Awuchi C. Physiological Effects of Plastic Wastes on the Endocrine System (Bisphenol A, Phthalates, Bisphenol S, PBDEs, TBBPA). *International Journal of Bioinformatics and Computational Biology*. 2019 Dec 21;4:11–29.
11. Lyche JL, Gutleb AC, Bergman Å, Eriksen GS, Murk AJ, Ropstad E, et al. Reproductive and Developmental Toxicity of Phthalates. *Journal of Toxicology and Environmental Health, Part B*. 2009 Aug 28;12(4):225–49.
12. Jurewicz J, Hanke W. Exposure to phthalates: Reproductive outcome and children health. A review of epidemiological studies. *International Journal of Occupational Medicine and Environmental Health*. 2011 Jan 1;24(2).
13. Pocar P, Brevini T, Fischer B, Gandolfi F. The impact of endocrine disruptors on oocyte competence. *Reproduction*. 2003 Mar 1;313–25.
14. Nicolopoulou-Stamati P. The impact of endocrine disruptors on the female reproductive system. *Human Reproduction Update*. 2001 May 1;7(3):323–30.
15. Windham GC, Lee D, Mitchell P, Anderson M, Petreas M, Lasley B. Exposure to Organochlorine Compounds and Effects on Ovarian Function. *Epidemiology*. 2005 Mar;16(2):182–90.
16. Toppari J, Skakkebaek NE. Sexual differentiation and environmental endocrine disruptors. *Baillière's Clinical Endocrinology and Metabolism*. 1998 Apr;12(1):143–56.
17. Colon I, Caro D, Bourdony CJ, Rosario O. Identification of Phthalate Esters in the Serum of Young Puerto Rican Girls with Premature Breast Development. *Environ Health Perspect*. 2000 Aug;108:895–900.

18. Aksglaede L, Juul A, Leffers H, Skakkebaek NE, Andersson A-M. The sensitivity of the child to sex steroids: possible impact of exogenous estrogens. *Human Reproduction Update*. 2006 Aug 1;12(4):341–9.
19. Swan SH, Main KM, Liu F, Stewart SL, Kruse RL, Calafat AM, et al. Decrease in Anogenital Distance among Male Infants with Prenatal Phthalate Exposure. *Environmental Health Perspectives*. 2005 Aug;113(8):1056–61.
20. Montuori P, Jover E, Morgantini M, Bayona JM, Triassi M. Assessing human exposure to phthalic acid and phthalate esters from mineral water stored in polyethylene terephthalate and glass bottles. *Food Additives & Contaminants: Part A*. 2008 Apr;25(4):511–8.
21. Sax L. Polyethylene Terephthalate May Yield Endocrine Disruptors. *Environmental Health Perspectives*. 2010 Apr;118(4):445–8.
22. Pan G, Hanaoka T, Yoshimura M, Zhang S, Wang P, Tsukino H, et al. Decreased Serum Free Testosterone in Workers Exposed to High Levels of Di- *n*-butyl Phthalate (DBP) and Di-2-ethylhexyl Phthalate (DEHP): A Cross-Sectional Study in China. *Environmental Health Perspectives*. 2006 Nov;114(11):1643–8.
23. Dockery DW, Pope CA, Xu X, Spengler JD, Ware JH, Fay ME, et al. An Association between Air Pollution and Mortality in Six U.S. Cities. *New England Journal of Medicine*. 1993 Dec 9;329(24):1753–9.
24. Prata JC. Airborne microplastics: Consequences to human health? *Environmental Pollution*. 2018 Mar;234:115–26.
25. Song Y, Li X, Du X. Exposure to nanoparticles is related to pleural effusion, pulmonary fibrosis and granuloma. *European Respiratory Journal*. 2009 Sep 1;34(3):559–67.
26. Giulivo M, Lopez de Alda M, Capri E, Barceló D. Human exposure to endocrine disrupting compounds: Their role in reproductive systems, metabolic syndrome and breast cancer. A review. *Environmental Research*. 2016 Nov;151:251–64.
27. Factor-Litvak P, Insel B, Calafat AM, Liu X, Perera F, Rauh VA, et al. Persistent Associations between Maternal Prenatal Exposure to Phthalates on Child IQ at Age 7 Years. *PLoS ONE*. 2014 Dec 10;9(12):e114003.
28. Balalian AA, Whyatt RM, Liu X, Insel BJ, Rauh VA, Herbstman J, et al. Prenatal and childhood exposure to phthalates and motor skills at age 11 years. *Environmental Research*. 2019 Apr;171:416–27.
29. Waring RH, Harris RM, Mitchell SC. Plastic contamination of the food chain: A threat to human health? *Maturitas*. 2018 Sep;115:64–8.
30. Pazos RS, Maiztegui T, Colautti DC, Paracampo AH, Gómez N. Microplastics in gut contents of coastal freshwater fish from Río de la Plata estuary. *Marine Pollution Bulletin*. 2017 Sep;122(1–2):85–90.
31. McGoran AR, Clark PF, Morrill D. Presence of microplastic in the digestive tracts of European flounder, *Platichthys flesus*, and European smelt, *Osmerus eperlanus*, from the River Thames. *Environmental Pollution*. 2017 Jan;220:744–51.

32. van Cauwenberghe L, Janssen CR. Microplastics in bivalves cultured for human consumption. *Environmental Pollution*. 2014 Oct;193:65–70.
33. Vandermeersch G, Lourenço HM, Alvarez-Muñoz D, Cunha S, Diogène J, Cano-Sancho G, et al. Environmental contaminants of emerging concern in seafood – European database on contaminant levels. *Environmental Research*. 2015 Nov;143:29–45.
34. Hahladakis JN, Velis CA, Weber R, Iacovidou E, Purnell P. An overview of chemical additives present in plastics: Migration, release, fate and environmental impact during their use, disposal and recycling. *Journal of Hazardous Materials*. 2018 Feb;344:179–99.
35. Marshall I, Todd A. The thermal degradation of polyethylene terephthalate. *Transaction of the Faraday Society*. 1952 May;49:67-78
36. S. Subramanian, Plastic Roads: India's Radical Plan to Bury Its Garbage Beneath the Streets, 2016, Available online: <https://www.theguardian.com/sustainable-business/2016/jun/30/plastic-road-india-tar-plastic-transportenvironment-pollution-waste> (accessed on 25 september 2021).
37. Yoshida S, Hiraga K, Takehana T, Taniguchi I, Yamaji H, Maeda Y, et al. A bacterium that degrades and assimilates poly(ethylene terephthalate). *Science*. 2016 Mar 11;351(6278):1196–9.
38. Austin HP, Allen MD, Donohoe BS, Rorrer NA, Kearns FL, Silveira RL, et al. Characterization and engineering of a plastic-degrading aromatic polyesterase. *Proceedings of the National Academy of Sciences*. 2018 May 8;115(19):E4350–7.
39. Joo S, Cho IJ, Seo H, Son HF, Sagong H-Y, Shin TJ, et al. Structural insight into molecular mechanism of poly(ethylene terephthalate) degradation. *Nature Communications*. 2018 Dec 26;9(1):382.
40. Han X, Liu W, Huang J-W, Ma J, Zheng Y, Ko T-P, et al. Structural insight into catalytic mechanism of PET hydrolase. *Nature Communications*. 2017 Dec 13;8(1):2106.
41. Liu B, He L, Wang L, Li T, Li C, Liu H, et al. Protein Crystallography and Site-Direct Mutagenesis Analysis of the Poly(ethylene terephthalate) Hydrolase PETase from *Ideonella sakaiensis*. *ChemBioChem*. 2018 Jul 16;19(14):1471–5.
42. Berman, H.M.; Westbrook, J.; Feng, Z.; Gilliland, G.; Bhat, T.N.; Weissig, H.; Shindyalov, I.N.; Bourne, P.E. The Protein Data Bank. Available online: [rcsb.org](http://rcsb.org) (accessed on 17 September 2021).
43. Son HF, Cho IJ, Joo S, Seo H, Sagong H-Y, Choi SY, et al. Rational Protein Engineering of Thermo-Stable PETase from *Ideonella sakaiensis* for Highly Efficient PET Degradation. *ACS Catalysis*. 2019 Apr 5;9(4):3519–26.
44. Weiland MH. Enzymatic Biodegradation by Exploring the Rational Protein Engineering of the Polyethylene Terephthalate Hydrolyzing Enzyme PETase from *Ideonella sakaiensis* 201-F6. In 2020. p. 161–74.
45. Son HF, Joo S, Seo H, Sagong H-Y, Lee SH, Hong H, et al. Structural bioinformatics-based protein engineering of thermo-stable PETase from *Ideonella sakaiensis*. *Enzyme and Microbial Technology*. 2020 Nov;141:109656.

46. Cui, Y.; Chen, Y.; Liu, X.; Dong, S.; Tian, Y.; Qiao, Y.; Mitra, R.; Han, J.; Li, C.; Han, X.; et al. Computational Redesign of a PETase for Plastic Biodegradation by the GRAPE Strategy. *bioRxiv* 2019, 787069.
47. Sun J, Cui Y, Wu B. GRAPE, a greedy accumulated strategy for computational protein engineering. 2021. 648:207–30.
48. Chen Z, Wang Y, Cheng Y, Wang X, Tong S, Yang H, et al. Efficient biodegradation of highly crystallized polyethylene terephthalate through cell surface display of bacterial PETase. *Science of The Total Environment*. 2020 Mar;709:136138.
49. Moog D, Schmitt J, Senger J, Zarzycki J, Rexer K-H, Linne U, et al. Using a marine microalga as a chassis for polyethylene terephthalate (PET) degradation. *Microbial Cell Factories*. 2019 Dec 10;18(1):171.
50. Kim JW, Park S-B, Tran Q-G, Cho D-H, Choi D-Y, Lee YJ, et al. Functional expression of polyethylene terephthalate-degrading enzyme (PETase) in green microalgae. *Microbial Cell Factories*. 2020 Dec 28;19(1):97.
51. Cousin X, Hotelier T, Giles K, Lievin P, Toutant J-P, Chatonnet A. The / fold family of proteins database and the cholinesterase gene server ESTHER. *Nucleic Acids Research*. 1997 Jan 1;25(1):143–6.
52. Sagong H-Y, Seo H, Kim T, Son HF, Joo S, Lee SH, et al. Decomposition of the PET Film by MHETase Using Exo-PETase Function. *ACS Catalysis*. 2020 Apr 17;10(8):4805–12.
53. Suzuki K, Hori A, Kawamoto K, Thangudu RR, Ishida T, Igarashi K, et al. Crystal structure of a feruloyl esterase belonging to the tannase family: A disulfide bond near a catalytic triad. *Proteins: Structure, Function, and Bioinformatics*. 2014 Oct;82(10):2857–67.
54. Knott BC, Erickson E, Allen MD, Gado JE, Graham R, Kearns FL, et al. Characterization and engineering of a two-enzyme system for plastics depolymerization. *Proceedings of the National Academy of Sciences*. 2020 Oct 13;117(41):25476–85.
55. Palm GJ, Reisky L, Böttcher D, Müller H, Michels EAP, Walczak MC, et al. Structure of the plastic-degrading *Ideonella sakaiensis* MHETase bound to a substrate. *Nature Communications*. 2019 Dec 12;10(1):1717.
56. Bollinger A, Thies S, Knieps-Grünhagen E, Gertzen C, Kobus S, Höppner A, et al. A Novel Polyester Hydrolase From the Marine Bacterium *Pseudomonas aestusnigri* – Structural and Functional Insights. *Frontiers in Microbiology*. 2020 Feb 13;11.
57. Sánchez D, Mulet M, Rodríguez AC, David Z, Lalucat J, García-Valdés E. *Pseudomonas aestusnigri* sp. nov., isolated from crude oil-contaminated intertidal sand samples after the Prestige oil spill. *Systematic and Applied Microbiology*. 2014 Mar;37(2):89–94.
58. Gomila M, Mulet M, Lalucat J, García-Valdés E. Draft Genome Sequence of the Marine Bacterium *Pseudomonas aestusnigri* VGX014<sup>T</sup>. *Genome Announcements*. 2017 Aug 10;5(32).
59. Bollinger A, Thies S, Katzke N, Jaeger K. The biotechnological potential of marine bacteria in the novel lineage of *Pseudomonas pertucinogena*. *Microbial Biotechnology*. 2020 Jan;13(1):19–31.



60. Sulaiman S, Yamato S, Kanaya E, Kim J-J, Koga Y, Takano K, et al. Isolation of a Novel Cutinase Homolog with Polyethylene Terephthalate-Degrading Activity from Leaf-Branch Compost by Using a Metagenomic Approach. *Applied and Environmental Microbiology*. 2012 Mar;78(5):1556–62.
61. Sulaiman S, You D-J, Kanaya E, Koga Y, Kanaya S. Crystal Structure and Thermodynamic and Kinetic Stability of Metagenome-Derived LC-Cutinase. *Biochemistry*. 2014 Mar 25;53(11):1858–69.
62. Tournier V, Topham CM, Gilles A, David B, Folgoas C, Moya-Leclair E, et al. An engineered PET depolymerase to break down and recycle plastic bottles. *Nature*. 2020 Apr 9;580(7802):216–9.
63. Yan F, Wei R, Cui Q, Bornscheuer UT, Liu Y. Thermophilic whole-cell degradation of polyethylene terephthalate using engineered *Clostridium thermocellum*. *Microbial Biotechnology*. 2021 Mar 28;14(2):374–85.
64. Kleeberg I, Hetz C, Kroppenstedt RM, Müller R-J, Deckwer W-D. Biodegradation of Aliphatic-Aromatic Copolyesters by *Thermomonospora fusca* and Other Thermophilic Compost Isolates. *Applied and Environmental Microbiology*. 1998 May;64(5):1731–5.
65. Chen S, Tong X, Woodard RW, Du G, Wu J, Chen J. Identification and Characterization of Bacterial Cutinase. *Journal of Biological Chemistry*. 2008 Sep;283(38):25854–62.
66. Dresler K, van den Heuvel J, Müller R-J, Deckwer W-D. Production of a recombinant polyester-cleaving hydrolase from *Thermobifida fusca* in *Escherichia coli*. *Bioprocess and Biosystems Engineering*. 2006 Aug 13;29(3):169–83.
67. Müller R-J, Schrader H, Profe J, Dresler K, Deckwer W-D. Enzymatic Degradation of Poly(ethylene terephthalate): Rapid Hydrolyse using a Hydrolase from *T. fusca*. *Macromolecular Rapid Communications*. 2005 Sep 5;26(17):1400–5.
68. Kleeberg I, Welzel K, VandenHeuvel J, Müller R-J, Deckwer W-D. Characterization of a New Extracellular Hydrolase from *Thermobifida fusca* Degrading Aliphatic–Aromatic Copolyesters. *Biomacromolecules*. 2005 Jan 1;6(1):262–70.
69. Silva C, Da S, Silva N, Matamá T, Araújo R, Martins M, et al. Engineered *Thermobifida fusca* cutinase with increased activity on polyester substrates. *Biotechnology Journal*. 2011 Oct;6(10):1230–9.
70. Dong Q, Yuan S, Wu L, Su L, Zhao Q, Wu J, et al. Structure-guided engineering of a *Thermobifida fusca* cutinase for enhanced hydrolysis on natural polyester substrate. *Bioresources and Bioprocessing*. 2020 Dec 9;7(1):37.
71. Then J, Wei R, Oeser T, Barth M, Belisário-Ferrari MR, Schmidt J, et al. Ca<sup>2+</sup> and Mg<sup>2+</sup> binding site engineering increases the degradation of polyethylene terephthalate films by polyester hydrolases from *Thermobifida fusca*. *Biotechnology Journal*. 2015 Apr;10(4):592–8.
72. Alisch-Mark M, Herrmann A, Zimmermann W. Increase of the Hydrophilicity of Polyethylene Terephthalate Fibres by Hydrolases from *Thermomonospora fusca* and *Fusarium solani* f. sp. *pisii*. *Biotechnology Letters*. 2006 May 23;28(10):681–5.
73. Su L, Woodard RW, Chen J, Wu J. Extracellular Location of *Thermobifida fusca* Cutinase Expressed in *Escherichia coli* BL21(DE3) without Mediation of a Signal Peptide. *Applied and Environmental Microbiology*. 2013 Jul 15;79(14):4192–8.

74. Yang Y, Malten M, Grote A, Jahn D, Deckwer W-D. Codon optimized *Thermobifida fusca* hydrolase secreted by *Bacillus megaterium*. *Biotechnology and Bioengineering*. 2007 Mar 1;96(4):780–94.
75. Sinsereekul N, Wangkam T, Thamchaipenet A, Srihirin T, Eurwilaichitr L, Champreda V. Recombinant expression of BTA hydrolase in *Streptomyces rimosus* and catalytic analysis on polyesters by surface plasmon resonance. *Applied Microbiology and Biotechnology*. 2010 May 20;86(6):1775–84.
76. Kawai F, Oda M, Tamashiro T, Waku T, Tanaka N, Yamamoto M, et al. A novel Ca<sup>2+</sup>-activated, thermostabilized polyesterase capable of hydrolyzing polyethylene terephthalate from *Saccharomonospora viridis* AHK190. *Applied Microbiology and Biotechnology*. 2014 Dec 15;98(24):10053–64.
77. Pati A, Sikorski J, Nolan M, Lapidus A, Copeland A, Glavina Del Rio T, et al. Complete genome sequence of *Saccharomonospora viridis* type strain (P101T). *Standards in Genomic Sciences*. 2009 Sep 24;1(2):141–9.
78. Miyakawa T, Mizushima H, Ohtsuka J, Oda M, Kawai F, Tanokura M. Structural basis for the Ca<sup>2+</sup>-enhanced thermostability and activity of PET-degrading cutinase-like enzyme from *Saccharomonospora viridis* AHK190. *Applied Microbiology and Biotechnology*. 2015 May 11;99(10):4297–307.
79. Numoto N, Kamiya N, Bekker G-J, Yamagami Y, Inaba S, Ishii K, et al. Structural Dynamics of the PET-Degrading Cutinase-like Enzyme from *Saccharomonospora viridis* AHK190 in Substrate-Bound States Elucidates the Ca<sup>2+</sup>-Driven Catalytic Cycle. *Biochemistry*. 2018 Sep 11;57(36):5289–300.
80. Oda M, Yamagami Y, Inaba S, Oida T, Yamamoto M, Kitajima S, et al. Enzymatic hydrolysis of PET: functional roles of three Ca<sup>2+</sup> ions bound to a cutinase-like enzyme, Cut190\*, and its engineering for improved activity. *Applied Microbiology and Biotechnology*. 2018 Dec 24;102(23):10067–77.
81. Kawabata T, Oda M, Kawai F. Mutational analysis of cutinase-like enzyme, Cut190, based on the 3D docking structure with model compounds of polyethylene terephthalate. *Journal of Bioscience and Bioengineering*. 2017 Jul;124(1):28–35.
82. Senga A, Numoto N, Yamashita M, Iida A, Ito N, Kawai F, et al. Multiple structural states of Ca<sup>2+</sup>-regulated PET hydrolase, Cut190, and its correlation with activity and stability. *The Journal of Biochemistry*. 2021 Mar 5;169(2):207–13.
83. Ribitsch D, Acero EH, Greimel K, Eiteljoerg I, Trotscha E, Freddi G, et al. Characterization of a new cutinase from *Thermobifida alba* for PET-surface hydrolysis. *Biocatalysis and Biotransformation*. 2012 Feb 14;30(1):2–9.
84. Herrero Acero E, Ribitsch D, Steinkellner G, Gruber K, Greimel K, Eiteljoerg I, et al. Enzymatic Surface Hydrolysis of PET: Effect of Structural Diversity on Kinetic Properties of Cutinases from *Thermobifida*. *Macromolecules*. 2011 Jun 28;44(12):4632–40.
85. Roth C, Wei R, Oeser T, Then J, Föllner C, Zimmermann W, et al. Structural and functional studies on a thermostable polyethylene terephthalate degrading hydrolase from *Thermobifida fusca*. *Applied Microbiology and Biotechnology*. 2014 Sep 13;98(18):7815–23.

86. Ribitsch D, Hromic A, Zitzenbacher S, Zartl B, Gamerith C, Pellis A, et al. Small cause, large effect: Structural characterization of cutinases from *Thermobifida cellulosilytica*. *Biotechnology and Bioengineering*. 2017 Nov;114(11):2481–8.
87. Gamerith C, Zartl B, Pellis A, Guillaumot F, Marty A, Acero EH, et al. Enzymatic recovery of polyester building blocks from polymer blends. *Process Biochemistry*. 2017 Aug;59:58–64.
88. Barth M, Oeser T, Wei R, Then J, Schmidt J, Zimmermann W. Effect of hydrolysis products on the enzymatic degradation of polyethylene terephthalate nanoparticles by a polyester hydrolase from *Thermobifida fusca*. *Biochemical Engineering Journal*. 2015 Jan;93:222–8.
89. Wei R, Oeser T, Schmidt J, Meier R, Barth M, Then J, et al. Engineered bacterial polyester hydrolases efficiently degrade polyethylene terephthalate due to relieved product inhibition. *Biotechnology and Bioengineering*. 2016 Aug;113(8):1658–65.
90. Barth M, Wei R, Oeser T, Then J, Schmidt J, Wohlgemuth F, et al. Enzymatic hydrolysis of polyethylene terephthalate films in an ultrafiltration membrane reactor. *Journal of Membrane Science*. 2015 Nov;494:182–7.
91. Then J, Wei R, Oeser T, Gerdts A, Schmidt J, Barth M, et al. A disulfide bridge in the calcium binding site of a polyester hydrolase increases its thermal stability and activity against polyethylene terephthalate. *FEBS Open Bio*. 2016 May;6(5):425–32.
92. Herrero Acero E, Ribitsch D, Dellacher A, Zitzenbacher S, Marold A, Steinkellner G, et al. Surface engineering of a cutinase from *Thermobifida cellulosilytica* for improved polyester hydrolysis. *Biotechnology and Bioengineering*. 2013 Oct;110(10):2581–90.
93. Dimarogona M, Nikolaivits E, Kanelli M, Christakopoulos P, Sandgren M, Topakas E. Structural and functional studies of a *Fusarium oxysporum* cutinase with polyethylene terephthalate modification potential. *Biochimica et Biophysica Acta (BBA) - General Subjects*. 2015 Nov;1850(11):2308–17.
94. Gott K, Burgess L, Balmas V, Duff J. Mycogeography of *Fusarium*: *Fusarium* Species in Soils From Palm Valley, Central Australia. *Australasian Plant Pathology*. 1994;23(3):112.
95. Nikolaivits E, Kokkinou A, Karpusas M, Topakas E. Microbial host selection and periplasmic folding in *Escherichia coli* affect the biochemical characteristics of a cutinase from *Fusarium oxysporum*. *Protein Expression and Purification*. 2016 Nov;127:1–7.
96. Kanelli M, Vasilakos S, Nikolaivits E, Ladas S, Christakopoulos P, Topakas E. Surface modification of poly(ethylene terephthalate) (PET) fibers by a cutinase from *Fusarium oxysporum*. *Process Biochemistry*. 2015 Nov;50(11):1885–92.
97. Maheshwari R, Bharadwaj G, Bhat MK. Thermophilic Fungi: Their Physiology and Enzymes. *Microbiology and Molecular Biology Reviews*. 2000 Sep;64(3):461–88.
98. Ronkvist ÅM, Xie W, Lu W, Gross RA. Cutinase-Catalyzed Hydrolysis of Poly(ethylene terephthalate). *Macromolecules*. 2009 Jul 28;42(14):5128–38.
99. Kold D, Dauter Z, Laustsen AK, Brzozowski AM, Turkenburg JP, Nielsen AD, et al. Thermodynamic and structural investigation of the specific SDS binding of *Humicola insolens* cutinase. *Protein Science*. 2014 Aug;23(8):1023–35.

100. Kazenwadel C, Eiben S, Maurer S, Beuttler H, Wetzl D, Hauer B, et al. Thiol-functionalization of acrylic ester monomers catalyzed by immobilized *Humicola insolens* cutinase. *Enzyme and Microbial Technology*. 2012 Jun;51(1):9–15.
101. Bateman A, Martin M-J, Orchard S, Magrane M, Agivetova R, Ahmad S, et al. UniProt: the universal protein knowledgebase in 2021. *Nucleic Acids Research*. 2021 Jan 8;49(D1):D480–9.
102. Fabbri F, Bertolini FA, Guebitz GM, Pellis A. Biocatalyzed Synthesis of Flavor Esters and Polyesters: A Design of Experiments (DoE) Approach. *International Journal of Molecular Sciences*. 2021 Aug 6;22(16):8493.
103. Feder D, Gross RA. Exploring Chain Length Selectivity in HIC-Catalyzed Polycondensation Reactions. *Biomacromolecules*. 2010 Mar 8;11(3):690–7.
104. de Castro AM, Carniel A, Nicomedes Junior J, da Conceição Gomes A, Valoni É. Screening of commercial enzymes for poly(ethylene terephthalate) (PET) hydrolysis and synergy studies on different substrate sources. *Journal of Industrial Microbiology and Biotechnology*. 2017 Jun 1;44(6):835–44.
105. Carniel A, Valoni É, Nicomedes J, Gomes A da C, Castro AM de. Lipase from *Candida antarctica* (CALB) and cutinase from *Humicola insolens* act synergistically for PET hydrolysis to terephthalic acid. *Process Biochemistry*. 2017 Aug;59:84–90.
106. Quartinello F, Vajnhandl S, Volmajer Valh J, Farmer TJ, Vončina B, Lobnik A, et al. Synergistic chemo-enzymatic hydrolysis of poly(ethylene terephthalate) from textile waste. *Microbial Biotechnology*. 2017 Nov 2;10(6):1376–83.
107. Carniel A, Gomes A da C, Coelho MAZ, de Castro AM. Process strategies to improve biocatalytic depolymerization of post-consumer PET packages in bioreactors, and investigation on consumables cost reduction. *Bioprocess and Biosystems Engineering*. 2021 Mar 28;44(3):507–16.
108. Eugenio E de Q, Campisano ISP, Castro AM de, Coelho MAZ, Langone MAP. Experimental and mathematical modeling approaches for biocatalytic post-consumer poly(ethylene terephthalate) hydrolysis. *Journal of Biotechnology*. 2021 Nov;341:76–85.
109. Lin T-S, Kolattukudy PE. Structural Studies on Cutinase, a Glycoprotein Containing Novel Amino Acids and Glucuronic Acid Amide at the N Terminus. *European Journal of Biochemistry*. 1980 May;106(2):341–51.
110. Martinez C, de Geus P, Lauwereys M, Matthyssens G, Cambillau C. *Fusarium solani* cutinase is a lipolytic enzyme with a catalytic serine accessible to solvent. *Nature*. 1992 Apr;356(6370):615–8.
111. Summerell BA, Laurence MH, Liew ECY, Leslie JF. Biogeography and phylogeography of *Fusarium*: a review. *Fungal Diversity*. 2010 Oct 14;44(1):3–13.
112. Martinez C, Nicolas A, van Tilbeurgh H, Egloff MP, Cudrey C, Verger R, et al. Cutinase, a lipolytic enzyme with a preformed oxyanion hole. *Biochemistry*. 1994 Jan 11;33(1):83–9.
113. Nicolas A, Egmond M, Verrips CT, de Vlieg J, Longhi S, Cambillau C, et al. Contribution of Cutinase Serine 42 Side Chain to the Stabilization of the Oxyanion Transition State †‡. *Biochemistry*. 1996 Jan 1;35(2):398–410.

114. Heumann S, Eberl A, Pobeheim H, Liebminger S, Fischer-Colbrie G, Almansa E, et al. New model substrates for enzymes hydrolysing polyethyleneterephthalate and polyamide fibres. *Journal of Biochemical and Biophysical Methods*. 2006 Nov;69(1–2):89–99.
115. Araújo R, Silva C, O’Neill A, Micaelo N, Guebitz G, Soares CM, et al. Tailoring cutinase activity towards polyethylene terephthalate and polyamide 6,6 fibers. *Journal of Biotechnology*. 2007 Mar;128(4):849–57.
116. Goto S, Sugiyama J, Iizuka H. A Taxonomic Study of Antarctic Yeasts. *Mycologia*. 1969 Jul;61(4):748.
117. Heldt-Hansen HP, Ishii M, Patkar SA, Hansen TT, Eigtd P. A New Immobilized Positional Nonspecific Lipase for Fat Modification and Ester Synthesis. *American Chemical Society*. 1989; 389:158–72.
118. Strzelczyk P, Bujacz GD, Kiełbasiński P, Błaszczuk J. Crystal and molecular structure of hexagonal form of lipase B from *Candida antarctica*. *Acta Biochimica Polonica*. 2015 Dec 30;63(1).
119. Uppenberg J, Oehrner N, Norin M, Hult K, Kleywegt GJ, Patkar S, et al. Crystallographic and molecular-modeling studies of lipase B from *Candida antarctica* reveal a stereospecificity pocket for secondary alcohols. *Biochemistry*. 1995 Dec 1;34(51):16838–51.
120. Anderson EM, Larsson KM, Kirk O. One Biocatalyst–Many Applications: The Use of *Candida antarctica* B-Lipase in Organic Synthesis. *Biocatalysis and Biotransformation*. 1998 Jan 11;16(3):181–204.
121. Stauch B, Fisher SJ, Cianci M. Open and closed states of *Candida antarctica* lipase B: protonation and the mechanism of interfacial activation. *Journal of Lipid Research*. 2015 Dec;56(12):2348–58.
122. Uppenberg J, Hansen MT, Patkar S, Jones TA. The sequence, crystal structure determination and refinement of two crystal forms of lipase B from *Candida antarctica*. *Structure*. 1994 Apr;2(4):293–308.
123. Xu J, Cen Y, Singh W, Fan J, Wu L, Lin X, et al. Stereodivergent Protein Engineering of a Lipase To Access All Possible Stereoisomers of Chiral Esters with Two Stereocenters. *Journal of the American Chemical Society*. 2019 May 15;141(19):7934–45.
124. Hong SY, Yoo YJ. Activity Enhancement of *Candida antarctica* Lipase B by Flexibility Modulation in Helix Region Surrounding the Active Site. *Applied Biochemistry and Biotechnology*. 2013 Jun 28;170(4):925–33.
125. Park HJ, Park K, Kim YH, Yoo YJ. Computational approach for designing thermostable *Candida antarctica* lipase B by molecular dynamics simulation. *Journal of Biotechnology*. 2014 Dec;192:66–70.
126. Le QAT, Joo JC, Yoo YJ, Kim YH. Development of thermostable *Candida antarctica* lipase B through novel in silico design of disulfide bridge. *Biotechnology and Bioengineering*. 2012 Apr;109(4):867–76.
127. Suen W-C, Zhang N, Xiao L, Madison V, Zaks A. Improved activity and thermostability of *Candida antarctica* lipase B by DNA family shuffling. *Protein Engineering Design and Selection*. 2004 Jan 20;17(2):133–40.

128. Zhang N, Suen W-C, Windsor W, Xiao L, Madison V, Zaks A. Improving tolerance of *Candida antarctica* lipase B towards irreversible thermal inactivation through directed evolution. *Protein Engineering Design and Selection*. 2003 Aug 1;16(8):599–605.
129. Rotticci D, Rotticci-Mulder JC, Denman S, Norin T, Hult K. Improved Enantioselectivity of a Lipase by Rational Protein Engineering. *ChemBioChem*. 2001 Oct 1;2(10):766.
130. Magnusson AO, Rotticci-Mulder JC, Santagostino A, Hult K. Creating Space for Large Secondary Alcohols by Rational Redesign of *Candida antarctica* Lipase B. *ChemBioChem*. 2005 Jun 6;6(6):1051–6.
131. Tsiklinsky, P. Sur Les Mucedinees Thermophiles. *Ann. Inst. Pasteur* 1899, 13:501–505.
132. Chew YH, Chua LS, Cheng KK, Sarmidi MR, Aziz RA, Lee CT. Kinetic study on the hydrolysis of palm olein using immobilized lipase. *Biochemical Engineering Journal*. 2008 May;39(3):516–20.
133. Tangkam K, Weber N, Wiege B. Solvent-free lipase-catalyzed preparation of diglycerides from co-products of vegetable oil refining. *Grasas y Aceites*. 2008 Sep 30;59(3).
134. Sivalingam G, Chattopadhyay S, Madras G. Solvent effects on the lipase catalyzed biodegradation of poly ( $\epsilon$ -caprolactone) in solution. *Polymer Degradation and Stability*. 2003 Mar;79(3):413–8.
135. Reddy JRC, Vijeeta T, Karuna MSL, Rao BVSK, Prasad RBN. Lipase-catalyzed preparation of palmitic and stearic acid-rich phosphatidylcholine. *Journal of the American Oil Chemists' Society*. 2005 Oct;82(10):727–30.
136. Brueckner T, Eberl A, Heumann S, Rabe M, Guebitz GM. Enzymatic and chemical hydrolysis of poly(ethylene terephthalate) fabrics. *Journal of Polymer Science Part A: Polymer Chemistry*. 2008 Oct 1;46(19):6435–43.
137. Lawson DM, Brzozowski AM, Rety S, Verma C, Dodson GG. Probing the nature of substrate binding in *Humicola lanuginosa* lipase through x-ray crystallography and intuitive modelling. *Protein Engineering, Design and Selection*. 1994 Apr;7(4):543–50.
138. Derewenda U, Swenson L, Wei Y, Green R, Kobos PM, Joerger R, et al. Conformational lability of lipases observed in the absence of an oil- water interface: Crystallographic studies of enzymes from the fungi *Humicola lanuginosa* and *Rhizopus delemar*. *Journal of Lipid Research*. 1994;35(3):524–34.
139. Holmquist M, Clausen IG, Patkar S, Svendsen A, Hult K. Probing a functional role of Glu87 and Trp89 in the lid of *Humicola lanuginosa* lipase through transesterification reactions in organic solvent. *Journal of Protein Chemistry*. 1995 May;14(4):217–24.
140. Martinelle M, Holmquist M, Clausen IG, Patkar S, Svendsen A, Hult K. The role of Glu87 and Trp89 in the lid of *Humicola lanuginosa* lipase. "Protein Engineering, Design and Selection." 1996;9(6):519–24.
141. Holmquist M, Martinelle M, Clausen IG, Patkar S, Svendsen A, Hult K. Trp89 in the lid of *Humicola lanuginosa* lipase is important for efficient hydrolysis of tributyrin. *Lipids*. 1994 Sep;29(9):599–603.
142. Omar IC, Nishio N, Nagai S. Production of a thermostable lipase by *Humicola lanuginosa* grown on sorbitol-corn steep liquor medium. *Agricultural and Biological Chemistry*. 1987;51(8):2145–51.

143. Skjold-Jørgensen J, Vind J, Moroz O v., Blagova E, Bhatia VK, Svendsen A, et al. Controlled lid-opening in *Thermomyces lanuginosus* lipase– An engineered switch for studying lipase function. *Biochimica et Biophysica Acta (BBA) - Proteins and Proteomics*. 2017 Jan;1865(1):20–7.
144. Peters GH, Svendsen A, Langberg H, Vind J, Patkar SA, Toxvaerd S, et al. Active Serine Involved in the Stabilization of the Active Site Loop in the *Humicola lanuginosa* Lipase. *Biochemistry*. 1998 Sep 1;37(36):12375–83.
145. Eberl A, Heumann S, Brückner T, Araujo R, Cavaco-Paulo A, Kaufmann F, et al. Enzymatic surface hydrolysis of poly(ethylene terephthalate) and bis(benzoyloxyethyl) terephthalate by lipase and cutinase in the presence of surface active molecules. *Journal of Biotechnology*. 2009 Sep;143(3):207–12.
146. Hantani Y, Imamura H, Yamamoto T, Senga A, Yamagami Y, Kato M, et al. Functional characterizations of polyethylene terephthalate-degrading cutinase-like enzyme Cut190 mutants using bis(2-hydroxyethyl) terephthalate as the model substrate. *AIMS Biophysics*. 2018;5(4):290–302.
147. Oeser T, Wei R, Baumgarten T, Billig S, Föllner C, Zimmermann W. High level expression of a hydrophobic poly(ethylene terephthalate)-hydrolyzing carboxylesterase from *Thermobifida fusca* KW3 in *Escherichia coli* BL21(DE3). *Journal of Biotechnology*. 2010 Apr 1;146(3):100–4.
148. Billig S, Oeser T, Birkemeyer C, Zimmermann W. Hydrolysis of cyclic poly(ethylene terephthalate) trimers by a carboxylesterase from *Thermobifida fusca* KW3. *Applied Microbiology and Biotechnology*. 2010 Aug 14;87(5):1753–64.
149. Belisário-Ferrari MR, Wei R, Schneider T, Honak A, Zimmermann W. Fast Turbidimetric Assay for Analyzing the Enzymatic Hydrolysis of Polyethylene Terephthalate Model Substrates. *Biotechnology Journal*. 2019 Apr 21;14(4):1800272.
150. Barth M, Honak A, Oeser T, Wei R, Belisário-Ferrari MR, Then J, et al. A dual enzyme system composed of a polyester hydrolase and a carboxylesterase enhances the biocatalytic degradation of polyethylene terephthalate films. *Biotechnology Journal*. 2016 Aug;11(8):1082–7.
151. Kawai F, Thumarat U, Kitadokoro K, Waku T, Tada T, Tanaka N, et al. Comparison of Polyester-Degrading Cutinases from Genus *Thermobifida*. *Green Polymer Chemistry*. 2013; 1144:111–20.
152. Thumarat U, Kawabata T, Nakajima M, Nakajima H, Sugiyama A, Yazaki K, et al. Comparison of genetic structures and biochemical properties of tandem cutinase-type polyesterses from *Thermobifida alba* AHK119. *Journal of Bioscience and Bioengineering*. 2015 Nov;120(5):491–7.
153. Kitadokoro K, Matsui S, Osokoshi R, Nakata K, Kamitani S. Expression, Purification and Crystallization of Thermostable Mutant of Cutinase Est1 from *Thermobifida alba*. *Advances in Bioscience and Biotechnology*. 2018;09(05):215–23.
154. Qiu L, Yin X, Liu T, Zhang H, Chen G, Wu S. Biodegradation of bis(2-hydroxyethyl) terephthalate by a newly isolated *Enterobacter* sp. HY1 and characterization of its esterase properties. *Journal of Basic Microbiology*. 2020 Aug;60(8):699–711.
155. Xi X, Ni K, Hao H, Shang Y, Zhao B, Qian Z. Secretory expression in *Bacillus subtilis* and biochemical characterization of a highly thermostable polyethylene terephthalate hydrolase from bacterium HR29. *Enzyme and Microbial Technology*. 2021 Feb;143:109715.

156. Eggert T, Pencreac'h G, Douchet I, Verger R, Jaeger K-E. A novel extracellular esterase from *Bacillus subtilis* and its conversion to a monoacylglycerol hydrolase. *European Journal of Biochemistry*. 2000 Nov;267(21):6459–69.
157. Ribitsch D, Heumann S, Trotscha E, Herrero Acero E, Greimel K, Leber R, et al. Hydrolysis of polyethyleneterephthalate by p-nitrobenzylesterase from *Bacillus subtilis*. *Biotechnology Progress*. 2011 Jul;27(4):951–60.
158. Jabloun R, Khalil M, ben Moussa IE, Simao-Beauvoir A-M, Lerat S, Brzezinski R, et al. Enzymatic Degradation of *p*-Nitrophenyl Esters, Polyethylene Terephthalate, Cutin, and Suberin by Sub1, a Suberinase Encoded by the Plant Pathogen *Streptomyces scabies*. *Microbes and Environments*. 2020;35(1):n/a.
159. Lambert C, Leonard N, de Bolle X, Depiereux E. ESyPred3D: Prediction of proteins 3D structures. *Bioinformatics*. 2002 Aug 1;18(9):1250–6.
160. Yoon M-Y, Kellis J, Poulouse AJ. Enzymatic modification of polyester. *AATCC review*. 2002;2(6).
161. Danso D, Schmeisser C, Chow J, Zimmermann W, Wei R, Leggewie C, et al. New Insights into the Function and Global Distribution of Polyethylene Terephthalate (PET)-Degrading Bacteria and Enzymes in Marine and Terrestrial Metagenomes. *Applied and Environmental Microbiology*. 2018 Apr 15;84(8).
162. Wei R, Oeser T, Then J, Kühn N, Barth M, Schmidt J, et al. Functional characterization and structural modeling of synthetic polyester-degrading hydrolases from *Thermomonospora curvata*. *AMB Express*. 2014 Dec 3;4(1):44.
163. Ribitsch D, Herrero Acero E, Greimel K, Dellacher A, Zitzenbacher S, Marold A, et al. A New Esterase from *Thermobifida halotolerans* Hydrolyses Polyethylene Terephthalate (PET) and Polylactic Acid (PLA). *Polymers*. 2012 Feb 21;4(1):617–29.
164. Liebminger S, Eberl A, Sousa F, Heumann S, Fischer-Colbrie G, Cavaco-Paulo A, et al. Hydrolysis of PET and bis-(benzoyloxyethyl) terephthalate with a new polyesterase from *Penicillium citrinum*. *Biocatalysis and Biotransformation*. 2007 Jan 11;25(2–4):171–7.
165. da Costa AM, de Oliveira Lopes VR, Vidal L, Nicaud J-M, de Castro AM, Coelho MAZ. Poly(ethylene terephthalate) (PET) degradation by *Yarrowia lipolytica*: Investigations on cell growth, enzyme production and monomers consumption. *Process Biochemistry*. 2020 Aug;95:81–90.
166. Roberts C, Edwards S, Vague M, León-Zayas R, Scheffer H, Chan G, et al. Environmental Consortium Containing *Pseudomonas* and *Bacillus* Species Synergistically Degrades Polyethylene Terephthalate Plastic. *mSphere*. 2020 Dec 23;5(6).
167. Shirke AN, Basore D, Butterfoss GL, Bonneau R, Bystroff C, Gross RA. Toward rational thermostabilization of *Aspergillus oryzae* cutinase: Insights into catalytic and structural stability. *Proteins: Structure, Function, and Bioinformatics*. 2016 Jan;84(1):60–72.
168. Liu Z, Gosser Y, Baker PJ, Ravee Y, Lu Z, Alemu G, et al. Structural and Functional Studies of *Aspergillus oryzae* Cutinase: Enhanced Thermostability and Hydrolytic Activity of Synthetic Ester and Polyester Degradation. *Journal of the American Chemical Society*. 2009 Nov 4;131(43):15711–6.
169. Almeida EL, Carrillo Rincón AF, Jackson SA, Dobson ADW. *In silico* Screening and Heterologous Expression of a Polyethylene Terephthalate Hydrolase (PETase)-Like Enzyme (SM14est) With



- Polycaprolactone (PCL)-Degrading Activity, From the Marine Sponge-Derived Strain *Streptomyces* sp. SM14. *Frontiers in Microbiology*. 2019 Oct 1;10.
170. Huang Y-C, Chen G-H, Chen Y-F, Chen W-L, Yang C-H. Heterologous expression of thermostable acetyl xylan esterase gene from *Thermobifida fusca* and its synergistic action with xylanase for the production of xylooligosaccharides. *Biochemical and Biophysical Research Communications*. 2010 Oct;400(4):718–23.
  171. Zhang Z, Wang Y, Ruan J. Reclassification of *Thermomonospora* and *Microtetraspora*. *International Journal of Systematic Bacteriology*. 1998 Apr 1;48(2):411–22.
  172. Thumarat U, Nakamura R, Kawabata T, Suzuki H, Kawai F. Biochemical and genetic analysis of a cutinase-type polyesterase from a thermophilic *Thermobifida alba* AHK119. *Applied Microbiology and Biotechnology*. 2012 Jul 20;95(2):419–30.
  173. Fersht AR. Profile of Martin Karplus, Michael Levitt, and Arieh Warshel, 2013 Nobel Laureates in Chemistry. *Proceedings of the National Academy of Sciences*. 2013 Dec 3;110(49):19656–7.
  174. Adcock SA, McCammon JA. Molecular Dynamics: Survey of Methods for Simulating the Activity of Proteins. *Chemical Reviews*. 2006 May 1;106(5):1589–615.
  175. Guvench O, MacKerell AD. Comparison of Protein Force Fields for Molecular Dynamics Simulations. *Chemical Reviews*. 2008 443:63–88.
  176. Vanommeslaeghe K, Guvench O, MacKerell AD. Molecular mechanics. *Current pharmaceutical design*. 2014;20(20):3281–92.
  177. Brooks BR, Brooks CL, Mackerell AD, Nilsson L, Petrella RJ, Roux B, et al. CHARMM: The biomolecular simulation program. *Journal of Computational Chemistry*. 2009 Jul 30;30(10):1545–614.
  178. Jorgensen WL, Tirado-Rives J. The OPLS [optimized potentials for liquid simulations] potential functions for proteins, energy minimizations for crystals of cyclic peptides and crambin. *Journal of the American Chemical Society*. 1988 Mar 1;110(6):1657–66.
  179. Scott WRP, Hünenberger PH, Tironi IG, Mark AE, Billeter SR, Fennel J, et al. The GROMOS Biomolecular Simulation Program Package. *The Journal of Physical Chemistry A*. 1999 May 1;103(19):3596–607.
  180. González MA. Force fields and molecular dynamics simulations. *École thématique de la Société Française de la Neutronique*. 2011 Jun 9;12:169–200.
  181. Alder BJ, Wainwright TE. *Studies in Molecular Dynamics*. I. General Method. *The Journal of Chemical Physics*. 1959 Aug;31(2):459–66.
  182. McCammon JA, Gelin BR, Karplus M. Dynamics of folded proteins. *Nature*. 1977 Jun;267(5612):585–90.
  183. Dawe GB, Musgaard M, Arousseau MRP, Nayeem N, Green T, Biggin PC, et al. Distinct Structural Pathways Coordinate the Activation of AMPA Receptor-Auxiliary Subunit Complexes. *Neuron*. 2016 Mar;89(6):1264–76.
  184. McCorvy JD, Butler K v, Kelly B, Rechsteiner K, Karpiak J, Betz RM, et al. Structure-inspired design of  $\beta$ -arrestin-biased ligands for aminergic GPCRs. *Nature Chemical Biology*. 2018 Feb 11;14(2):126–34.

185. Khandogin J, Brooks CL. Linking folding with aggregation in Alzheimer's beta-amyloid peptides. *Proceedings of the National Academy of Sciences*. 2007 Oct 23;104(43):16880–5.
186. Leach A, *Molecular Modelling: Principles and Applications* (2nd Edition). 2001: Prentice Hall.
187. Kräutler V, van Gunsteren WF, Hünenberger PH. A fast SHAKE algorithm to solve distance constraint equations for small molecules in molecular dynamics simulations. *Journal of Computational Chemistry*. 2001 Apr 15;22(5):501–8.
188. Ryckaert J-P, Ciccotti G, Berendsen HJC. Numerical integration of the cartesian equations of motion of a system with constraints: molecular dynamics of n-alkanes. *Journal of Computational Physics*. 1977 Mar;23(3):327–41.
189. Stephens PJ, Devlin FJ, Chabalowski CF, Frisch MJ. Ab Initio Calculation of Vibrational Absorption and Circular Dichroism Spectra Using Density Functional Force Fields. *The Journal of Physical Chemistry*. 1994 Nov 1;98(45):11623–7.
190. Hariharan PC, Pople JA. The influence of polarization functions on molecular orbital hydrogenation energies. *Theoretica Chimica Acta*. 1973;28(3):213–22.
191. Cramer, C.J., *Essentials of Computational Chemistry - Theories and Models*. 2nd ed. 2004: John Wiley & Sons. 596.
192. Kohn W, Sham LJ. Self-Consistent Equations Including Exchange and Correlation Effects. *Physical Review*. 1964. 136(3B):B864-B871.
193. Clark T, Chandrasekhar J, Spitznagel GW, Schleyer PVR. Efficient diffuse function-augmented basis sets for anion calculations. III. The 3-21+ G basis set for first-row elements, Li–F. *Journal of Computational Chemistry*. 1983;4(3):294–301.
194. Chung LW, Sameera WMC, Ramozzi R, Page AJ, Hatanaka M, Petrova GP, et al. The ONIOM Method and Its Applications. *Chemical Reviews*. 2015 Jun 24;115(12):5678–796.
195. Dapprich S, Komáromi I, Byun KS, Morokuma K, Frisch MJ. A new ONIOM implementation in Gaussian98. Part I. The calculation of energies, gradients, vibrational frequencies and electric field derivatives. *Journal of Molecular Structure: THEOCHEM*. 1999;461:1–21.
196. W. J. Hehre, W. A. Lathan, R. Ditchfield, M. D. Newton, and J. A. Pople, Gaussian 70 (Quantum Chemistry Program Exchange, Program No. 237, 1970).
197. Frisch MJ, Trucks GW, Schlegel HB, Scuseria GE, Robb MA, Cheeseman JR et al. (2009) Gaussian 09. Gaussian, Inc., Wallingford, CT, USA.
198. Neese F, Wennmohs F, Becker U, Riplinger C. The ORCA quantum chemistry program package. *The Journal of Chemical Physics*. 2020 Jun 14;152(22):224108.
199. Guo Y, Riplinger C, Becker U, Liakos DG, Minenkov Y, Cavallo L, et al. Communication: An improved linear scaling perturbative triples correction for the domain based local pair-natural orbital based singles and doubles coupled cluster method [DLPNO-CCSD(T)]. *The Journal of Chemical Physics*. 2018 Jan 7;148(1):011101.
200. Dunning TH. Gaussian basis sets for use in correlated molecular calculations. I. The atoms boron through neon and hydrogen. *The Journal of Chemical Physics*. 1989 Jan 15;90(2):1007–23.

201. Chang A, Jeske L, Ulbrich S, Hofmann J, Koblitz J, Schomburg I, et al. BRENDA, the ELIXIR core data resource in 2021: new developments and updates. *Nucleic Acids Research*. 2021 Jan 8;49(D1):D498–508.
202. BRENDA is available at [www.brenda-enzymes.org](http://www.brenda-enzymes.org) (accessed on 23 December 2021).
203. Caspi R, Altman T, Billington R, Dreher K, Foerster H, Fulcher CA, et al. The MetaCyc database of metabolic pathways and enzymes and the BioCyc collection of Pathway/Genome Databases. *Nucleic Acids Research*. 2014 Jan;42(D1):D459–71.
204. Lenfant N, Hotelier T, Velluet E, Bourne Y, Marchot P, Chatonnet A. ESTHER, the database of the  $\alpha/\beta$ -hydrolase fold superfamily of proteins: tools to explore diversity of functions. *Nucleic Acids Research*. 2012 Nov 26;41(D1):D423–9.
205. Warren BE. X-Ray Diffraction. Courier Corporation. 1990
206. Hore PJ. Nuclear magnetic resonance. Oxford University Press, USA; 2015.
207. Bacon GE. Neutron diffraction 3 edition. Clarendon Press; 1975
208. Dubochet J, Adrian M, Chang J-J, Homo J-C, Lepault J, McDowell AW, et al. Cryo-electron microscopy of vitrified specimens. *Quarterly Reviews of Biophysics*. 1988 May 17;21(2):129–228.
209. S. Fernandes H, Ramos MJ, M. F. S. A. Cerqueira N. molUP: A VMD plugin to handle QM and ONIOM calculations using the gaussian software. *Journal of Computational Chemistry*. 2018 Jul 15;39(19):1344–53.
210. Humphrey W, Dalke A, Schulten K. VMD: Visual molecular dynamics. *Journal of Molecular Graphics*. 1996 Feb;14(1):33–8.
211. Fernandes HS, Sousa SF, Cerqueira NMFS. VMD Store—A VMD Plugin to Browse, Discover, and Install VMD Extensions. *Journal of Chemical Information and Modeling*. 2019 Nov 25;59(11):4519–23.
212. Maier JA, Martinez C, Kasavajhala K, Wickstrom L, Hauser KE, Simmerling C. ff14SB: Improving the Accuracy of Protein Side Chain and Backbone Parameters from ff99SB. *Journal of Chemical Theory and Computation*. 2015 Aug 11;11(8):3696–713.
213. Neese F. The ORCA program system. *WIREs Computational Molecular Science*. 2012 Jan 28;2(1):73–8.
214. Schrödinger Release 2021-4: Protein Preparation Wizard; Epik, Schrödinger, LLC, New York, NY, 2021; Impact, Schrödinger, LLC, New York, NY; Prime, Schrödinger, LLC, New York, NY, 2021.
215. Schrödinger Release 2021-4: Epik, Schrödinger, LLC, New York, NY, 2021.
216. Anandkrishnan R, Aguilar B, Onufriev A v. *H++* 3.0: automating pK prediction and the preparation of biomolecular structures for atomistic molecular modeling and simulations. *Nucleic Acids Research*. 2012 Jul 1;40(W1):W537–41.
217. Olsson MHM, Søndergaard CR, Rostkowski M, Jensen JH. PROPKA3: Consistent Treatment of Internal and Surface Residues in Empirical pK<sub>a</sub> Predictions. *Journal of Chemical Theory and Computation*. 2011 Feb 8;7(2):525–37.

218. Huang J, Rauscher S, Nawrocki G, Ran T, Feig M, de Groot BL, et al. CHARMM36m: an improved force field for folded and intrinsically disordered proteins. *Nature Methods*. 2017 Jan 7;14(1):71–3.
219. Torrie GM, Valleau JP. Nonphysical sampling distributions in Monte Carlo free-energy estimation: Umbrella sampling. *Journal of Computational Physics*. 1977 Feb;23(2):187–99.
220. Elstner M. The SCC-DFTB method and its application to biological systems. *Theoretical Chemistry Accounts*. 2006 Jul 31;116(1–3):316–25.

# F. Appendices

## 1. List of articles

### **Review:**

Perspectives on the Role of Enzymatic Biocatalysis for the Degradation of Plastic PET

Magalhães, Rita P., Jorge M. Cunha, and Sérgio F. Sousa

International Journal of Molecular Sciences 22 (20) (2021)

DOI: 10.3390/ijms222011257

## 2. Conference communication

### **Poster presentation:**

Jorge M. Cunha, Rita P. Magalhães, Henrique S. Fernandes, Sérgio F. Sousa “Application of QM/MM methods for development of plastic degradation enzymes” - Encontro de jovens investigadores da Universidade do Porto (IJUP), Portugal/Porto, 2020 May 6th

Jorge M. Cunha, Rita P. Magalhães, Henrique S. Fernandes, Sérgio F. Sousa “Bioinformatic applications for the development of plastic degradation enzymes using QM/MM” - X Bioinformatics Open Days, Braga/Portugal, 2020 May 6th

## Application of QM/MM methods for Development of Plastic Degradation Enzymes

Jorge M. Cunha, Rita P. Magalhães, Henrique S. Fernandes, Sérgio F. Sousa

UCIBIO/REQUIMTE, BioSIM - Departamento de Biomedicina, Faculdade de Medicina, Universidade do Porto, Alameda Professor Hamílton Monteiro, 4200-319 Porto, Portugal

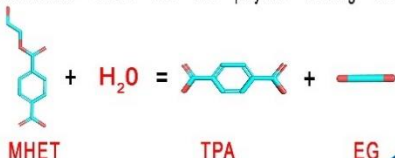
jorgemcunha97@gmail.com

### Introduction

Plastic production has been dramatically increasing, reaching values as high as 350 million tons annually. The excess can be accumulated in soils and oceans causing major consequences to all forms of life.

Chemical strategies used in plastic degradation industry can degrade plastic, however the aftermath is not environmentally friendly, causing problems such as air pollution. Thus, strategies like using biocatalysts are being developed.

MHETase from *Ideonella sakaiensis* is capable of degrading the PET intermediate MHET into the polymer building blocks TPA and EG.



MHET

TPA

EG

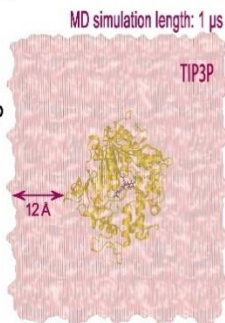
### Molecular Dynamics

PDB structures were downloaded from Protein Data Bank and treated in molUP VMD software

Molecular Dynamics Amber18 software

Protein ff14SB

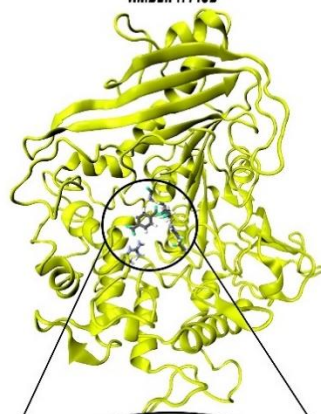
MHET ANTECHAMBER:GAFF,  
RESP:HF/6-31G(d)



Timestep 2 fs T = 300 K  
Cutoff = 10 Å P = 1 bar  
SHAKE (bonds with H)

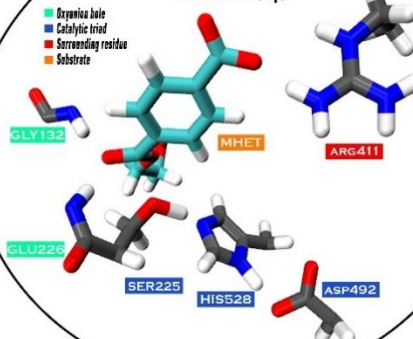
### QM/MM

Gaussian09 / ONIOM - molUP  
Molecular Mechanics (MM)  
AMBER ff14SB



### Quantum Mechanics (QM)

B3LYP/6-31G(d,p)



### Future perspectives

The next studies will be the application of the ONIOM QM/MM computational methodology for detailed description of the catalytic mechanism and the application of in-site mutagenesis in key residues for activity enhancement.

### References

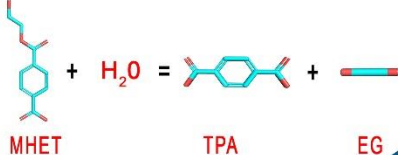
- [1] Sinha et al, J. Polym. Environ. 2010; 18: 8-25
- [2] Yoshida et al, Science 2016; 351:1196-1199
- [3] Magalhães et al, Isr. J. Chem. 2020; 60, 655-666

### Introduction

Plastic production has been dramatically increasing, reaching values as high as 350 million tons annually. The excess can be accumulated in soils and oceans causing major consequences to all forms of life.

Chemical strategies used in plastic degradation industry can degrade plastic, however the aftermath is not environmentally friendly, causing problems such as air pollution. Thus, strategies like using biocatalysts are being developed.

MHETase from *Ideonella sakaiensis* is capable of degrading the PET intermediate MHET into the polymer building blocks TPA and EG.



MHET

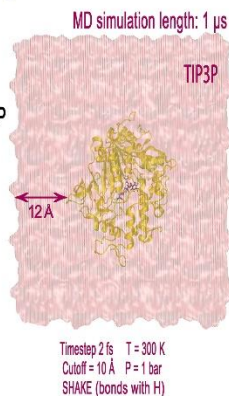
TPA

EG

### Molecular Dynamics

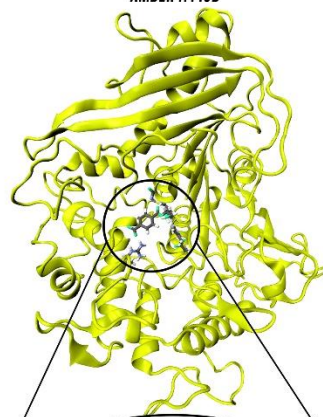
PDB structures were downloaded from Protein Data Bank and treated in molUP VMD software

Molecular Dynamics Amber18 software  
 Protein ff14SB  
 MHET ANTECHAMBER:GAFF,  
 RESP:HF/6-31G(d)



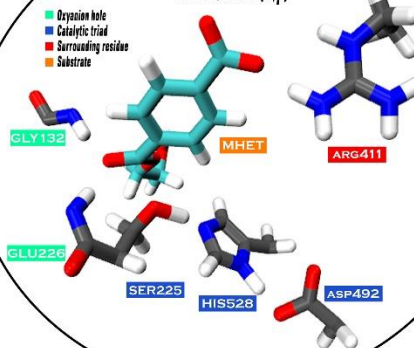
### QM/MM

Gaussian09 / ONIOM - molUP  
 Molecular Mechanics (MM)  
 AMBER ff14SB



### Quantum Mechanics (QM)

B3LYP/6-31G(d,p)



### Future perspectives

The next studies will be the application of the ONIOM QM/MM computational methodology for detailed description of the catalytic mechanism and the application of in-site mutagenesis in key residues for activity enhancement.

### References

- [1] Sinha et al, J. Polym. Environ. 2010; 18: 8-25
- [2] Yoshida et al, Science 2018; 351:1196-1199
- [3] Magalhaes et al, Isr. J. Chem. 2020; 60, 655-666